Structural Systems Inspired by the Architecture of Skeletal Muscle

by

Narayanan Kidambi

A dissertation submitted in partial fulfillment
of the requirements for the degree of
Doctor of Philosophy
(Mechanical Engineering)
in the University of Michigan
2018

Doctoral Committee:

Professor Kon-Well Wang, Chair
Assistant Professor Evgueni Filipov
Professor Gregory Hulbert
Professor Noel Perkins

Narayanan Kidambi

kidambi@umich.edu

ORCID iD: 0000-0002-5832-4564

To Amma, Appa and Katie

Acknowledgements

I would like to first acknowledge my advisor, Dr. Kon-Well Wang. Throughout my time at the University of Michigan, he has been a constant source of support, encouragement, and inspiration. I am incredibly fortunate and appreciative of the opportunity to work under his guidance in the Structural Dynamics and Controls Lab. I would also like to thank the members of my dissertation committee, Dr. Evgueni Filipov, Dr. Greg Hulbert, and Dr. Noel Perkins, for their insightful and helpful feedback on this dissertation work.

With colleagues in our research group, both past and present, I have had many fruitful and fun discussions on both research and the world beyond. I am especially grateful to Dr. Ryan Harne, now an Assistant Professor at the Ohio State University, who has been a wonderful mentor since the day I started my research in the lab. He continues to offer valuable input, and I am truly inspired by his dedication. The people I have met over the last several years have helped make my time at Michigan truly enjoyable. I have forged cherished friendships over coffee breaks, trivia nights, and rooftop hangouts, and have worked with some great folks in the ME Graduate Council. I would also like to acknowledge funding support from the University of Michigan, Ford Motor Company, and the Army Research Office.

Finally, this thesis would not have been possible were it not for my family. Thank you, Katie, for giving me a reason to smile every single day, and for being simply the best partner with whom to tackle life's challenges. Thank you, Amma and Appa, for all your love, support, and sacrifice from literally day one. Your patience, generosity, and commitment are virtues I hope I can emulate in my own life.

Table of Contents

List of Figures

List of Tables

List of Appendices

Abstract

Modern engineering applications call for structural and material systems that exhibit advanced performance. To achieve this performance, researchers often look to nature for inspiration. Skeletal muscle is a multifunctional system with remarkable versatility and robustness, offering a great example on how to effectively store, convert, and release energy for force generation and shape change. To date, most efforts seeking to emulate muscle have focused on its bulk characteristics. However, it has recently been shown that many of muscle's advantageous properties arise from the assembly and geometry of its microscale constituents. This dissertation will aim to develop new concepts for structural and material systems inspired by a fundamental understanding of the assembly of muscle's constituent elements into contractile units. This is achieved by exploiting two key ingredients expressed by these constituents: *metastability*, which is the existence of multiple stable conformations for a prescribed global geometry, and *local conformation changes* to switch between these stable topologies. Rather than faithfully emulating or seeking to explain the complex chemo-mechanical processes that govern muscle contraction, the major contributions of this thesis arise from the exploitation of the aforementioned key features within the context of engineered structures and materials systems.

First, a fundamental metastable unit is studied under harmonic excitation. Experimental, numerical, and analytical investigations uncover the coexistence of multiple response regimes with significantly different amplitudes. These distinct regimes are exploited to achieve highly adaptable energy dissipation characteristics that vary by up to two orders of magnitude among them, even as

excitation parameters are held constant. On the other hand, introducing asymmetry by varying a static bias parameter allows for smooth, finer variation of energy dissipation performance. Then, inspired by the ability of the myofibril lattice in skeletal muscle to trap strain energy that can be released on-demand, this thesis explores structural systems that leverage asymmetric multistability for energy capture and storage. The initial kinetic energy from impulsive excitation is shown to trigger state transitions that result in the capture of recoverable strain energy in higher-potential states. Reverse transitions to lower-energy states exploit this stored energy to facilitate efficient deployment and length change in the structure. Lastly, the effect of myofibril lattice spacing in skeletal muscle, and shear-like motions of adjacent filaments during contraction, serves as inspiration for the development of an architected modular material system that uses transverse confinements in conjunction with oblique, shear-like motions to give rise to sudden state transitions. Numerical results provide insight into the experimentally-observed behaviors, revealing that these energy-releasing transitions correspond to discrete changes in reaction force magnitude and direction Mechanical response properties can be tailored by strategic variation of transverse confinement and system geometry. Analytical tools using relatively simple models are developed to offer meaningful prediction of the above features. The overall outcomes of this thesis reveal great potential to develop high-performance, versatile, and adaptable structural and material systems by exploiting fundamental features of skeletal muscle architecture.

Chapter 1. Introduction and background

1.1 Introduction

An increasing number of engineering applications call for structural and material systems that exhibit performance and adaptability beyond the capabilities of bulk constituents. Furthermore, there are inherent advantages to realizing this adaptability without the need for complex, active controls [1–3]. Skeletal muscle is a multifunctional system that effectively balances these two objectives, providing strong inspiration for the development of advanced engineered structures and materials. It exhibits robustness and adaptation of macroscale properties in order to ensure energetic efficiency of motions, while minimizing the risk of damage or over-straining [4–7]. It is also energetically versatile, and can effectively store, convert and release energy to facilitate rapid force generation or length change [8,9]. These macroscale properties are strongly dependent on the coordination between skeletal muscle's constituents across its length scales [10]. To date, most researchers have taken inspiration from muscle's macroscale structure and functionality for a variety of applications in the fields of robotics and prosthetics, as well as to improve our understanding of movement and locomotion. There are comparatively fewer efforts that take as inspiration skeletal muscle's microscale architecture, despite evidence that this may be the origin for many of its attractive macroscale characteristics [11–13].

Historically, development of a comprehensive understanding of skeletal muscle's microscale behaviors has been hindered by challenging experimental conditions which render it very difficult to

accurately observe mechanical properties at the smaller length scales. Nevertheless, experimental efforts over the past few decades have revealed remarkable properties that arise from skeletal muscle's microscale architecture. These properties include rapid tension recovery from perturbations [14,15], force enhancement when skeletal muscle's microscale sarcomere constituents are extended beyond their ideal lengths [16,17], and strain energy storage in micro- and nanoscale constituents that can be released to enable explosive motion or reduce the metabolic cost of cyclic movements [6,18,19].

This chapter of the dissertation offers background information on skeletal muscle architecture and functionality, including mechanical models that have been developed to reflect the behaviors of various constituents. It also presents an overview of past efforts to develop engineered systems inspired by muscle, and motivates the development of engineered structures and materials that invoke key features of skeletal muscle's micro- and nanoscale architecture.

1.2 Summary of skeletal muscle architecture

Like many biological systems, skeletal muscle exhibits a strong relationship between structure and functionality. Both its macroscopic and microscopic components and assemblies have evolved to enable very effective force generation and movement [4]. Figure 1-1 presents skeletal muscle's morphology from the whole muscle scale down to its micro- and nanoscale sarcomere and cross-bridge constituents. Skeletal muscles primarily span joints in the skeletal system, and are attached to bones through connective tendon tissue. This connective tissue extends to form the epimysium, a layer that wraps around the muscle body. The muscle body itself is composed of bundles of fascicles, each surrounded by a perimysium layer. Fascicles are in turn composed of bundles of muscle fibers or muscle cells enclosed by sarcolemma membranes and surrounded by endomysium tissue. The endomysium is highly vascularized, carrying small blood vessels to the muscle fibers. Muscle fibers

can vary significantly in size, and are ordinarily between 10 μm and 100 μm in diameter and 10 cm in length [5]. The main components of muscle fibers are rod-like structures known as myofibrils, which are on the order of 1 μm in diameter [4] and are sectioned into contractile units called sarcomeres. Myofibrils are made up of alternating thin and thick protein filaments arranged in a lattice. The thin

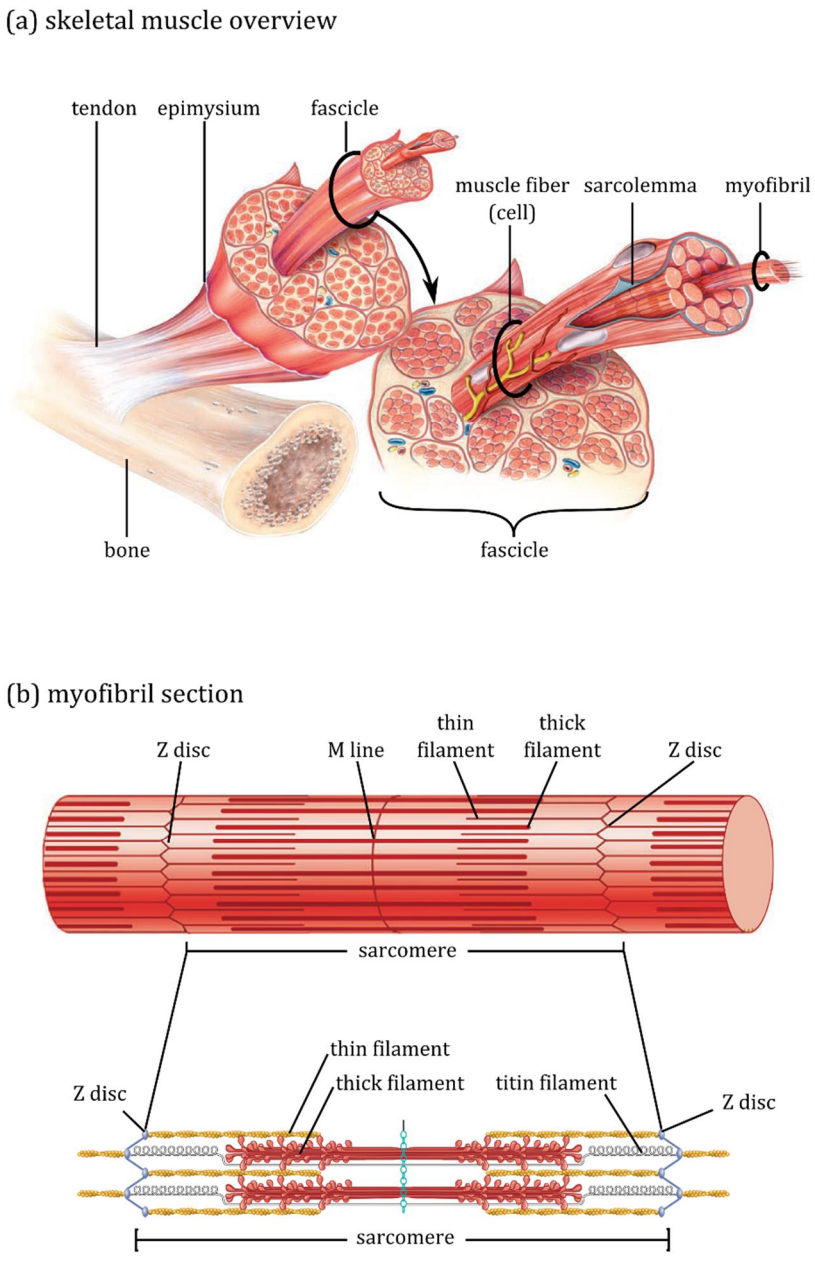

Figure 1-1. Components and architecture of skeletal muscle from (a) whole muscle to the myofibril level, showing (b) the arrangement of actin and myosin filaments in sarcomere contractile units. Images are reused from [5] with written permission from the publisher.

filament is primarily composed of the protein actin and is about 7 nm in diameter, while the thick filament is primarily composed of the myosin and is roughly 15 nm in diameter [20]. A single thick filament may contain up to hundreds of cross-bridges [5,12], while thousands of sarcomeres comprise a myofibril [4].

Skeletal muscle fiber contractions are the result of a complex process. Details can be found in references [4,5], but a brief overview of the role of key constituents is presented here and in the following sections. Nerve impulses trigger local action potentials, initiating the release of Ca^{2+} ions from the sarcoplasm surrounding the myofibrils. This leads to the opening of actin binding sites on the thin filament. Myosin protein heads that extend from the thick filament attach to these binding sites when energized by ATP (adenosine triphosphate) hydrolysis, forming cross-bridges. The resulting ADP (adenosine diphosphate) is then released from the cross-bridge, which undergoes a conformational change known as the power stroke. The power stroke is characterized by a rotation of the myosin head, generating a force that causes the thick filament to slide against the thin filament, and represents skeletal muscle's fundamental active force generating process.

1.3 Mechanical models of microscale constituents

Researchers have developed a number of relatively simple models to explain and gain insight into muscle mechanics at various length scales. Macroscale models incorporate stiffness and damping elements in various configurations to capture the bulk passive responses of muscle and tendons [10,21]. Muscle models that explicitly consider fiber orientations have been used to explain the force and velocity amplification observed in pennate muscles, where fibers are aligned oblique to the axis of overall muscle contraction [7,22,23]. At the microscale, the mechanisms that govern active force generation in sarcomere contractile units are the result of simultaneous chemical, mechanical, and

thermal processes. Nevertheless, mechanical representations have been employed to explain and gain insight into many features of skeletal muscle, both active and passive [13,24].

1.3.1 Myofibrils and sarcomeres

A simple and common myofibril model is presented in Figure 1-2(a), and consists of a chain of serially-connected half-sarcomeres [25–27]. A myofibril can contain as many as 10^4 sarcomeres [28], and the response of an individual sarcomere can be characterized by a superposition of an active contractile component and a passive component. A simplified sarcomere schematic is shown in Figure 1-2(b). The active contractile elements represent the actin-myosin interactions of ATP-fueled power strokes, while the passive components represent filament elasticity, particularly that of the structural protein titin [4,29,30]. A characteristic sarcomere length-tension response is presented in Figure 1-2(c) based on a model first developed by A.V. Hill [31] that combines the active and passive components, The active response possesses a region with negative stiffness or negative slope known as the descending limb. The observed stability of myofibrils at any length despite the presence of these large negative stiffness regions in the sarcomeres has led to modelling and experimental efforts seeking to understand the origin of this behavior [26,27,32].

Due to the inhomogeneity of sarcomeres in a myofibril, it has been postulated that a lengthening muscle fiber can remain stable in its aggregate descending limb while each individual sarcomere jumps across its own local descending limb region in an event known as sarcomere popping [33,34]. In shortening muscle, stronger sarcomeres may snap across the descending limb to the ascending limb of the active response, at the expense of weaker sarcomeres that must rely on passive tension to achieve the same response [32]. With a large number of sarcomeres in a single myofibril, there are exponentially many combinations of individual sarcomere states possible for a given fiber length. This feature is known as *metastability*, and may explain the experimentally-observed hysteresis and history-dependence of both shortening and lengthening active muscle [25,27,35]. Sarcomere tension

response depends not only on its length, but also on the inter-filament spacing [36]. Two- and three-dimensional models that account for variations in lattice spacing are shown to predict sarcomere tension responses across a range of lengths [37,38].

The sarcomere length-tension curve also varies with its velocity of shortening [4,10,39], and a sarcomere model that explicitly accounts for velocity-dependent forces is presented in Figure 1-3 [26].

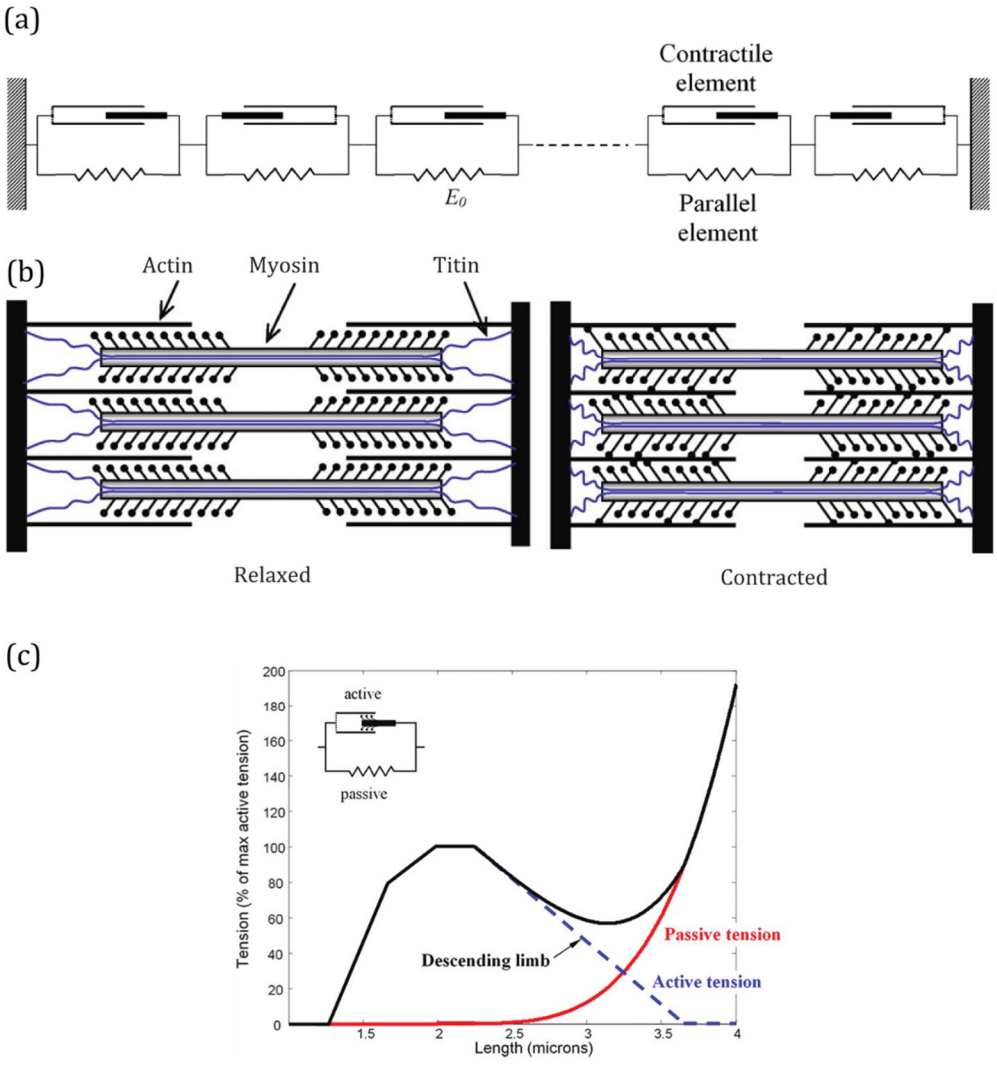

Figure 1-2. (a) A myofibril represented by a chain of serially connected half-sarcomeres, each with an active contractile element representing the actin-myosin interactions, and a passive elasticity. (b) Schematic of an individual sarcomere in relaxed and contracted configurations, showing the structural protein titin, which is largely responsible for the parallel elasticity in (a). (c) The length-tension response of an individual half-sarcomere arises due to the combination of both active and passive influences. The active component exhibits a negative stiffness or slope known as the descending limb. This is compensated for by large passive tension as sarcomere length increases further. (a) and (c) are reused from [26] and (b) is reused from [25], with written permission from the publishers.

This model is still relatively simple, but explicitly separates the active force generation due to cross-bridge power strokes from the series passive elasticity of the actin and myosin filaments. The active element and the parallel titin component both have velocity-dependent terms. Consideration of these influences helps explain the sensitivity of muscle fibers' dynamic response to the initial distribution of sarcomere states, which had previously been attributed to the uncontrollable variability inherent to such a complex biological system [25,26].

While some myofibril models do not assume the existence of any mechanism to ensure stability of sarcomeres in the negative stiffness descending limb [25,27], other models suggest that the titin protein may have an key role to play [16,40,41]. Titin, which earns its name due to its relatively giant size (around 1 μm), is a structural protein that connects myosin to either end of the sarcomere unit, and helps align the myofibril lattice as actin and myosin filaments slide against one another [5]. Titin may itself be modeled as a chain of ~240 bistable units that unfold as sarcomeres are lengthened [42]. It has been shown that this interpretation of titin structure provides an explanation for its role as a shock absorber, where the sequential and rapid unfolding of the bistable domains provides a mechanism to quickly release energy and avoid over-straining of muscle fibers during eccentric (lengthening) sarcomere contractions [16,43–45].

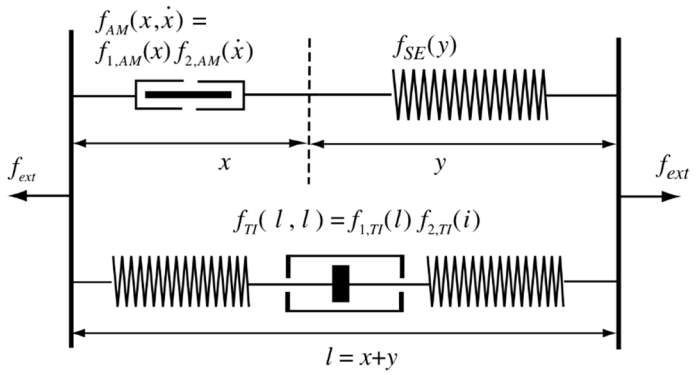

Figure 1-3. Sarcomere model divided into two parallel strands. The upper strand shows an active contractile element with force response f_{AM} and a series elastic element with force f_{SE}, while the lower strand is the parallel passive element with force f_{TI} representing the contribution of the titin protein. Image reused from [26] with written permission.

1.3.2 Cross-bridges and the power stroke

The modern understanding of the process governing muscle contraction, the *sliding filament theory* [4,46], largely stems from the observations of Huxley and Niedergerke [47] and Huxley and Hanson [48] in the 1950s. The existence of cross-bridges extending from the myosin (thick) filament was shown soon thereafter [49]. However, the mechanisms that cause this sliding motion were not clarified until later, when Huxley proposed that these cross-bridges have globular heads that attach to actin at certain binding sites, and that this angle of attachment undergoes an active change due to ATP hydrolysis [50]. A basic biochemical model explaining cross-bridge attachment to actin, the force-generating power stroke, and subsequent detachment is known as the Lymn-Taylor cross-bridge cycle [51], and it has been further refined in recent years as experimental efforts have shed new light into the structures and processes involved [4].

While chemical kinetics must be considered for any complete model of the cross-bridge cycle, the behavior of a bound cross-bridge lends itself to a simpler representation of a bistable contractile element connected to a linear stiffness. The power stroke occurs at extremely fast time scales, and as such can be considered as an event with a purely mechanical, rather than chemical, response. The mechanical representation of the cross-bridge is also shown to reasonably predict observed

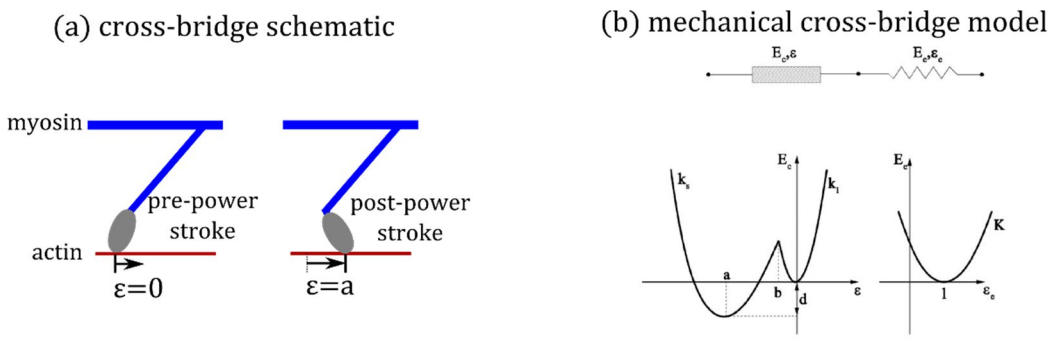

Figure 1-4. (a) Schematic of a single cross-bridge in pre- and post-power stroke configurations. The power stroke generates causes the actin and myosin filaments to slide against one another, resulting in sarcomere contraction. (b) An example of a one-dimensional cross-bridge model, composed of one bistable element and one linear-elastic element in series. The two local minima of the bistable element's potential, E_C, denote the pre- and post-power stroke states. The linear-elastic element represents filament elasticity. (b) is reused from [12] with written permission from the publisher.

behaviors such as power stroke reversal and rapid tension recovery [40,52–54]. A schematic is presented in Figure 1-4. The two states of the bistable element represent the pre- and post-power configurations. The two local minima of potential energy in the bistable constituent are at different levels, reflecting a natural bias in the element's energy landscape where the *long*, or *pre-power stroke* state is at a higher energy than the *short* or *post-power stroke* state. Early efforts such the Huxley-Simmons work [53], treated the two configurations as discrete chemical states with infinitely narrow potential wells. However, a mechanical snap-spring representation of the power stroke that includes the influence of cross-bridge elasticity and permits continuous, finite-time configuration changes was seen to better reflect more recent experimental findings [35,52,54]. As long as filament and cross-bridge stiffness is not too large, a cross-bridge can exhibit metastability – It can be in either the pre- or post-power stroke for a given sarcomere length. Since a single sarcomere may contain hundreds or thousands of cross-bridges, an exponential number of aggregate metastable states are possible, and transitions between these metastable configurations may help explain muscle's remarkable ability to dissipate energy and rapidly yet passively recover tension in response to sudden loads [54,55].

Just as a sarcomere's tension response is influenced by the lattice spacing [36,37], so too are the forces generated during the cross-bridge power stroke. It has been shown that varying the lattice spacing affects the chances of cross-bridge binding [56], and spatially-explicit models that consider radial cross-bridge deformations in addition to axial deformations may shed light on the mechanisms that regulate the sarcomere tension response at various lengths [37,57]. An example is presented in Figure 1-5, which shows a comparison between models composed of (a) a single spring, (b) two springs, and (c) four springs. The two- and four-spring models explicitly account for lattice spacing, while the four-spring model further reflects the conformation changes exhibited in the myosin head during the power stroke. Consideration of radial cross-bridge deformations may help explain the ability of the myofibril lattice to store elastic potential energy that can be subsequently actively exploited and released to enable rapid movements [9,19,38].

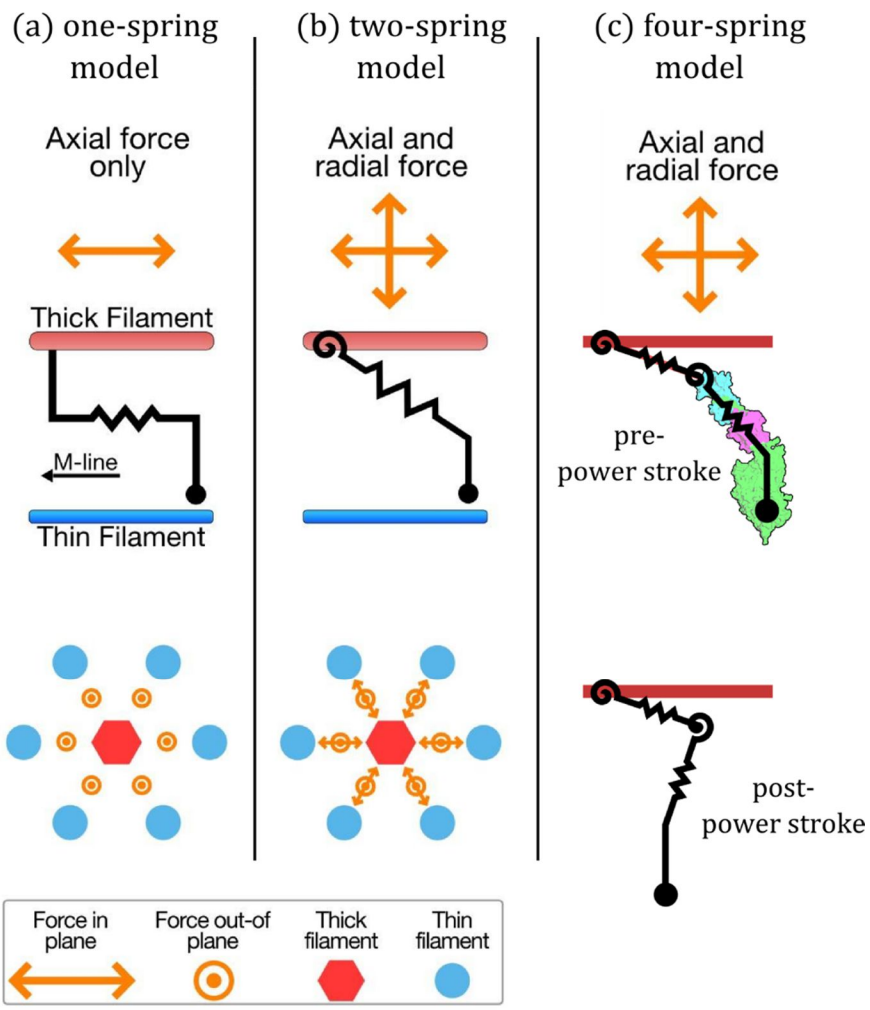

Figure 1-5. Cross-bridge models composed of (a) one spring, (b) two springs, one of which is torsional, and (c) four springs, two of which are torsional. The two- and four-spring representations are capable of modeling both axial and radial forces. Images (a,b) and (c) are reproduced and modified from [37] and [38], respectively, under the terms of the Creative Commons Attribution License.

1.4 Engineered systems and structures inspired by muscle

Researchers have long looked to biology as inspiration for a wide range of engineered materials, structures, and systems [58–62]. The development of systems based on the characteristics of skeletal muscle have generally targeted an emulation of its smooth and continuous force generation and shape change. These behaviors are especially beneficial for soft robotics, where the ability to change morphology according to the task and environment are crucial [63,64], and are commonly achieved

through a variety of means [65,66], including pneumatics and fluidics [67,68], electro-active polymers [69–71], and shape-memory materials [72].

On the other hand, the means by which the architecture of muscle's microscale constituents can be leveraged for advanced engineered structures and materials have received much less focus [73,74], despite strong evidence from experiments and analyses that have demonstrated the crucial role of skeletal muscle's microscale constituents on its macroscopic behavior [4,24,46,50]. Recent efforts have uncovered the role of local configuration changes in the micro- and nanoscale sarcomeres and cross-bridges on its remarkable robustness and passive tension recovery [24,52,54], as well as its ability to store elastic energy in these components to facilitate rapid, efficient movements [6,8,19]. These findings provide strong motivation for the development of engineered structures and materials that exploit a similar arrangement of constituents.

The arrangement of elastic constituents in models of the skeletal muscle cross-bridge [52,54] has recently been explored in mechanical analogues [75,76], as presented in Figure 1-6. These mechanical systems emulate the metastability expressed by a single cross-bridge and its enhancement when considering multiple cross-bridges. This is exploited to enable dramatic adaptivity in reaction force and stiffness by considering different internal arrangements for a prescribed global length, and large hysteresis under quasi-static cyclic loading to generate large hysteresis. When large numbers of such modules are arranged in parallel, the adaptivity in mechanical properties increases dramatically [76].

Insights on the shock and energy absorption and dissipation behaviors of titin [43] have motivated analytical and numerical analyses of bistable chains with unique, trilinear local strain responses [45] and simple quasi-static experiments on mechanical systems that display similar characteristics to titin [42]. Figure 1-7(a) presents results from experiments conducted on a single titin protein, and

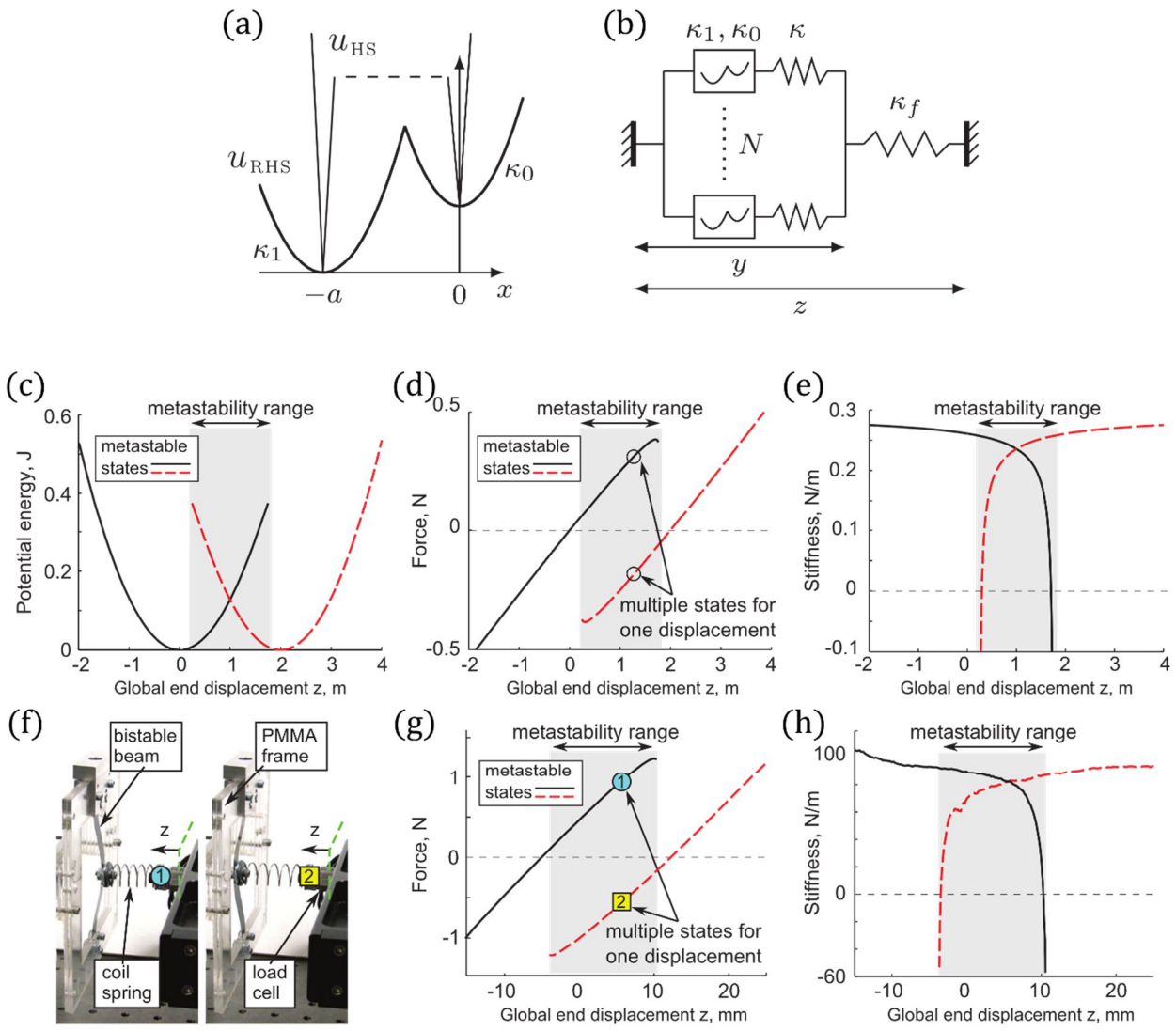

Figure 1-6. (a) Energy in the power-stroke element, and (b) its series arrangement with a linear elastic element to form a cross-bridge. A half-sarcomere model includes *N* cross-bridges in parallel. (c) Potential strain energy for a single *metastable module* – one bistable and linear elastic element arranged in series – as a function of overall length. (f) An experimental metastable module showing two configurations with the same global displacement. (g) Reaction force and (h) stiffness responses for the experimental prototype. (a,b) and (c-h) are reproduced from [54] and [75], respectively, with written permission from the publishers

Figure 1-7(b) presents a mechanical chain of bistable units that is used to verify the theoretical predictions on stiffness and state transitions in titin-like systems. The authors employ this model as a demonstration that the complex stress-strain response and shock-absorbing capabilities of titin as its numerous domains unfold can be approximated by a much simpler equivalent system.

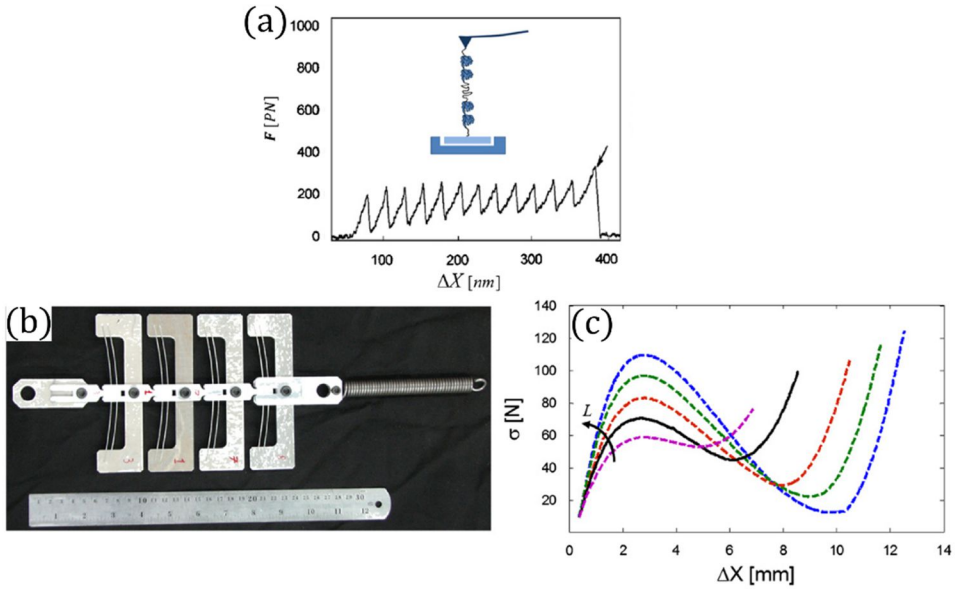

Figure 1-7. (a) Experimental results from the stretching of titin domains. (b) Assembly of mechanical bistable units into a chain with a linear spring at one end. (c) The effect of beam length on the bistable force response of a single unit. Images are reused from [42] with written permission from the publisher.

While the above works develop important insight into the advantages of mechanical structures and materials employing a few key characteristics of skeletal muscle's microscale architecture, the investigations are limited to specific, quasi-static studies. However, engineered structures often operate in environments where dynamics play a critical role, and a comprehensive understanding of the dynamic response of these structures can make them more useful in a wider range of engineering applications. Furthermore, skeletal muscle offers a great example on how dynamic inertial loads can be exploited and leveraged for more efficient movements, and how mechanical responses can be modulated as key geometric parameters are varied. Hence, this dissertation seeks to learn from the architecture and functionality of the constituent units of skeletal muscle in order to develop concepts for mechanical structures and materials that offer similar characteristics.

1.5 Research statement

Skeletal muscle offers researchers great inspiration for the development of advanced engineered systems. While the vast majority of muscle-inspired systems focus on macroscale features, the origins of many of its advantageous properties arise from the architecture and functionality of its micro- and nanoscale constituents. Recent research efforts have developed detailed models of skeletal muscle's constituents across a variety of length scales, and there are extensive opportunities to use these findings to advance the development of structural and material systems.

This dissertation aims to introduce and comprehensively develop new concepts for structures exhibiting great energetic versatility and adaptivity inspired by the assembly of muscle's cross-bridges, sarcomeres, and myofibrils. This is broadly achieved by exploiting two key ingredients expressed by these constituents – *metastability*, and *local conformation changes*. It is important to note that this thesis does not seek to explain muscle behavior using mechanical or structural analogues, or faithfully replicate the complex chemo-mechanical processes that govern muscle contraction. Rather, the major contributions of this thesis arise from the exploitation of the aforementioned key features expressed by skeletal muscle's constituents for the development and investigation of novel structural and material systems. The outcomes reveal great potential for such systems for energy absorption and dissipation, the capture and release of strain energy for actuation and deployment, and adaptivity of mechanical properties by exploiting conformational change in conjunction with oblique, shear-like motions.

1.6 Summary of contributions

The metastability expressed by a cross-bridge [35,54] and its mechanical analogues [75,76] has been shown to provide a means to adapt mechanical properties such as global stiffness and stress. However, mechanical systems based on cross-bridge architecture offer great potential for adaptivity in dynamic behaviors in addition to the previously explored static features. In fact, it has been shown that bound cross-bridges can experience oscillatory power stroke reversals that may explain muscle's passive tension recovery and allow for energy dissipation [54,77]. The first major contribution of this thesis thus extends the notion of static metastability to explore the highly adaptive dynamic response and energy dissipation characteristics that arise as a result of near-resonant excitations that activate multiple qualitatively distinct dynamic regimes. Analytical, numerical, and experimental study reveals that these distinct regimes offer energy dissipation behaviors that vary by multiple orders of magnitude. Transitions between regimes can be passively triggered by variations to excitation amplitude or frequency. Introducing asymmetry by biasing the module to one of its two local potential wells results in continuously tunable energy dissipation performance, showing promise for applications that call for large and adaptable energy dissipation for a variety of demanding needs.

Models of cross-bridge energy landscapes commonly depict the pre-power stroke configuration at a higher energy level than the post-power stroke state, meaning that the power stroke element is energetically asymmetric [12]. Asymmetric bistability and multistability is also reflected in the potential energy profile of the shock-absorbing protein titin [45], and may help explain the ability of cross-bridges to store inertial energy from inertial loads and rapidly release it for explosive movements or to reduce the metabolic cost of cyclic motions [8,9,38]. This motivates the second contribution of this thesis, which develops and investigates structures composed of asymmetrically bistable constituents for energy trapping and recovery. Incorporating experimental

study, numerical simulations, and a semi-analytical approximation, the findings could encourage the development of novel structural systems exhibiting attractive energetic properties, such as actuators that effectively capture, store, and release energy, or adaptive, robust, and reusable armors and protective devices.

Across length scales, from whole muscle fiber orientations to sarcomere and cross-bridge compositions, skeletal muscle exploits multidimensionality and oblique motions to modulate or enhance force generation and tension response. In the macroscale, certain muscles exhibit a pennate orientation of muscle fibers to enable force or velocity amplification while minimizing the risk of damage due to over-straining of fibers [7,17,22]. In the microscale, the spacing between adjacent actin and myosin filaments affects cross-bridge mechanics [57], which leads to variation of the length-tension curves of sarcomeres as muscles contract [37]. The third main contribution of this dissertation is on the development, fabrication, and analysis of an architected material system that evokes skeletal muscle's combination of oblique, shearing motions between filaments in a sarcomere, and conformational change during muscle contractions. The architected material demonstrates tailorable discrete, rapid changes in reaction force amplitude and direction. Numerical investigations reveal that these conformation changes coincide with sudden releases of strain energy, and a simple model is presented that offers useful prediction of the behavior of the more complex architected material system.

Chapter 2. Dynamics and energy dissipation in a cross-bridge-inspired metastable mechanical analogue

2.1 Introduction

Skeletal muscle is an effective manager of energy – it stores, converts, and release energy for force generation and length change [14], and is also capable of rapidly dissipating the energy from sudden excitations [11]. Many modern engineering applications would greatly benefit from the availability of structural and material systems demonstrating similarly versatile energy management and dissipation. The assembly of cross-bridges into sarcomere contractile units, as depicted in Figure 2-1, and the integration of bistable cross-bridge constituents with a robust host structure composed of thin (primarily actin) filaments, thick (primarily myosin) filaments, and titin proteins may explain the ability of skeletal muscle to rapidly absorb energy and recover tension when subject to dynamic loads [35,54]. Mechanical systems inspired by this assembly have demonstrated significant potential for the adaptivity of static properties such as stiffness and reaction force [75], strongly suggesting the potential for similar adaptivity in dynamic behaviors.

The use of bistable or negative-stiffness inclusions within positive stiffness host structures for large and adaptable damping has recently been of significant engineering research interest. Advances in multiscale modeling have facilitated an understanding of how material selection and microstructure influence the stability and dissipative performance of such structural and material systems [78,79]. and adaptation in energy dissipation characteristics of composites with negative stiffness inclusions has been demonstrated by varying temperature [80,81]. Numerical study of the

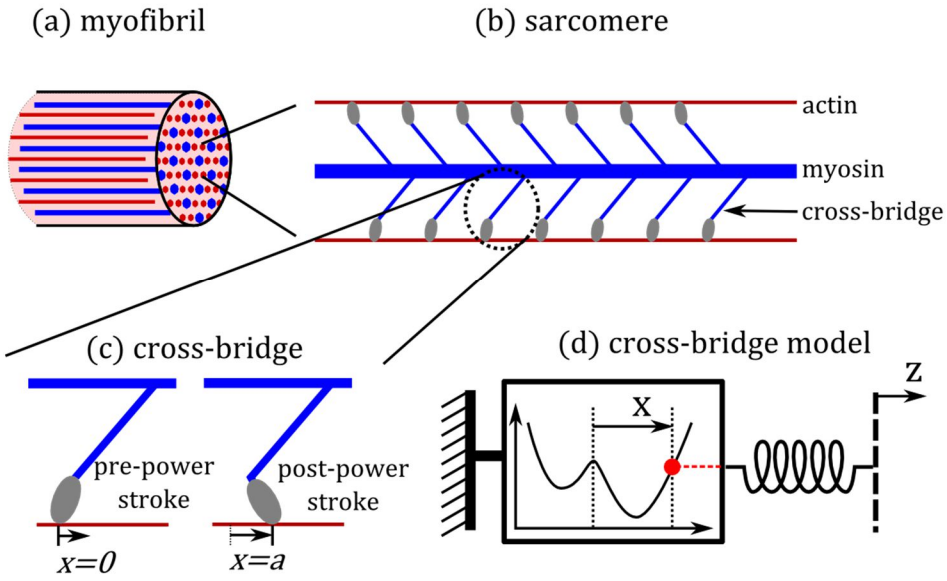

Figure 2-1. Skeletal muscle constituents showing (a) myofibril composed of alternating actin and myosin filaments arranged into (b) sarcomere units. (c) cross-bridges connect adjacent actin and myosin filaments, undergoing a power stroke which results in local conformation changes of the myosin head. (d) A one-dimensional mechanical cross-bridge model presents a bistable element in series with a linear elastic spring [54].

behavior of bistable von-Mises trusses have revealed large changes in damping as device configuration and excitation frequency vary [82], while experimental and theoretical investigations explored the damping enhancement and adaptation facilitated by a compressed spring-mass bistable device [83]. Structures composed of chains of elements with bistable-like interactions between adjacent elements, such as the giant protein titin [43–45] have been shown to demonstrate enhanced shock absorption and dissipation capabilities by exploiting a "reversible rupture" phenomenon [45]. Meanwhile, a one-dimensional chain of elements with bistable on-site potentials can exhibit three different dynamic regimes depending on oscillation amplitude [84].

These works illustrate that negative stiffness inclusions in the form of bistable devices and elements can yield significant energy dissipation under certain conditions. From the viewpoint of system integration in both biological systems and engineered structures, negative stiffness elements often interface with positive stiffness elastic members. A fundamental, one-dimensional, cross-bridge

model is presented in Figure 2-1(d), and consists of a bistable and linear (positive stiffness) springs in series [12,13], which exhibits very different properties compared to an individual bistable element [75].

To clarify the difference, the inset of Figure 2-2(a) shows a mechanical archetype of the one-dimensional constituent module examined in this chapter, equivalent to the simplified cross-bridge model in Figure 2-1(d): a bistable spring (axially-compressed rigid bars joined at a central pivot) connected in series with a linear spring with stiffness coefficient K_L. When the module is constrained by a static, global end displacement Z at the free end of the linear spring, the qualitative behavior of

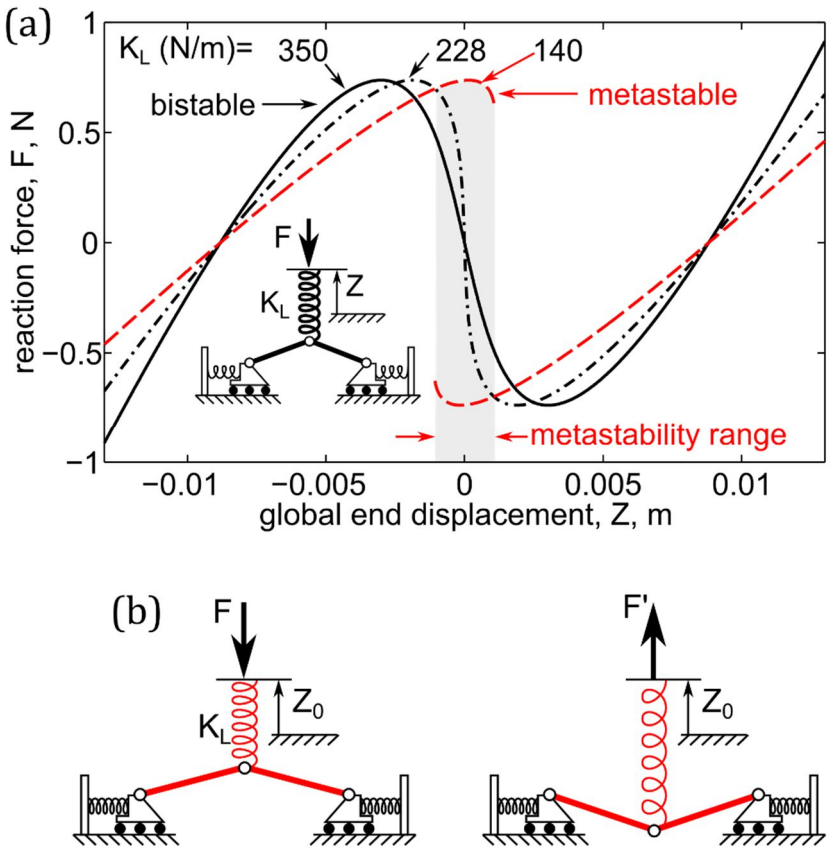

Figure 2-2. (a) Inset: Schematic of the mechanical module that integrates bistable and liner springs in series. Reaction force, F, of mechanical module acted upon by a global end displacement, Z, for three linear spring stiffnesses K_L. (c) For sufficiently small linear spring stiffness, the system exhibits coexisting metastable states evidenced by more than one reaction force for one end displacement.

the reaction force F evaluated at the end varies significantly depending on the relative amplitude of the stiffnesses between the bistable and linear spring constituents.

For example, the black solid curve in Figure 2-2(a) shows the case for which the linear spring is very stiff compared to the bistable spring. Since the *weakest link* of springs in series governs the upper bound on the effective total stiffness, a macroscopic observation taken from the end displacement Z reveals that this module is bistable. It therefore exhibits only one potential reaction force as the global end displacement varies, which is illustrated by the black solid curve in Figure 2-2(a). As the linear spring stiffness K_L is reduced, a dramatic change in mechanical properties occurs. At a critical reduction of the linear spring stiffness, a vertical tangency appears in the force-displacement profile [85], such as that shown for the dash-dot curve. Thus, the continued reduction in the linear spring stiffness leads to two *coexistent metastable states*, shown by the dashed curves. In this chapter, a module having multiple coexisting metastable states over a given range of displacements is referred to as a *metastable module*. The coexisting states are illustrated in Figure 2-2(b) where for one prescribed end displacement Z_0 there are two unique static internal configurations that induce unique reaction forces F and F'. For the mechanical system considered in here, the *metastable range* is defined as the extent of displacements across which the module exhibits a coexistence of metastable states.

Based on the above discussion, integration of negative stiffness (bistable) inclusions or devices into structural/material systems may commonly result in a system possessing coexisting metastable states, and the unit-level module of such a phenomenon serves as a suitable model to explore the global features [78,86]. While such metastable modules have been examined for their quasi-static properties [79–81], much remains to be understood regarding the dynamics and energy dissipation characteristics of metastable modules under dynamics loads. Excitations at frequencies near the linearized resonant frequencies of the stable states are particularly important, since near-resonant excitations are substantially more influential on the activation of large amplitude snap-through

dynamics in individual bistable devices, [87] and damping change has greater impact around system resonances.

In the remainder of this chapter, the dynamic characteristics of a metastable module are studied under near-resonance excitations to identify how the various dynamic states may be leveraged to achieve large and adaptable energy dissipation properties at the unit module level. The study considers an archetypal mechanical metastable module as presented in Figure 2-2. The following subsections introduce the experimental platform and corresponding one degree-of-freedom (DOF) model of the metastable module, then present analytical, numerical, and experimental investigations to evaluate the effects of excitation parameters on the energy dissipation properties effected via near resonant excitation.

2.2 A metastable module for dynamic analysis

2.2.1 Experimental setup

The experimental system studied here is depicted in Figure 2-3, and represents the essential constituents required to closely examine the dynamics of an individual metastable module. A polycarbonate base (a) supports a suspension system consisting of a pair of parallel, thin spring steel beams (b) clamped at the ends. At the center of each spring steel beam suspension is a miniature ball bearing that serves as a mount for a rigid, rotating arm (c). The other ends of the arms are pinned together at a center point between the suspensions using similar bearings in the arms and a shared axle. The net length of the two rotating arms is greater than the distance between the suspension system ends and thus the sub-system is bistable. Due to the compliance provided by the suspensions, the rigid arms may rotate between the two stable equilibria. The configuration used throughout experimentation is designed such that the two stable equilibria of the bistable constituent are at ±10° with respect to a line normal to the suspension beams. These prior elements represent the bistable

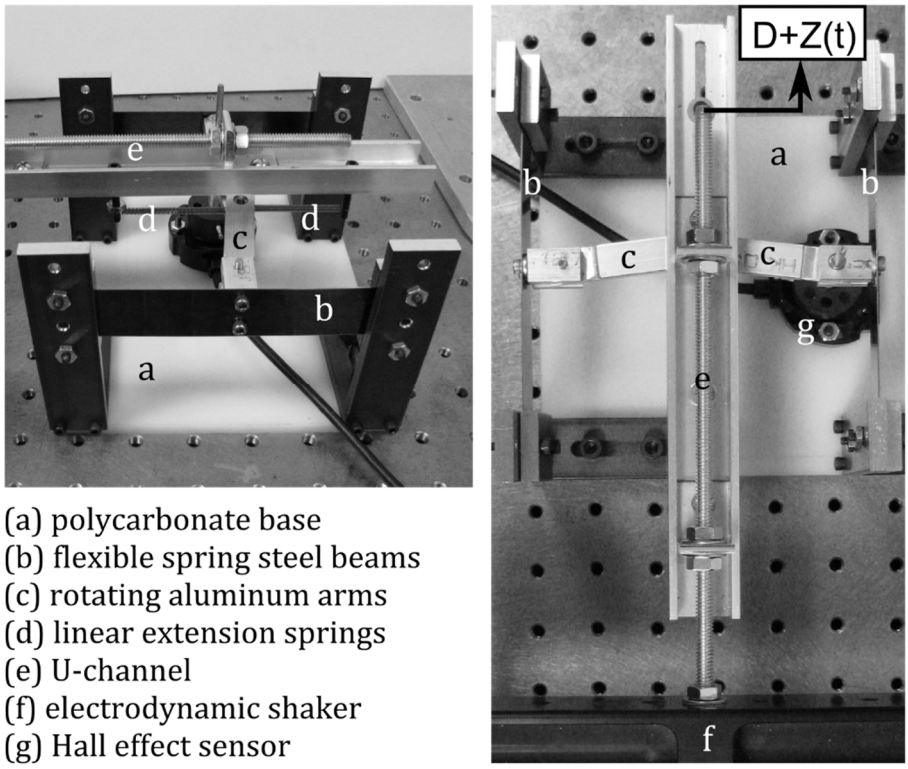

(a) polycarbonate base
(b) flexible spring steel beams
(c) rotating aluminum arms
(d) linear extension springs
(e) U-channel
(f) electrodynamic shaker
(g) Hall effect sensor

Figure 2-3. Experimental metastable module and experimentation components. The configuration used throughout experimentation is such that the two stable equilibria of the bistable constituent are at $\theta = \pm 10°$.

spring of the metastable module. A pair of linear tension springs (d) connects the shared axle that joins the two rotating arms to bolts protruding from a rigid U-channel beam (e). The tension springs are always extended from the relaxed lengths to avoid the possibility of the spring bottoming out or buckling. The U-channel beam, to which the tension springs are connected, is fixed to a controlled electrodynamic shaker (APS ELECTRO-SEIS 400, APS Dynamics) (f). The position of the shaker represents the global end displacement for – and excitation to – the metastable module. The bolts connecting the U-channel to the springs may be moved to generate a static offset to the excitation.

Experiments are conducted to verify that the U-channel beam is sufficiently rigid to eliminate resonant dynamics of the U-channel in the frequencies of interest. The energy dissipation mechanisms present in the system are primarily the result of viscous damping in the deformation of the springs and suspension beams, as well as the unavoidable friction in the bearings. To monitor the

excited dynamics of the metastable module, the rotation of the rigid arms is measured using a Hall effect sensor (RFC-4801, Novotechnik) (g) attached to the pinned axle that connects one arm to a suspension, as shown in Figure 2-3. Additionally, the input shaker acceleration is monitored by an accelerometer (PCB 352 C33, PCB Piezotronics).

2.2.2 Model formulation and governing equation

The experimental module shown in Figure 2-3 is modeled using the schematic of Figure 2-4 and the governing equation of motion is derived using energy principles. The mass taken into consideration here consists only of the rigid rotating arms, while the masses of the other components of the module relative to the arms are assumed to be negligible. The total kinetic energy of the module may then be derived as

$$T = 2\left[\frac{1}{2}\left(I_p + M\frac{L^2}{4}\right)\right]\dot{\theta}^2 \tag{2-1}$$

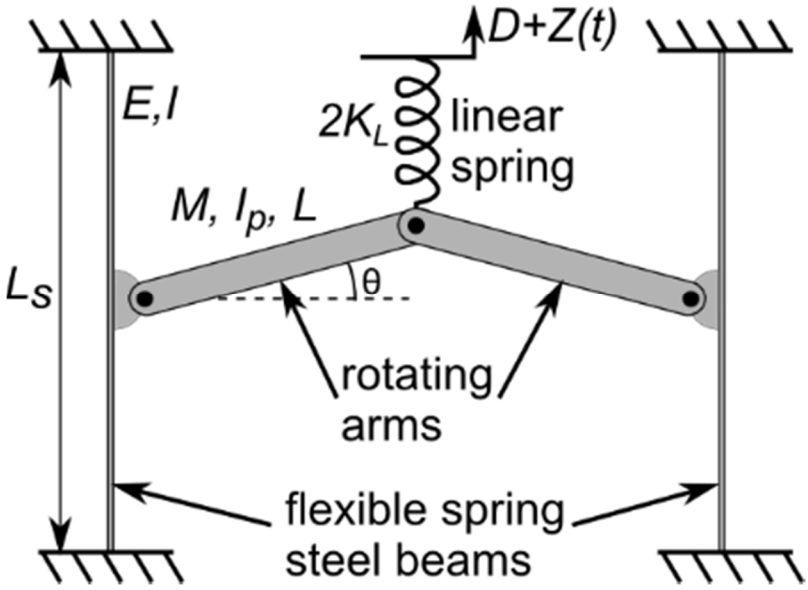

Figure 2-4. Schematic of the experimental metastable module.

The rotation of both arms is expressed using one common angular displacement $\theta(t)$. M is the mass of each rotating arm of length L, and I_p is the moment of inertia of each rigid arm about an axis through its center of mass, perpendicular to the plane shown in Figure 2-4. The parallel axis theorem is applied to obtain the moment of inertia of the rigid arm about its pinned end. The potential energy stored in the suspension beams may be written as

$$U_1 = 2\frac{192EI}{L_s^2}\left[1 - \theta\sin(\theta) - \cos(\theta) + \frac{1}{2}\theta^2\cos(\theta_0)\right] \tag{2-2}$$

where E is the Young's modulus of the suspension beam, I is the area moment of inertia about the neutral axis of bending, L_s is the length from clamp to clamp of each suspension, and θ_0 is the angular position of the arms that results in the absence of the connection to the linear springs. The term $192EI/L_s^3$ is the effective, one-dimensional spring stiffness of a clamped-clamped beam with an applied load at the center point [88]. The potential energy stored in the linear springs is

$$U_2 = K_L[Z + D - L\sin(\theta)]^2 \tag{2-3}$$

where tension spring stiffness is K_L, D refers to a static offset of the periodic excitation Z from the neutral position of the bistable device. In other words, a non-zero offset D biases the system towards one of the two potential wells. The offset is adjusted experimentally by changing the pre-tension on one of the linear springs. Dissipation is approximated by a viscous damping force proportional to the angular velocity of the rigid, rotating arms according to the coefficient B, whose value is determined by fitting numerical results to experimentally measured data of the free decay response. Lagrange's equations are used to yield the governing equation of motion for the rigid arm rotation θ in consequence to certain end displacement motions Z:

$$\left(\frac{ML^2}{2} + 2I_p\right)\ddot{\theta} + B\dot{\theta} + 2K_L L^2\sin(\theta)\cos(\theta)$$

$$-\frac{384EI}{L_s^2}\theta[\cos(\theta) - \cos(\theta_0)] - 2K_L L\,(Z + D)\cos(\theta) = 0 \tag{2-4}$$

In this study, the global energy dissipation of the metastable module due to harmonic excitations of the end displacement, $Z(t) = Z_0 \cos \Omega t$, is quantified by computing the area enclosed in the hysteresis loops of reaction force and end displacement. The reaction force due to the deflection of the linear springs is defined in Eq. (2-5). In addition to the apparent spring force contribution, the reaction force also reflects inertial and energy dissipation phenomena due to the influences of the rotations θ of the internal moving arms.

$$F(t) = 2K_L[Z + D - L\sin(\theta)] \tag{2-5}$$

2.3 Approximate analytical solution of steady state dynamics

2.3.1 Model transformation and equivalent governing equation

Eq. (2-4) may be directly integrated via numerical methods to predict the response and energy dissipation properties due to a particular selection of design and excitation parameters for the metastable module. However, to obtain more comprehensive insights on the potential dynamic behaviors, an approximate analytical strategy to solve the governing Eq. (2-4) is undertaken. As a first step towards the application of an approximate solution, the restoring forces in Eq. (2-4) are expanded via a Taylor series around θ = 0, retaining terms up to the third order.

$$\left(\frac{ML^2}{2} + 2I_p\right)\ddot{\theta} + B\dot{\theta} - \frac{384EI}{L_s^2}[1 - \cos(\theta_0)]\theta + [K_L L(Z + D)]\theta^2 + \left(-\frac{4}{3}K_L L^2 + \frac{192EI}{L_s^2}\right)\theta^3 - 2K_L L(Z + D - L\theta) = 0 \tag{2-6}$$

By performing a coordinate transformation around a stable angular equilibrium θ_0 of the internal bistable element when disconnected from the linear spring [89], and by applying the arc length relationship ($x = L\theta$) to relate the displacement of the center axle joining the rigid arms x to the angular rotation of the arms θ, the following governing equation may be obtained

$$m\ddot{x} + b\dot{x} + k_1 x + k_2 x^2 + k_3 x^3 - k_L(z + d - x) = 0 \tag{2-7}$$

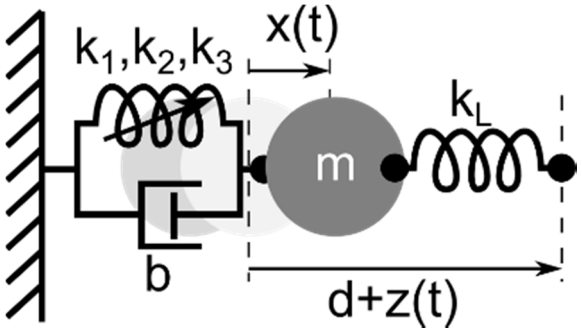

Figure 2-5. Schematic of the transformed model formulation of the metastable module.

where m is the lumped internal mass, and k_1, k_2, k_3 are the linear, quadratic, and cubic stiffness coefficients, respectively. Figure 2-5 shows a schematic representation of the metastable module using the parameters expressed in Eq. (2-7). With the restoring forces of the module approximated by the power series in terms of the displacement x, the governing Eq. (2-7) may be approximately solved using a variety of assumed solution techniques to predict the steady-state behaviors [90].

A harmonic balance solution is employed in this chapter, and further details and derivation are provided in Appendix A. A fundamental assumption of the harmonic balance method is that system responses are periodic, which is often untrue in lightly damped nonlinear systems such as the one studied here [89]. Under certain experimental conditions, period doubling and chaotic responses were sometimes observed. Such behaviors are not reflected in the analytical approach presented here. Stable, steady-state results of the oscillation amplitude r predicted by the harmonic balance method are compared with the experimentally measured results of angular rotation magnitude $|\theta|$. Additionally, for further quantitatively meaningful comparison, Eq. (2-4) is numerically integrated The dynamic reaction force $F(t)$ from Eq. (2-5) is compared to the corresponding measured result using common system parameters.

2.4 Steady state dynamic response at near-resonant excitations

It is well-known that structures containing buckled members may more readily exhibit strongly nonlinear dynamics when excited near resonance, [87] and this feature has previously been exploited to achieve high and adaptable damping using an individual bistable oscillator [83]. But the ways in which such an excitation comparably influence the dynamics of metastable modules, like the one studied here with bistable-linear spring integrations, remain poorly understood.

To investigate the frequency dependence of the near-resonant harmonic excitation, experimental excitation frequency sweeps are performed at fixed amplitude using very slow sweep rates of ± 0.05 Hz/s to ensure that steady-state responses are correctly identified and that all potential dynamic states are realized by sweeping both up and down in frequency. First, the examinations consider the case in which the offset parameter D is set such that the mean value of the harmonic excitation corresponds to the central unstable equilibrium position of the internal bistable device of the metastable module. For the offset D satisfying the condition described above, the linear spring stiffness K_L is selected such that the module exhibits coexistent metastable states. Experimental model parameters are presented in Table 2-1. Parameters used in the transformed model to gain initial qualitative predictions are presented in Table 2-2, while Table 2-3 shows parameters of the transformed model derived directly from the experimental system.

Table 2-1. Experimental system parameters used in numerical simulations of a harmonically excited metastable module

M (g)	I_P (kg.m^2)	L (cm)	E (GPa)	I (m^4)
12	2.74×10^{-6}	5.08	180	5.46×10^{-15}
L_s (cm)	θ_0 (°)	K_L (N.m^{-1})	B (N.s.m^{-1})	
9.82	±10	84	1.5×10^{-4}	

Table 2-2. Transformed model parameters used in analytical solution.

m (kg)	k_1 (N.m^{-1})	k_2 (N.m^{-2})	k_3(N.m^{-3})	k_L (N.m^{-1})	b (N.s.m^{-1})
1	2	-3	1	0.5	0.05

Table 2-3. Analytical model parameters derived from experimental system.

m (kg)	k_1 (N.m^{-1})	k_2 (N.m^{-2})	k_3(N.m^{-3})	k_L (N.m^{-1})	b (N.s.m^{-1})
2.10 ×10^{-5}	-0.595	0	19.4	0.434	1.5×10^{-4}

Figure 2-6 presents (a,b) experimental and (c,d) analytical results of the rigid arm rotation and displacement amplitudes, respectively. In the experiments, the harmonic excitation frequency varies

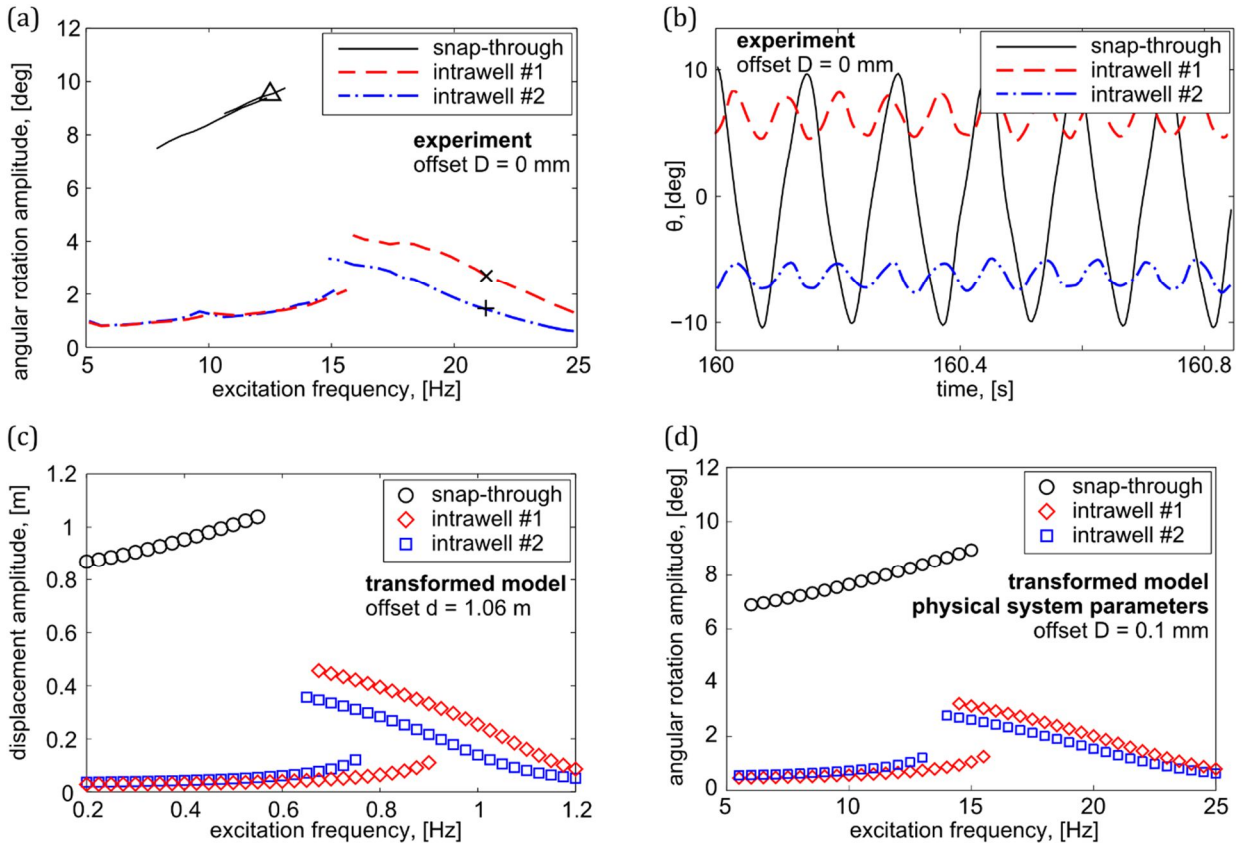

Figure 2-6. (a) Experimentally measured angular rotation amplitude of the rigid arms. The three data marked points are provided as reference to time-series results presented in (b), and to the hysteresis loops presented in Figure 2-7. (c) Analytical predictions of the displacement amplitude as the excitation frequency is varied, showing qualitative agreement with experiment. (d) Analytical predictions employing parameters derived from the experimental system shown in Table 2-3, demonstrating quantitative agreement with experiment.

from 5 to 25 Hz with a constant excitation amplitude Z_0 = 300 μm. Statically stable equilibria of the bistable constituent of the experimental module are at angular positions $\pm 10°$. The transformed analytical model, Eq. (2-7), is evaluated between normalized frequencies of 0.2 Hz and 1.2 Hz, with excitation amplitude z_0 = 0.06 m. Both the experimental and analytical results reveal two distinct dynamic regimes: intrawell and interwell. Time-series responses of both types of oscillations are presented in Figure 2-6 (b). *Intrawell* responses oscillate around a statically stable equilibrium. As described using the illustration of Figure 2-2, the system possesses two local wells of potential energy for some configurations of the module. Hence, it exhibits a coexistence of metastable states for a prescribed end displacement Z. For clarity, these two local wells are referred to throughout the rest of this chapter as *well #1* and *well #2*. Intrawell responses observed in these potential wells are labeled in all figures as *intrawell #1*, and *intrawell #2*, respectively. Interwell (i.e., *snap-through*) responses are characterized by displacements which cross the unstable equilibrium of the internal bistable constituent.

Intrawell and snap-through response behaviors are exhibited by individual bistable oscillators [91], and are observed here due to the internal bistable element within the metastable module and the corresponding module design and excitation parameters. For the excitation offset D = 0 mm, the metastable module displays two statically stable equilibria. Since the excitation amplitude Z_0 is sufficiently small, two distinct intrawell-type dynamics are activated, as shown in Figure 2-6(a,b) by the dashed and dash-dot curves. This is a unique co-existence of dynamics not manifest in an individual, displacement-driven bistable device. For certain excitation frequencies, namely those close to 15 Hz, two different intrawell responses are observed for each of the intrawell-type behaviors: *low* and *high amplitude* intrawell. In particular, these two responses are realized due to the near-resonant excitation frequencies. The continuous snap-through oscillations, shown by a solid line in Figure 2-6(a), are observed at excitation frequencies between 8 Hz and 14 Hz, with much greater response amplitudes than either of the intrawell oscillations. Due to the differences in the

angular rotation amplitudes amongst each dynamic type across the near-resonant frequencies explored here, the kinetic energy of the dynamic regimes are distinct. Because the metastable module possesses internal damping mechanisms, a wide variation of energy dissipation capabilities is correspondingly achieved, and is shown to be governed by the harmonic excitation frequency in this case.

The excitation offset position D = 0 mm is presumed to be centered on the unstable equilibrium of the internal bistable element. Hence, an ideal, symmetric, module should exhibit identical intrawell responses. Yet, the different response amplitudes, particularly for the high amplitude intrawell responses found at frequencies greater than 15 Hz, indicate that the experimental metastable module is slightly asymmetric. Note that due to the coordinate transformation performed to reduce Eq. (2-6) to the equivalent form presented in Eq. (2-7) and according to the transformed model parameters employed (Table 2), the symmetric offset position for the analytical model is d = 1 m. To reflect the small asymmetry in the analytical model for qualitative comparison purposes, a static offset of d = 1.06 m is included in the calculation of the analytical results presented in Figure 2-6(c). The resulting analytical predictions shown in Figure 2-6 show good qualitative agreement with the corresponding measurements. They reveal distinct low and high amplitude intrawell responses in both potential wells, as well as the higher amplitude snap-through oscillations at low excitation frequencies. Derivation of the transformed model parameters from the exact formulation in Eq. (2-4) to the form in Eq. (2-7) yields the analytical results presented in Figure 2-6(d), demonstrating quantitative in addition to qualitative agreement with the experimental results.

2.5 Influence of excitation parameters on system response

2.5.1 Excitation frequency influence on energy dissipation

The activation of numerous distinct dynamic responses from the near-resonant excitations suggests that the energy dissipation characteristics are also distinct. To quantify the energy dissipated over one excitation period, the reaction force F as defined in Eq. (2-5) is plotted against global end displacement Z over one excitation period. Using $W = \int F \cdot \mathrm{d}Z$, the work W done by the reaction force may be calculated over one period of excitation. Since the excitation and response are periodic, the force-displacement trajectory forms a loop. The area enclosed by this loop, resulting from damping-induced hysteresis, is the work done by the reaction force, and is equal to the energy dissipated by the module over a single excitation period [92].

The solid curves in Figure 2-7(a) present the hysteresis loops of a snap-through response obtained from the experimental time-series data using an excitation frequency of 12.5 Hz, as well as both intrawell responses observed at an excitation frequency of 22 Hz, all using an offset of D = 0 mm. These excitation conditions correspond to the angular rotation amplitude data point in Figure 2-6(a) indicated by the triangle for the snap-through response, and the multiplication and addition

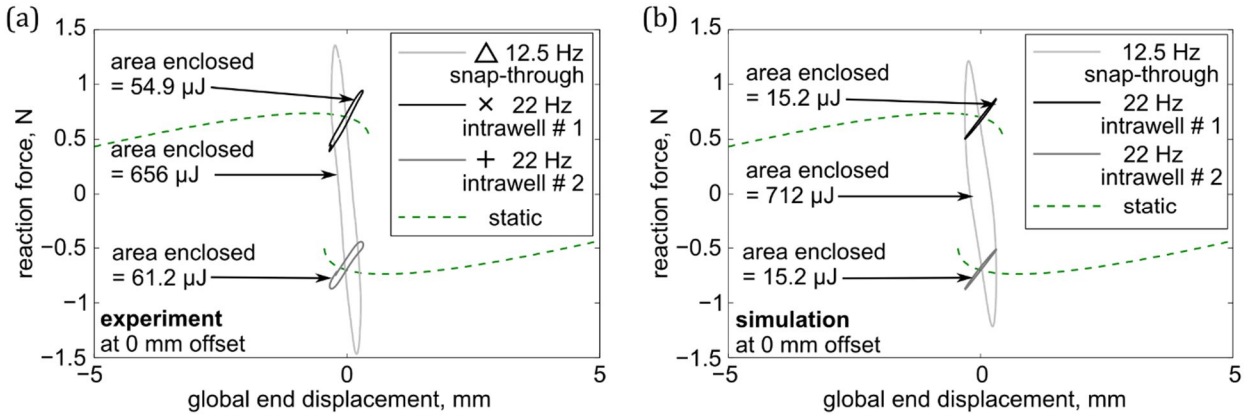

Figure 2-7. (a) Experimental and (b) simulated hysteresis loops (solid curve) of a snap-through response at 12.5 Hz excitation, and an intrawell response at 22 Hz excitation with 0 mm offset. Symbols in the legend of (a) correspond to the respective conditions from Figure 2-6(a).

symbols for the intrawell #1 and intrawell #2 responses, respectively. The solid curves in Figure 2-7(b) show the corresponding simulation results obtained by numerically integrating Eq. (2-4) which is the governing equation of motion for the experimental system. The plots also show dashed curves which are the corresponding static force-displacement profiles. The static profiles are determined by solving Eq. (2-6) under static conditions and for a fixed global end displacement Z. Similar to the dashed curve in Figure 2-2(a), the static force-displacement characteristics for the metastable module studied here demonstrate a range of global end displacements for which two metastable states occur. The snap-through result of Figure 2-7(b) demonstrates good agreement with the experimental result in Figure 2-7(a), and shows large reaction force amplitudes having a mean value over the loop which is approximately zero. This suggests that the dynamic reaction force behavior is associated with snap-through, since there is no force bias typical of intrawell oscillations. In fact, examinations of the experimental and simulated time-series data, such as the results of Figure 2-6(b), confirm that the dynamic responses are correctly identified as snap-through, since the rotating arms oscillate across the central, unstable equilibrium twice per excitation period. Furthermore, the snap-through hysteresis loops display a negative mean slope, indicating the presence of negative dynamic stiffness in this regime [92]. The large displacement amplitude of the internal coordinate in the snap-through regime corresponds to large deflections of the linear springs. Due to the more significant internal deformations and the damping present in the module, a large dissipation of energy is achieved for relatively small excitation amplitudes of the global end displacement.

It is clearly seen that each of the intrawell responses in Figure 2-7 are confined to a single potential well around a static equilibrium, resulting in a smaller hysteresis loop and consequently much lower energy dissipation per excitation cycle than the snap-through case. The per-cycle energy dissipation predicted by simulation for the intrawell cases in Figure 2-7(b) is 15.2 μJ, which is lower than the 54.9 μJ and 61.2 μJ of energy dissipated in the experimental system. This could be due to the

unmodeled stick-slip friction in the bearings of the experimental metastable module, which have the effect of increasing damping for low amplitude oscillations. Thus, there is greater deviation in the values of the area enclosed in the hysteresis loops between the measurements and simulations for the small amplitude intrawell dynamics than for the corresponding measures for the large amplitude snap-through responses.

As seen in Figure 2-6, excitation frequency is one factor that determines whether intrawell or snap-through responses are activated. Small changes in frequency may maintain a given response type although the response amplitude and phase may smoothly vary. Consider Figure 2-8 which shows experimental and simulated hysteresis loops of snap-through responses as the excitation frequency is varied from 10 Hz to 14 Hz. The area enclosed by the loops, and consequently the energy dissipated per excitation cycle, increases with the increase in frequency. This finding is consistent with results presented in Figure 2-6(a), which show snap-through response amplitudes increasing with frequency. As the arm rotation angle amplitude increases, the deflection of the linear springs likewise grows in magnitude. Consequently, the reaction force amplitude also increases according to Eq. (2-5). This results in the steady magnification of the hysteresis loops as the frequency increases from 10 to 14 Hz in Figure 2-8. Similar to the results of Figure 2-7, good overall agreement is seen

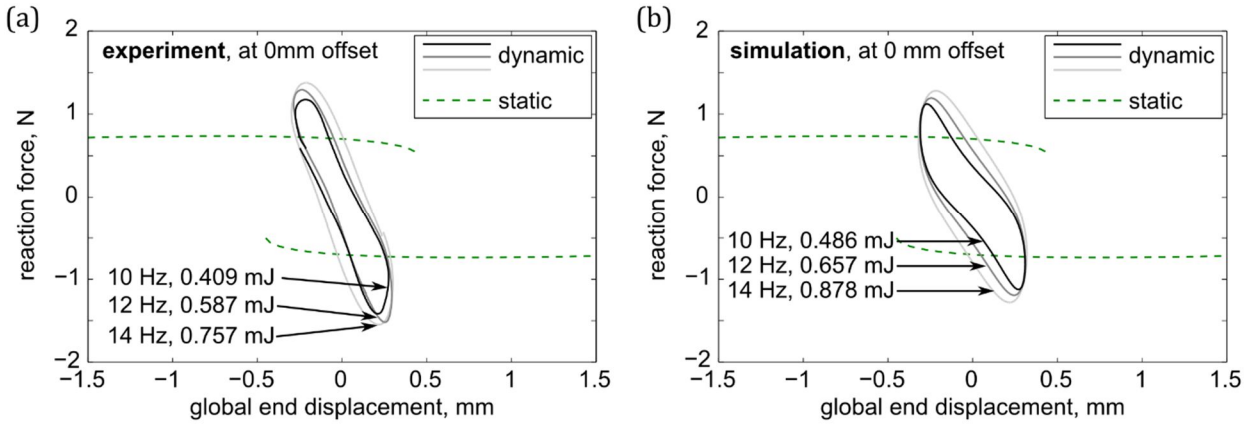

Figure 2-8. (a) Experimental and (b) simulated hysteresis loops (solid curves) of snap-through response at 0 mm offset at different excitation frequencies.

comparing the experimental results in Figure 2-8(a) of the snap-through dynamics with the behaviors predicted from the direct simulations of the model governing equations as shown in Figure 2-8(b).

The results suggest that energy dissipation performance is affected by excitation frequency in the following two ways. First, the excitation frequency influences which dynamic response regimes are realizable. Intrawell and snap-through responses induce particularly different hysteresis loops due to the much larger amplitudes of arm rotation triggered by the snap-through behaviors. Thus, large adaptation of energy dissipation (orders of magnitude) may be accomplished. Second, small changes in excitation frequency that maintain a particular response regime may have a lesser, but still appreciable, effect on the energy dissipated per cycle. In this way, a refined modulation of the energy dissipation may be induced.

2.5.2 Excitation level influence on system response and energy dissipation

Excitation level is shown to have a strong influence on the dynamic behavior of bistable oscillators [83,93], and is expected to exert similarly strong influence on the metastable module as well. To study the influences, several excitation amplitude sweeps are performed at fixed excitation

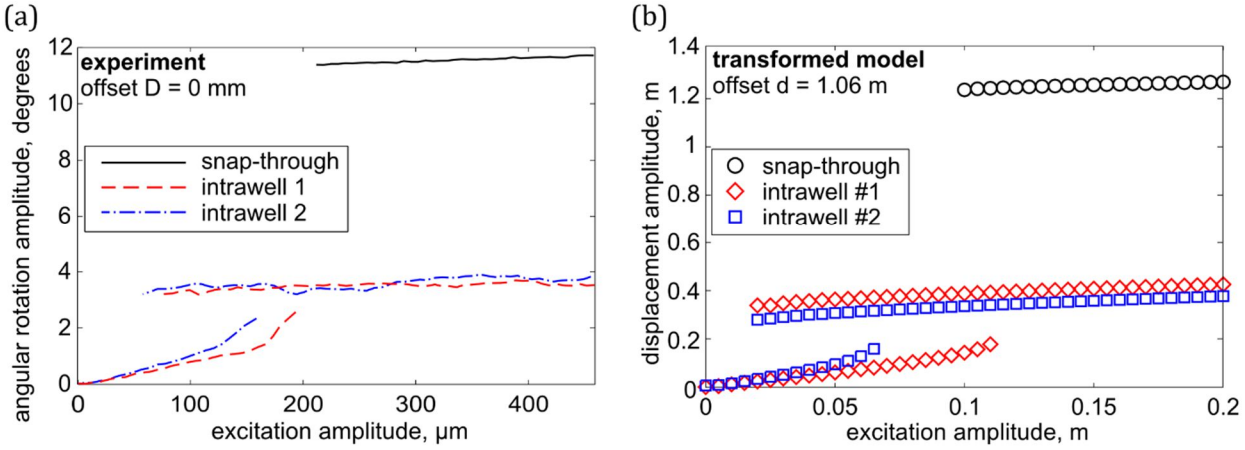

Figure 2-9. (a) Experimental and (b) analytical results of the influence of excitation amplitude on the internal dynamics of the metastable module when excited at constant frequency.

frequencies. Figure 2-9(a) presents the experimental results of an excitation amplitude sweep from 0 to 450 μm at a rate of 2.25 μm/s, with constant excitation frequency $\Omega/2\pi$ = 17 Hz. Figure 2-9(b) shows analytical model results, computed using an excitation frequency $\omega/2\pi$ = 0.8 Hz and with the model parameters given in Table 2. Similar to the good agreement seen in Figure 2-6, the comparisons in Figure 2-9 indicate that the analytical model provides a meaningful prediction of the qualitative behaviors observed experimentally when the excitation amplitude is varied while the excitation frequency remains constant. Both the experimental and analytical results show the presence of low amplitude intrawell oscillations only at low excitation levels, and a range for which low and high amplitude intrawell responses coexist. Snap-through responses are observed at high excitation amplitudes. The high amplitude intrawell and the snap-through regimes show fairly constant response amplitudes over a large range of excitation amplitudes, indicating significant robustness to changes in excitation level.

Figure 2-9 indicates that the existence or coexistence of dynamic response regimes is strongly influenced by excitation amplitude. To demonstrate how these trends correspond to energy dissipation performance, Figure 2-10(a), (b), and (c) show hysteresis loops at 200 μm, 300 μm, and 450 μm excitation amplitudes, respectively for a fixed 17 Hz excitation frequency, and offset D = 0 mm. It is observed that as excitation amplitude is increased, the amount of energy dissipated in a particular response regime is slightly increased, consistent with the results presented in Figure 2-9(a).

Thus, the excitation amplitude influences the energy dissipation characteristics in a comparable manner to excitation frequency. First, excitation amplitude affects the dynamic response regimes that are realizable, where each regime results in different energy dissipation. At very low excitation levels, only low amplitude intrawell responses are observed. As excitation level increases, the low amplitude intrawell responses vanish while high amplitude intrawell and snap-through responses are activated. Second, increased excitation amplitude increases the amount of energy dissipated per

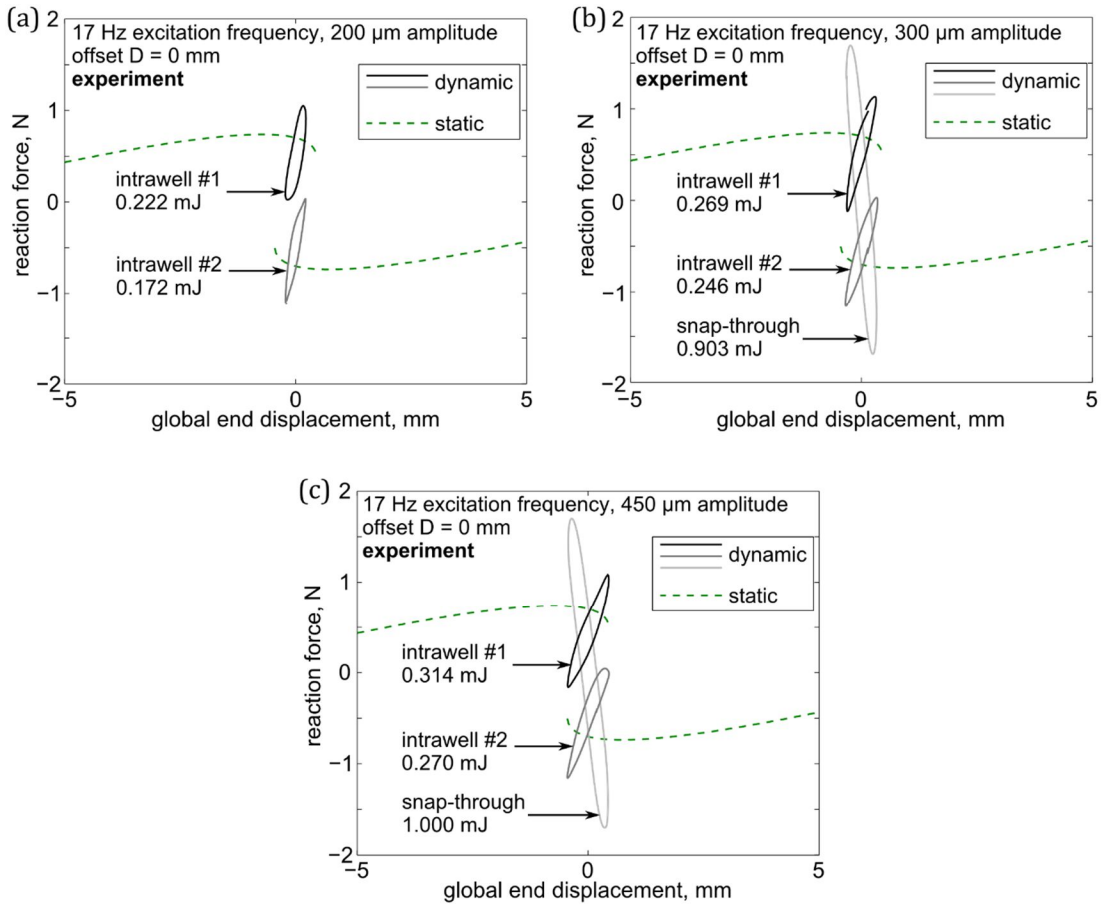

Figure 2-10. Experimental hysteresis loops (solid curves) at D = 0 mm offset, 17 Hz excitation frequency and (a) 200 μm, (b) 300 μm, and (c) 450 μm excitation amplitude. Response type and area enclosed by each loop are indicated.

excitation cycle for a fixed response regime. This is a desirable characteristic in practice, where greater excitation levels typically call for increased damping and energy dissipation performance.

2.5.3 Offset influence on system response and energy dissipation

Thus far, the studies have focused on excitations that are nominally symmetric about the unstable equilibrium position of the internal bistable element of the metastable module. However, once the excitation is applied with an offset from the symmetric condition, asymmetry may appear in the dynamic response, since the bistable constituent of the metastable module is under an additional

static force ($K_L D$). In engineering practice, such a load may be representative of a mass supported by the module under gravitational body forces.

The influence of introducing a static offset D that modulates the symmetry of the system on the steady-state dynamics of the module due to are examined in Figure 2-11 and Figure 2-12. Fixed excitation amplitudes Z_0=300μm and z_0=0.06m are employed in experiment and the analytical model, respectively. Figure 2-11(a) presents experimental results where the excitation offset D is 0.7 mm deflected from the neutral position, while Figure 2-11(b) shows qualitatively similar analytical results for the offset of d = 1.2 m. The offset biases the metastable module towards well #1; the dynamics of this state are shown using dashed curves and diamonds in Figure 2-11(a) and (b), respectively. The asymmetry results in a greater bandwidth of frequencies for which the steady-state intrawell responses occur when the internal mass is confined to well #1, whereas the frequency range of existence for motions in well #2 is greatly diminished (dash-dot curves and squares in Figure 2-11(a) and (b), respectively). Qualitatively, the change in offset plays a key role in tailoring the local linearized resonant frequencies of the intrawell behaviors, and thus governs the frequency bandwidths across which each set of low and high amplitude intrawell dynamics may occur. As a

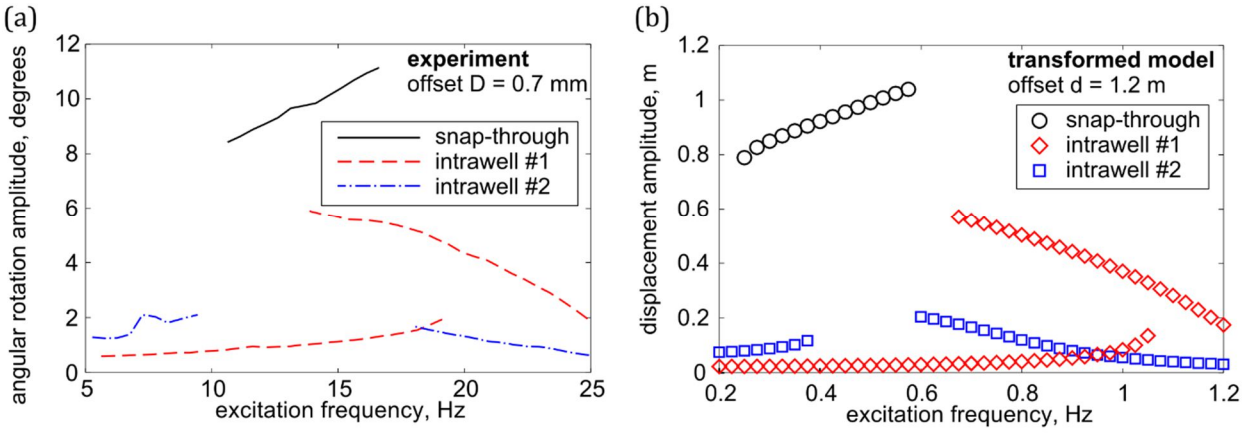

Figure 2-11. (a) Experimental and (b) analytical results showing the internal dynamics of the metastable module as excitation frequency is varied, while the excitation amplitude and offset remain fixed.

result, the energy dissipation characteristics of these regimes are strongly controlled via offset modulation.

Furthermore, in comparing the experimental and analytical results from Figure 2-6 to those in Figure 2-11, the frequency bandwidth for which snap-through motions are observed is modulated. In other words, the offset has the effect of tailoring the bandwidth of frequencies for which the large dissipation capability of the snap-through dynamics is realized. The asymmetry introduced by the static offset also causes the intrawell #1 and #2 responses to exhibit notably different response amplitudes for the same excitation frequency. Collectively, the results show that application of an offset to the harmonic excitation of the metastable module leads to a versatile range of energy dissipation performance according to the operating frequency and amplitude of the induced dynamics of the internal bistable element.

When the offset is further increased to D = 1.4 mm in the experiment, as shown in Figure 2-12(a), well #2 is no longer statically stable, and no steady-state intrawell responses are found in well #2 at any frequency. Analytical results in Figure 2-12(b) with an offset of d = 1.3 m demonstrate similar behavior. Compared to Figure 2-11, the size of frequency bandwidth for which the same type of intrawell responses in well #1 exist is further increased. However, the absence of stable intrawell

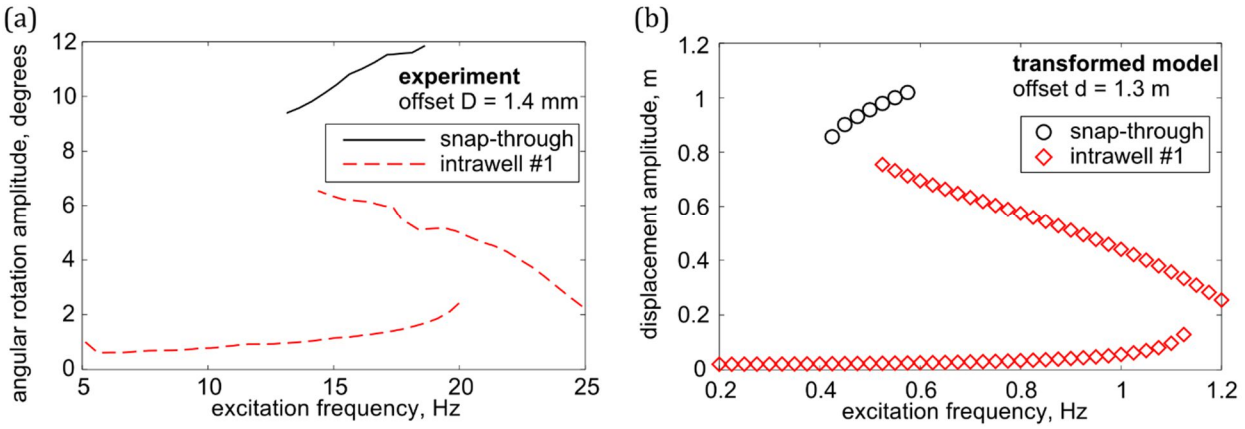

Figure 2-12. (a) Experimental and (b) analytical results showing the internal dynamics of the metastable module as excitation frequency is varied, while the excitation amplitude and offset remain fixed. A greater offset is used than that employed for the results shown in Figure 2-11.

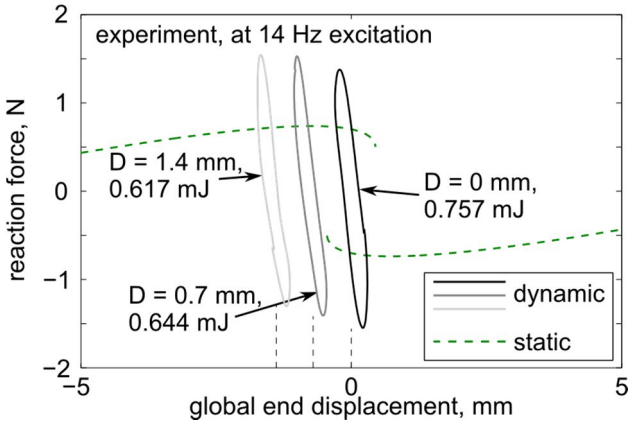

Figure 2-13. Experimental hysteresis loops (solid curves) for snap-through responses at 14 Hz excitation. Excitation offset and area enclosed by each loop are indicated.

responses in well #2 means that fewer frequencies exhibit multiple coexistent responses regimes, compromising some energy dissipation adaptability. Considering the snap-through responses from Figure 2-6 to 2-11 to 2-12, it is apparent that change in the excitation offset from a near-symmetric excitation condition has the effect of modulating the bandwidth of frequencies for which the snap-through motions occur. In particular, an increase of the offset increases the lower and upper frequency extents of the bandwidth although the total bandwidth is seen to remain relatively constant. This finding suggests a novel bandpass filter feature may be realized for the metastable module in terms of triggering large damping associated with the snap-through behaviors for a particular range of excitation frequencies.

While the introduction of a non-zero static offset to the excitation affects the frequency ranges in which the different response regimes are observed, certain excitation frequencies exhibit the same response regime at all three offsets D = 0 mm, 0.7 mm, and 1.4 mm, permitting an analysis of the impact of offset on energy dissipation performance. For example, Figure 2-13 presents measured hysteresis loops for snap-through responses when excited at 14 Hz. As the offset is increased (shown by the increasing lightness of the solid curves), the centers of the hysteresis loops move towards the statically stable well, although the amount of energy dissipated per cycle varies only slightly. This

indicates that the energy dissipation performance in the snap-through regime is robust to small changes in excitation offset. Such behavior is useful for applications in which high energy dissipation is desired but equivalent offset influences vary over time, such as change in applied dead loads or supported weights.

As evidenced by the frequency sweep results presented in Figure 2-11 and Figure 2-12, excitation offset may affect which response regimes are physically realizable even when excitation frequency and amplitude are fixed. This, in turn, influences the energy dissipation behaviors. Experimental and simulation results presented in Figure 2-14 summarize this feature for an excitation frequency of 16 Hz. At the zero offset position, only high amplitude intrawell responses are observed as denoted by the hysteresis loops shown in Figure 2-14(a) and (d). As the offset is increased to D = 0.7mm, intrawell responses in well #2 responses disappear, while low amplitude intrawell responses in well #1, and large, snap through responses are observed. These responses are also observed at an offset

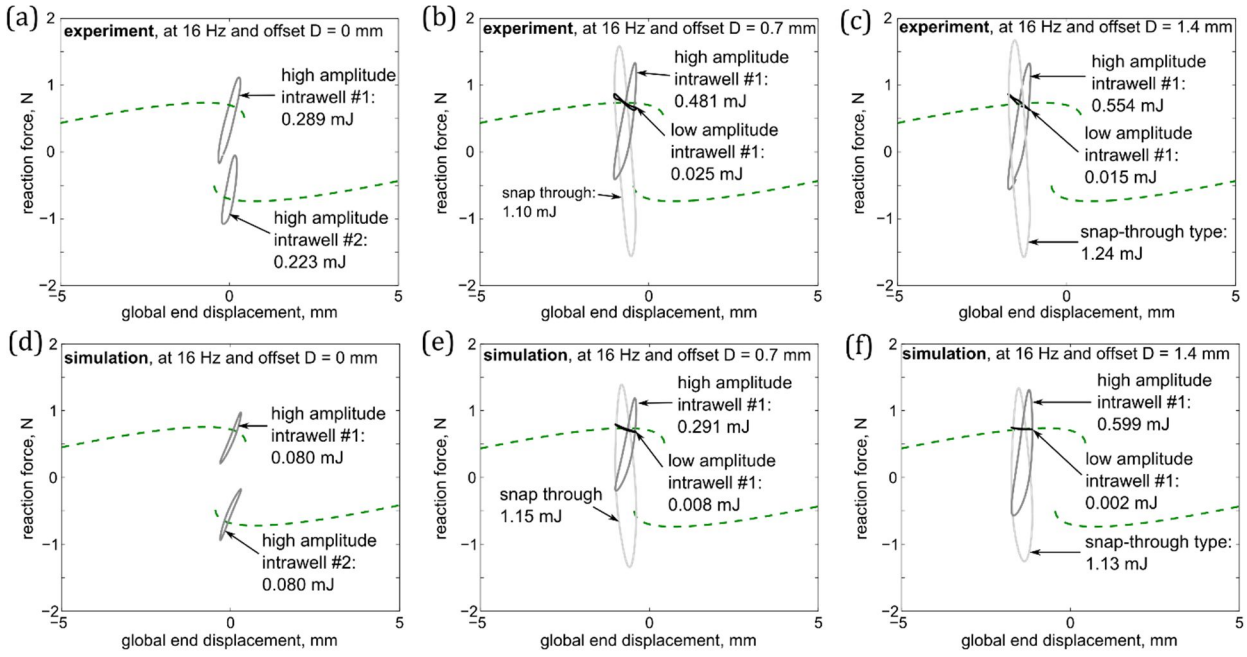

Figure 2-14. Hysteresis loops showing energy dissipated per cycle computed as the area enclosed by the loops, at 300 μm excitation amplitude and 16 Hz frequency. (a-c) Experimental and (d-f) simulated results are shown for: (a,d) D = 0 mm, (b,e) D = 0.7 mm, and (c,f) D = 1.4 mm. Loops plotted over static force-displacement profile (dashed curves).

of D = 1.4 mm, though with slightly different response amplitudes and energy dissipation. For the case of D = 0.7 mm presented in Figure 2-14(b), there is a 44 times difference in energy dissipation from the low amplitude intrawell to the snap-through responses, while the high amplitude intrawell dynamics provide an intermediate level to bridge the extremes.

This underscores the significant adaptation of energy dissipation enabled by the metastable module for fixed excitation parameters by switching amongst the various dynamic states, for example via strategic perturbations or different initial conditions. In fact, with appropriate design the module may exhibit five coexistent dynamic responses: low and high amplitude intrawell oscillations in each potential well, along with snap-through.

2.6 Conclusions

This chapter explores the unique, adaptable dynamics and energy dissipation characteristics of a constituent metastable module. Its architecture and mechanics are inspired by the metastability of a skeletal muscle cross-bridge and the properties adaptivity enabled by such an arrangement of constituent elements. An archetypal metastable module also represents a fundamental unit for the integration of negative stiffness bistable elements within an overall structural system. An experimental realization is designed, fabricated, and modeled numerically and analytically. Although the module contains a bistable constituent, the static and dynamic properties of the metastable module are significantly distinct when compared to the properties of an individual bistable element. The prescribed amplitude and frequency of harmonic global end displacement excitations on the metastable module are found to affect the existence or co-existence of multiple dynamic regimes that display an order of magnitude of difference in energy dissipation amongst them. Tailoring the displacement offset presents another method to modify energy dissipation characteristics, due to

asymmetric static mechanical properties that govern the realization of particular dynamic energy dissipation regimes. These characteristics may be used to develop vibration damping devices having large and adaptable energy dissipation properties for applications with diverse and demanding performance needs.

Chapter 3. Strain energy capture and release in multistable systems inspired by cross-bridge and sarcomere assembly

3.1 Introduction

The mechanics of skeletal muscle exhibit several noteworthy characteristics, including the ability to effectively store, convert, and release energy [11,14], providing great inspiration for the development of advanced engineered structural/material systems with similar behaviors. Models of the power stroke mechanics of skeletal muscle's cross-bridges often incorporate a bistable constituent whose two energy minima denote the pre- and post- power stroke configurations [12,54], as presented in Figure 3-1. The pre-power stroke state (also referred to as the *long* or *unfolded* configuration) has higher potential energy than the post-power stroke state (*short* or *folded* configuration), which means that the energy landscape of the bistable power stroke element is asymmetric [94].

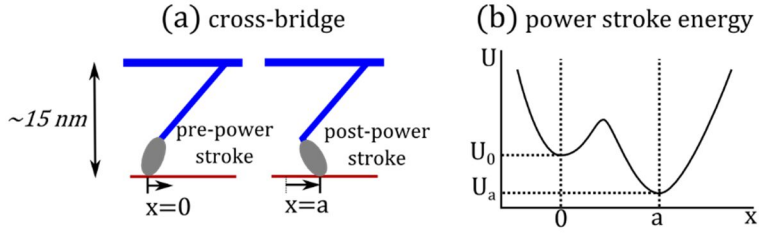

Figure 3-1. Cross-bridges (a) are responsible for the fundamental force generating process in muscle. While the cross-bridge heads are bound to actin, they undergo a power stroke, generating forces which contribute to macroscopic muscle contractions. (b) Mechanical models of cross-bridge power stroke motions incorporate elements with asymmetrically bistable potential energy landscape, reflecting a bias towards the post-power stroke state.

Recent research suggests that a significant proportion of the inertial energy from external inertial loads such as a periodically moved appendage is stored as strain energy in the cross-bridge constituent [38]. This stored energy may be later used to reduce the energetic cost of cyclic motion or to enable explosive movement [8,9]. Certain external loads have also been shown to cause power stroke reversals, allowing the cross-bridge to move back and forth repeatedly along the power stroke's energy landscape without unbinding the myosin head from the actin binding site [77].

Models of these and other mechanics at the micro- and nano-scale commonly integrate constituents with non-convex energy landscapes to capture empirically-observed conformational changes [13,26,27,42,54], and offer inspiration for the development of engineered structural/material systems that exhibit a similar ability to capture, store, and release energy. In fact, the exploitation of mechanical instabilities by incorporating bistable elements has been widely studied [95,96], demonstrating significant damping [83,97], energy dissipation [82,98], and shock absorption [99] as outcomes to the strategic exploitation. These behaviors arise primarily as a result of a *snap-through* phenomenon between stable equilibrium states of the structure's bistable constituents.

3.1.1 Asymmetric bistability and energy capture

A common physical realization of a bistable element takes the form of a clamped, post-buckled beam as depicted in Figure 3-2. The beam exhibits two stable configurations where the displacements of the beam's midpoints are $x = x_a$ and $x = x_b$, as shown in Figure 3-2(a) and (c), respectively. An unstable equilibrium is observed at the neutral position for $x = 0$, as shown in Figure 3-2(b). If the post-buckled beam is straight in its unstressed state, the reaction force as the beam midpoint is vertically displaced follows a curve similar to Figure 3-3(a), with stable equilibria observed where the curve crosses the zero axis with positive stiffness or positive slope, and an unstable equilibrium where it crosses the zero axis with negative slope. The corresponding strain energy landscape is shown in Figure 3-3(b), where the two local potential minima at the same energy

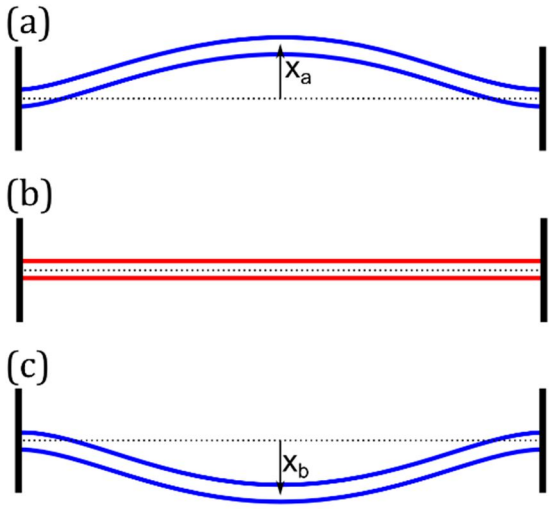

Figure 3-2. Axially compressed beam shown in three equilibrium configurations: (a) curved upward with vertical displacement of the beam midpoint $x = x_a$, (b) no vertical displacement or $x = 0$, and (c) curved downward with vertical displacement $x = x_b$. Configurations (a) and (c) are stable, while (b) is unstable.

level denote the two stable equilibria of this *symmetrically bistable* element. A beam with a natural curvature which is then clamped in its post-buckled state will be biased towards one of its two stable configurations [100], exhibiting *asymmetric bistability* and demonstrating reaction force and energy profiles represented by Figure 3-4. The two local energy minima are at different levels, and a transition from the low-energy configuration $x = x_a$ to the high energy configuration $x = x_2$ results in the capture of recoverable strain energy of the amount $\Delta U = U_1 - U_2$.

There are several examples of structural/material systems that exhibit differences in elastic potential energy between stable equilibrium configurations under tensile [101,102] and compressive [103,104] loading. These architected structures and materials exhibit larger strains before failure than the corresponding monolithic bulk material properties would permit, offering great potential for energy absorption and damage mitigation. While the energy trapping capabilities of such systems have been reported [101,103], no connection has yet been made between the asymmetries inherent to the strain energy landscapes of these structures, though the mechanics described in Figure 3-4 suggest that the asymmetric bistability inherent to these architectures may be the underlying reason

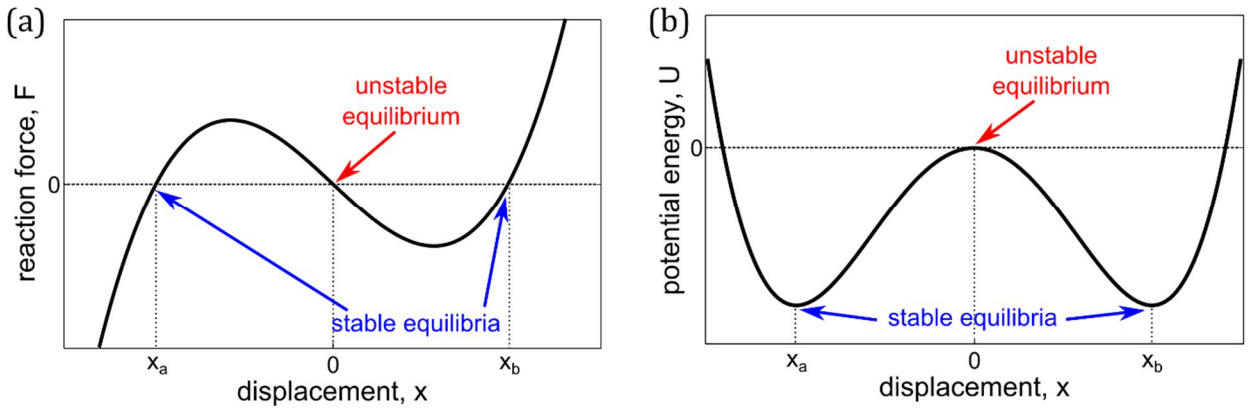

Figure 3-3. (a) Vertical reaction force at the beam midpoint in Figure 3-2, and (b) potential strain energy as displacement x is varied of a symmetric bistable constrained curved beam. Equal amounts of strain energy are stored at the two stable equilibria.

for such intriguing properties. In the context of skeletal muscle, asymmetrically bistable elements are employed to explain not only the behaviors of individual cross-bridges and sarcomeres, but also those of the protein titin, which behaves as a shock or impact absorber in sarcomeres and may also be represented mechanically as a series chain of bistable constituents [42,105]. Furthermore, though there have been efforts to understand the impact or shock isolation behaviors of structures incorporating such bistable or negative-stiffness constituents [45,82,99], these investigations do not attempt to explain the strain energy capture that may result from the observed state transitions or snap-through events.

Based on the discussions above, the objectives of the remainder of this chapter are to study the influence of asymmetry on the potential energy landscapes of structures composed of bistable constituents, to exploit transitions between stable states to demonstrate strain energy capture under quasi-static and dynamic loads, and to understand the influences of structural parameters on system dynamics and energy capture. Insights into these behaviors would enable the development of structural/material systems that reflect skeletal muscle's robustness and its remarkable ability to store, convert, and release energy. In the following subsections, experimental prototypes of single bistable elements with varying asymmetry are studied for their potential energy landscapes. A

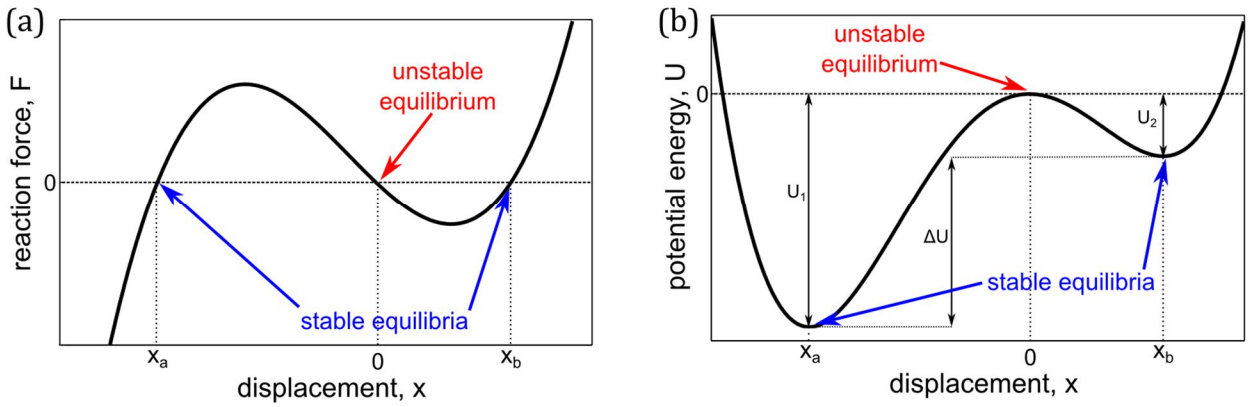

Figure 3-4. (a) Vertical reaction force at the beam midpoint in Figure 3-2, and (b) potential strain energy as displacement x is varied of an asymmetrically bistable constrained curved beam. Different amounts of strain energy are stored at the two stable equilibria. Transition from x_1 to x_2 requires a quantity of energy U_1 to be supplied to the system, and results in net strain energy storage of $\Delta U = U_1 - U_2$.

system identification is developed from experimentally-obtained force-displacement profiles, facilitating analysis and numerical investigations of the behavior of a single asymmetrically bistable element under dynamic loads. Energy landscapes of structures composed of multiple elements arranged in series are then studied, and dynamic analyses are conducted on their energy trapping capabilities. The influences of asymmetry, damping, excitation level, and thermal noise on energy trapping behaviors are analyzed and discussed. Then, an alternative parametrization of asymmetry is presented in order to facilitate an investigation of the release of this stored energy for actuation and deployment. Various quasi-static deployment pathways are considered, and this process is then studied with explicit consideration of system dynamics. An experimental demonstration is presented, followed by concluding remarks.

3.2 Structures composed of asymmetrically bistable constituents

3.2.1 Force and energy landscapes in a bistable module

To facilitate investigations into the influence of asymmetry on the mechanics and energy landscapes of bistable elements, modules with varying geometries are designed and fabricated with polyamide PA 2200 nylon using selective laser sintering (SLS). A connected, double curved-beam design minimizes the likelihood that the element will buckle or snap-through in its second mode [99,100]. This helps to ensure predictable and repeatable buckling behaviors. Figure 3-5(a) presents a schematic of a module in its unstressed state. The beam's curvature is defined as the ratio between the half-arch's height and its length, and its T-shaped member facilitates modular assembly. Figure 3-5(b) shows a prototype module in its post-buckled state under axial confinement of 39.5 mm in the lower-energy stable configuration.

Quasi-static tests are performed using an Instron 5950 universal testing machine to obtain force-displacement relationships, and representative plots for three modules of different unstressed beam curvatures are shown in Figure 3-6. The modules with the greater unstressed curvature exhibit larger positive reaction forces under compression but smaller negative reaction force, meaning an increase in unstressed beam curvatures leads to greater asymmetry in the force-displacement

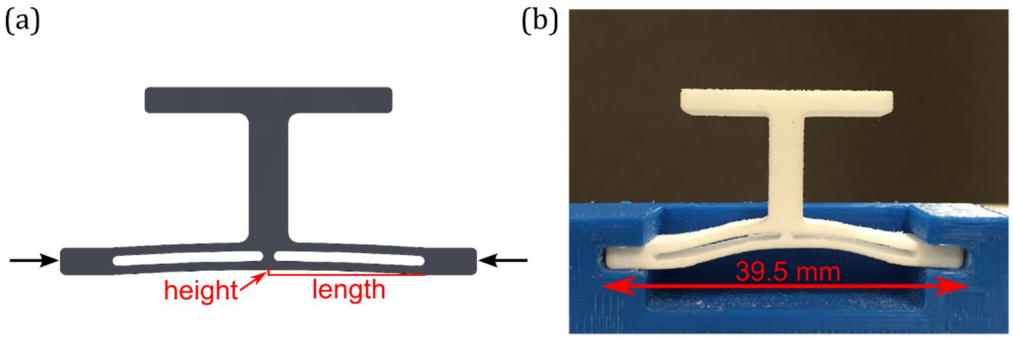

Figure 3-5. (a) Schematic of a single module composed of a connected, double curved arch with a stiff, T-shaped member to facilitate modular assembly. The unstressed beam curvature is calculated as height/length, and axial compression and constraint of double-curved beams enables bistability. (b) Experimental prototype fabricated with a beam length of 15 mm using selective laser sintering (SLS) of polyamide PA 2200 nylon shown in its post-buckled, axially compressed state. The prototype's total initial width is 40 mm, but it is compressed and confined to a width of 39.5 mm by the rigid base.

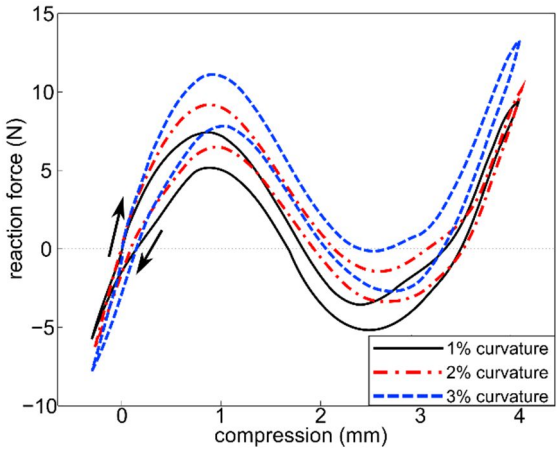

Figure 3-6. Force-displacement profiles of individual asymmetrically bistable modules obtained from uniaxial compression tests at a rate of 0.05 $\frac{\mathbf{mm}}{\mathbf{s}}$. As natural beam curvature is increased, the force-displacement characteristic grows more asymmetric with respect to the zero axis.

profile. The most asymmetric module requires a relatively large compressive force to snap to the second stable configuration, while only needing a small tensile force in order to snap back to the initial state.

Experimentally-derived strain potential energy curves, shown by the solid lines in Figure 3-7, are generated by integrating the reaction force curves with respect to displacement during the compressive portion of the quasi-static load tests. As the beam curvature is increased, the difference between the two local minima of strain energy grows larger and the energy landscape becomes increasingly asymmetric. To facilitate further numerical and analytical study of these asymmetrically bistable modules, it is assumed that the observed reaction force F_R of the modules may be approximated by a cubic nonlinearity, namely

$$F_R = k_1 x + k_2 x^2 + k_3 x^3 \tag{3-1}$$

where x represents the displacement of the midpoint of the double curved beams from the unstable equilibrium position, and k_1, k_2, and k_3 are the linear, quadratic, and cubic stiffness parameters, respectively. The potential strain energy U due to elastic deformation may be obtained by integrating the restoring force with respect to x.

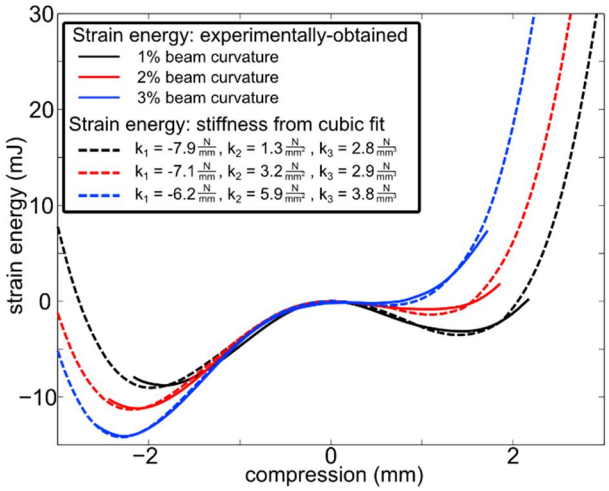

Figure 3-7. Strain energy profiles of three prototypes with varying unstressed beam curvature obtained from quasi-static compression tests (solid lines), demonstrating greater asymmetry of the double well potential energy landscape as beam curvature is increased. Dashed lines illustrate strain energy calculated from Eq. (3-2), where the nonlinear stiffness coefficients are obtained from a least-squares regression of cubic nonlinear stiffness parameters to experimental data.

$$U = \frac{1}{2}k_1x^2 + \frac{1}{3}k_2x^3 + \frac{1}{4}k_3x^4 + C \tag{3-2}$$

where C is the integration constant. For consistency, U is prescribed to be zero at the unstable equilibrium $x = 0$, which corresponds to $C = 0$. The dashed curves in Figure 3-7 depict the strain energies using Eq. (3-2) where the stiffness terms k_1, k_2, and k_3 are obtained from a polynomial fit to the experimental data, and the approximations reasonably reflect the strain energy curves of the evaluated modules. Furthermore, the quadratic stiffness k_2 demonstrates the greatest variation between modules of different beam curvature, while k_1 and k_3 are relatively similar for all three tested specimens, which suggests that variations in the asymmetry of the module's strain energy landscapes could be modeled by tailoring k_2. This is confirmed by an examination of the strain energy expression in Eq. (3-2), where the quadratic stiffness $k_2$contributes the only odd term and hence dictates the level of asymmetry. The cubic nonlinear stiffness approximation enables a systematic analytical and numerical dynamics study of the influence of various system and excitation parameters on strain energy landscapes and energy trapping performance.

3.2.2 Force and energy landscape of a multi-module system

Mechanical models of skeletal muscle often incorporate serially-connected bistable elements in representations of sarcomere chains that form muscle myofibrils [25,26], and the protein titin [45,105]. Assembly of asymmetrically bistable elements into these greater structures leads to more complex force-displacement and strain energy landscapes, enabling large macroscopic length changes, shock absorption, and energy dissipation [43,45,103]. This configuration may also be leveraged to demonstrate the capture and storage of elastic potential energy in the system's many stable configurations. For a structure composed of n serially connected bistable modules as depicted in Figure 3-8, and whose reaction forces are governed by Eq. (3-1), the total strain energy stored in the system is:

$$U_{tot} = \frac{1}{2}k_{1,1}{x_1}^2 + \frac{1}{3}k_{2,1}{x_1}^3 + \frac{1}{4}k_{3,1}{x_1}^4 + \sum_{j=2}^{n}\left(\frac{1}{2}k_{1,j}\left(x_j - x_{j-1}\right)^2 + \frac{1}{3}\left(x_j - x_{j-1}\right)^3 + \frac{1}{4}\left(x_j - x_{j-1}\right)^4\right) \tag{3-3}$$

where x_j is the displacement and $k_{1,j}, k_{2,j}$, and $k_{3,j}$ are the linear, quadratic, and cubic stiffness coefficients, respectively, of the j^{th} module.

This arrangement of elements, in which *interactions* between adjacent elements are governed by a bistable potential [45,106], is notably distinct from systems where elements are in local, *on-site*, bistable potentials and adjacent elements are coupled by a linear or monostable stiffnesses [107,108]. A structure

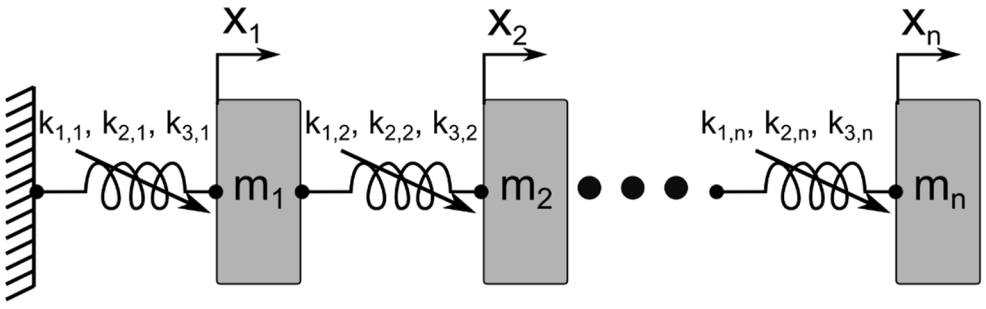

Figure 3-8. Schematic of a structure composed of *n* modules in series with bistability modeled using a cubic nonlinear stiffness.

with bistable interactions can exhibit large length and shape change across its global energy landscape as individual bistable elements transition from one stable position to the other.

To demonstrate the mechanics of systems composed of serially-configured modules, Figure 3-9(a) Figure 3-9(b) present experimentally-obtained reaction force profiles of a structure composed of two and four modules, respectively, with 2% beam curvature. Positive slope or stiffness denotes the existence of stable configurations, and negative slopes correspond to regions of transition between stable states. The four-module structure demonstrates a greater number of stable configurations and much greater hysteresis over the compression and extension cycle. The increased hysteresis is due to increased free-play in the structure, as well as the increased likelihood of divergence between loading and unloading paths as the number of elements in a bistable chain is increased [42,45]. For a single bistable element, the loading and unloading paths are theoretically identical, since there is only one stable configuration for a prescribed displacement. In a structure composed of $n = 2$ *identical* bistable elements with cubic nonlinearity, there may be multiple possible configurations for a range of global displacements, but they are at identical strain energy levels and thus do not demonstrate hysteresis under idealized conditions [106]. Such a structure would exhibit smoothly varying strain energy under loading and unloading. However, for $n > 2$ or for $n =$

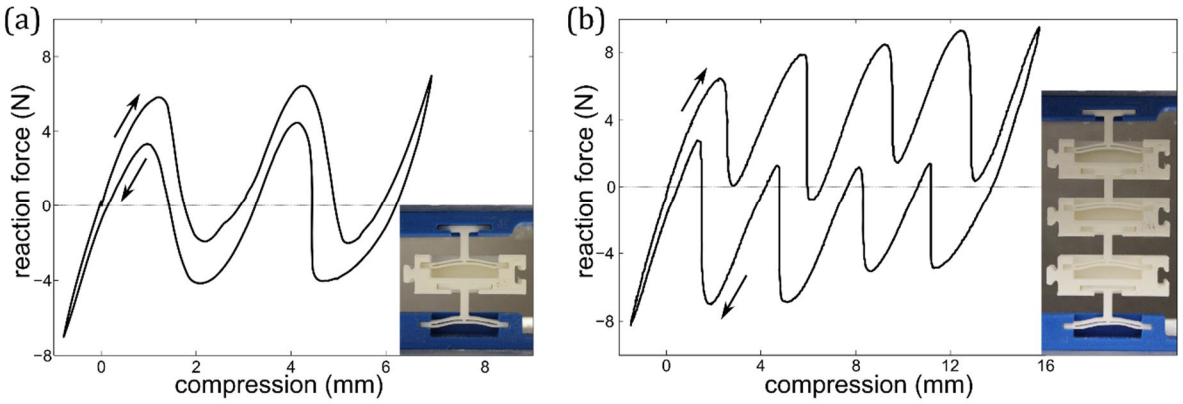

Figure 3-9. Observed reaction force of a (a) two-module structure and (b) four-module structure under uniaxial compression tests at a rate of 0.05 $\frac{\mathbf{mm}}{\mathbf{s}}$.

2 *different* modules, these coexistent configurations may be at different energy levels, and as the structure is globally extended or compressed, it does not follow the minimum-energy *Maxwell path* [42]. Instead, the large hysteresis observed in Figure 3-9(b) is due to discrete state transitions that result in a decrease of potential energy when the structure's current configuration becomes unstable and the system snaps to a different stable configuration at a lower energy level, releasing stored elastic energy in the process [45,97,109].

Since the modules considered in this chapter are nominally identical, the order in which the elements snap through is governed by manufacturing defects [103,104]. Under compressive loading, the module with the lowest maximum stress in the long or extended state will undergo a transition first. This explains the increasing local maxima of reaction force of the four-module system under the compression portion of the path in Figure 3-9(b). The same phenomenon under extension explains the decreasing local minima of reaction force along the extension portion. If desired, the deformation paths can be designed to be deterministic by varying the geometric parameters of each module that govern the maximum of minimum reaction force before snap-through [110,111].

Due to discrete state transitions that release elastic potential energy, direct integration of the experimentally-obtained force displacement profiles of structures composed of multiple elements does not in general yield their strain energy landscapes. To gain insight into the energy landscapes of two- and four-module structures, Figure 3-10 presents the strain energy as computed from Eq. (3-3) where each module's nonlinear stiffness coefficients are obtained from the system identification results shown in Figure 3-7. For the two-module case in Figure 3-10(a), random variation corresponding to a standard deviation of 5% from the nominal values is applied, accounting for manufacturing variability between the nominally identical modules and to facilitate clearer presentation of the ranges under which the different stable configurations may be observed. These configurations are denoted by different line styles and correspond to the presented figure insets.

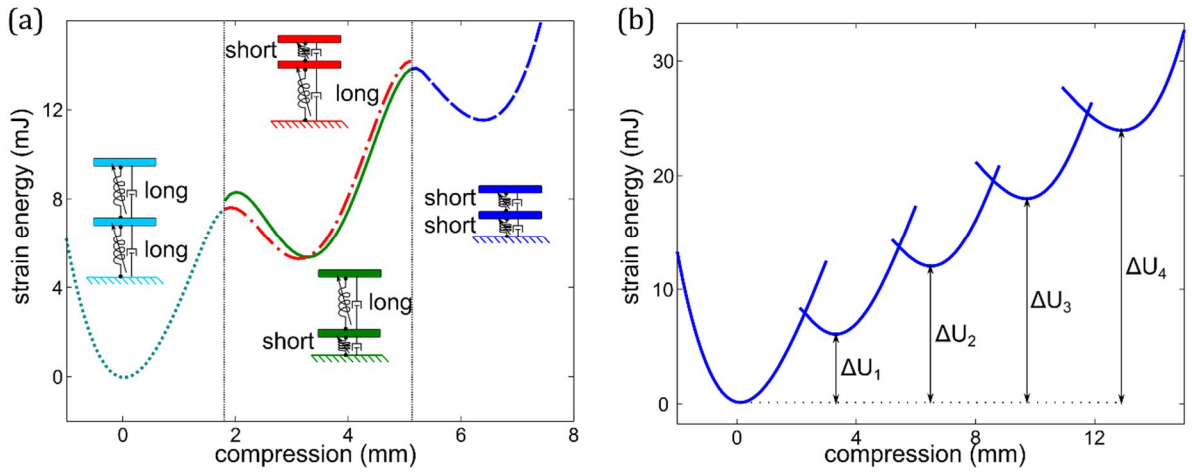

Figure 3-10. Strain energy landscape of a (a) two-module and (b) four-module structure calculated using a cubic stiffness approximation to experimentally-observed reaction force of a module with 2% beam curvature. A small difference between the stiffness terms of the two modules is provided in (a) in order to clearly illustrate the existence of multiple configurations. The four-module structure demonstrates overlapping potential wells, a feature found in chains of *n>2* bistable elements [45]. Due to the individual modules' asymmetry, increasing amounts of strain energy, ΔU_1 to ΔU_4, are stored at the stable equilibria – or local energy minima – as the structure is compressed.

The assembly of multiple modules in series gives rise to a *metastability range* [76], where multiple reaction forces and strain energies may be observed for a range of end displacements x_2 due to the *coexistence* of multiple stable configurations, although only one configuration may be physically realized at a given time. If the modules were identical, the two global configurations in which one module in the short state and the other is in the long state would exhibit overlapping energy levels [106]. However, the modules are slightly different, and discontinuities are observed between the cyan dotted and green solid curves, and between the red dash-dotted and blue dashed curves of Figure 3-10(a). Under an external axial load, the structure will only exhibit state transitions that are either continuous in potential energy if the current topology represents a local energy minimum with respect to the internal degrees of freedom, or that result in a discrete reduction of stored strain energy [109,111]. For the four-module case presented in Figure 3-10(b), no random variation is applied to the modules' stiffness parameters and all modules are assumed to be identical. The local minima of potential energy, which denote the stable configurations in the absence of external forces, are at different quantities depending on the number of modules in the long (low-energy) and short (high-

energy) configurations. Hence, a transition from the lowest energy global configuration to higher-energy configurations will result in incremental amounts of captured and stored elastic energy ΔU_1 to ΔU_4, depending on the number of long-to-short state transitions that occur.

3.3 Dynamic response of asymmetrically multistable systems

3.3.1 Dynamics of an asymmetrically bistable oscillator

The quasi-static analysis in the prior subsection demonstrates that modular assembly of asymmetrically bistable constituents can lead to structures exhibiting complex, multi-well energy landscapes and whose stable configurations exhibit different quantities of stored elastic potential energy. Due to the modules' geometry, transitions from long to short configurations result in the capture and storage of recoverable strain energy. On the other hand, for structures under dynamic loads, the total system energies do not smoothly follow potential energy landscapes. Since the captured strain energy ΔU depends on the initial and final configurations of the system, transient dynamics play an important role in the structure's ability to capture energy in consequence to excitations. The experimental prototypes presented in the prior subsection, while not well-suited to dynamic tests due to their large damping, viscoelasticity, and low toughness, motivate comprehensive analytical and numerical investigations of these dynamics. Figure 3-11 presents a

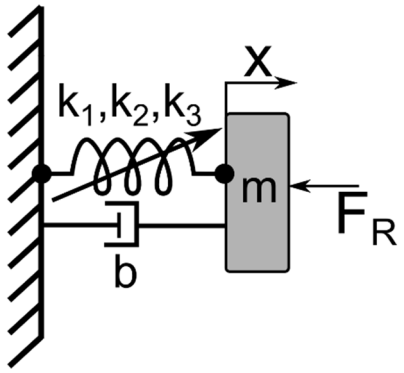

Figure 3-11. Schematic of a Duffing oscillator. k_1, k_2, and k_3 are the linear, quadratic and cubic stiffness coefficients of the nonlinear spring. The oscillator is bistable for $k_1 < 0$ and asymmetric for $k_2 \neq 0$.

schematic of a one degree-of-freedom system based on the experimentally-derived single-module mechanics shown in Figure 3-6 and Figure 3-7. The bistable nonlinear stiffness takes the cubic form of Eq. (3-1), while inertial influences are captured by the mass m, and linear viscous damping is assumed with coefficient b. The governing equation is thus:

$$m\ddot{x} + b\dot{x} + k_1 x + k_2 x^2 + k_3 x^3 = 0 \tag{3-4}$$

Eq. (3-4) describes the dynamics of a Duffing oscillator [89], and under the specific conditions $k_1 < 0$, $k_2 \neq 0$, and $k_3 > 0$, it describes an asymmetric bistable Duffing oscillator. For the case of a single asymmetric Duffing oscillator starting in its lower-energy configuration, energy trapping due to an impulsive excitation may be quantified by comparing the difference in potential energy between its initial and final states with the initial kinetic energy of the impulsive excitation. Hence, if the initial and final configurations are identical, all of the initial kinetic energy is dissipated and no energy is trapped. If, however, the system settles in its higher-potential energy well, a portion of the initial kinetic energy is now captured and stored.

Predicting the system's final configuration following impulsive excitation necessitates solving for its transient dynamics. Solution methods that assume the transient dynamics of Duffing-type oscillators can be described using trigonometric functions generally lead to degraded accuracy for large nonlinearities [112]. Jacobian elliptic functions have been proposed as generating solutions for the Duffing equation, with considerable success for undamped, bistable Duffing oscillators [89,113]. Recently, Zhang et al. [114] presented a solution method for the damped snap-through and intrawell vibrations of a symmetric bistable Duffing oscillator. However, this approach cannot be directly applied to the case of an asymmetric Duffing oscillator due to the assumed symmetric form of the Jacobian elliptic function $cn(u_c, k_c)$, so the method is adapted and modified. First, Eq. (3-4) is normalized by mass and rewritten as

$$\ddot{x} + \eta\dot{x} + \alpha x + \beta x^2 + \gamma x^3 = 0 \tag{3-5}$$

where $\alpha = \frac{k_1}{m}, \beta = \frac{k_2}{m}, \gamma = \frac{k_3}{m}$, and $\eta = \frac{b}{m}$. In order to eliminate the quadratic stiffness β causing the asymmetry, the system is approximated by two different, symmetric bistable Duffing oscillators, each approximating the behavior of the original system in one of the two potential wells.

$$\ddot{x} + \eta\dot{x} + \alpha_1 x + \gamma_1 x^3 = 0;\ x \leq 0 \tag{3-6a}$$

$$\ddot{x} + \eta\dot{x} + \alpha_2 x + \gamma_2 x^3 = 0;\ x > 0 \tag{3-6b}$$

The stiffnesses $\alpha_1, \gamma_1, \alpha_2$, and γ_2 are obtained from a least-squares regression of the asymmetrically bistable spring reaction force in Eq. (3-5). The validity of this approach for describing the force-displacement and potential energy profiles of the asymmetrically bistable spring is verified by Figure 3-12 for $\alpha = -7.1$, $\beta = -3.2$, and $\gamma = 2.9$. The approximated stiffnesses are $\alpha_1 = -4.9, \gamma_1 = 4.0$ for $x < 0$, and $\alpha_2 = -10.4, \gamma_2 = 2.2$ for $x > 0$. Further details on the solution approach for the system's transient dynamics are presented in Appendix B.

Figure 3-13 illustrates the procedure's accuracy in predicting the transient intrawell vibrations of a damped asymmetrically bistable Duffing oscillator under two different initial conditions: (a) $x_0 = 2.2$ mm, $\dot{x}_0 = -0.45\,\frac{\text{m}}{\text{s}}$ and (b) $x_0 = 2.2$ mm, $\dot{x}_0 = -0.80\,\frac{\text{m}}{\text{s}}$. The stiffness terms k_1, k_2, and k_3 are -7.1

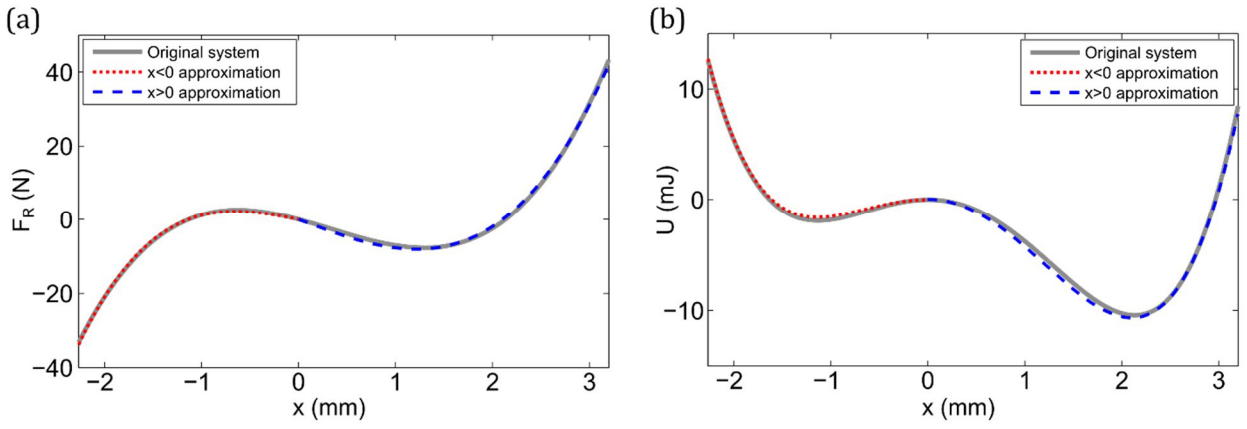

Figure 3-12. (a) Reaction force and (b) strain energy of an asymmetrically bistable Duffing oscillator. Solid lines denote the mechanics of the original asymmetric system described by Eq. (3-5), while the dotted and dashed lines denote the mechanics of the approximations of Eqs. (3-6a) and (3-6b), respectively.

$\frac{\text{N}}{\text{mm}}$, -3.2 $\frac{\text{N}}{\text{mm}^2}$, and 2.9 $\frac{\text{N}}{\text{mm}^3}$, respectively, which reflect the stiffness parameters obtained from the quasi-static tests presented in Figure 3-6. Mass m and damping coefficient b are prescribed such that the linearized damping ratio and undamped natural frequency at $x = x_0$ are $\zeta = 0.4$ and $\omega_n = 119\ \frac{rad}{s}$, and are selected to reflect an underdamped oscillator capable of exhibiting the desired strain energy capturing behaviors under dynamic loads. The oscillator is initially at rest in its lower-energy stable configuration. Dotted lines show the trajectories as computed numerically using the original system description of Eq. (3-5), and dashed lines show the trajectory as computed numerically from the approximate systems of Eqs. (3-6a) and (3-6b) in the two potential wells. Solid lines present analytically-predicted trajectories until the final snap-through event.

Under the initial conditions of the trajectories plotted in Figure 3-13(a), the system is observed to undergo one snap-through event and settle in its higher-energy stable configuration, trapping a portion of the initial kinetic energy $T_0 = \frac{1}{2}m\dot{x}_0^2$ as recoverable strain energy. The fraction R of energy thus captured is computed as:

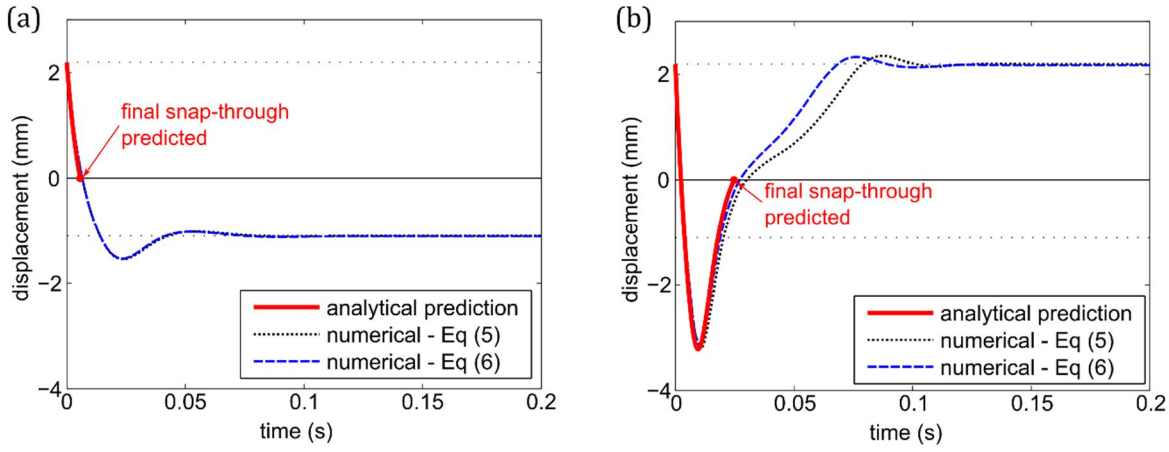

Figure 3-13. Analytically-predicted snap-through trajectories (solid), and numerically integrated trajectories using the asymmetric system of Eq. (3-5) and approximation of Eq. (3-6) in consequence to initial conditions (a) $x_0 = 2.2$ mm, $\dot{x}_0 = -0.45\frac{\text{m}}{\text{s}}$ and (b) $x_0 = 2.2$ mm, $\dot{x}_0 = -0.80\frac{\text{m}}{\text{s}}$. In (a), the two numerically-integrated trajectories overlap almost completely. Thin, dotted horizontal lines denote the two stable equilibria. The analytical approach is demonstrated to accurately predict the final occurrence of snap-through, and hence the module's final configuration.

$$R = \frac{\Delta U}{T_0} = \frac{U_2 - U_1}{T_0} \tag{3-7}$$

where U_1 and U_2 are the strain potential energy at the initial and final configurations, respectively. In Figure 3-13(b) two snap-through events are observed, and the system settles in its low energy initial configuration resulting in no energy trapped ($R = 0$). The results of Figure 3-13 demonstrate the ability of the presented analytical approach to predict the snap-through trajectories and final configuration of a damped asymmetrically bistable oscillator under impulsive excitation, and hence to predict the fraction of initial kinetic energy that is captured as recoverable strain energy.

3.3.2 Dynamics of a multi-module structure

The assembly of multiple elements in series greatly enhances opportunities for strain energy capture by leveraging state transitions between configurations at different energy levels. As illustrated in Figure 3-10(b) for a structure composed of four serially connected modules, stable configurations exhibit increased stored energy as the structure is compressed and modules transition to the higher-energy short configurations. Assuming linear viscous damping and determining the reaction forces due to deflection in the cubic nonlinear springs connecting adjacent masses, the following equation of motion is obtained for mass m_j within a series configuration of n modules shown in Figure 3-14.

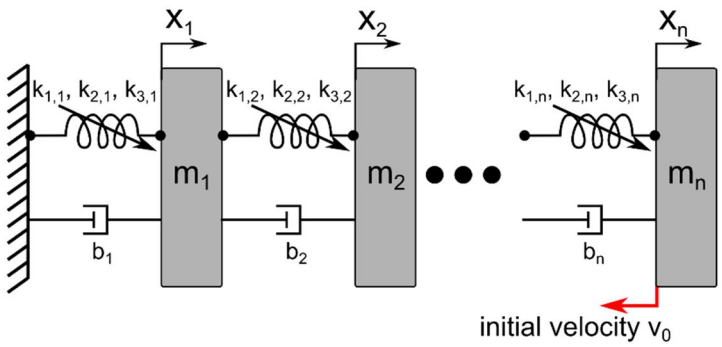

Figure 3-14. Schematic of a structure composed of n modules arranged in series. Initial velocity is prescribed to the end mass m_n in the indicated direction during dynamic analyses of energy trapping, simulating an impulsive excitation.

$$m_j\ddot{x}_j + b_j(\dot{x}_j - \dot{x}_{j-1}) + b_{j+1}(\dot{x}_k - \dot{x}_{j+1}) + k_{1,j}(x_j - x_{j-1}) + k_{1,j+1}(x_j - x_{j+1}) + k_{2,j}(x_j - x_{j-1})^2 +$$

$$k_{2,j+1}(x_j - x_{j+1})^2 + k_{3,j}(x_j - x_{j-1})^3 + k_{3,j+1}(x_j - x_{j+1})^3 = 0 \quad (3\text{-}8)$$

The transient response is strongly influenced by the initial velocity and kinetic energy, as illustrated by the results presented in Figure 3-15 for a four-module structure under different input energy levels. The stiffnesses $k_{1,j}, k_{2,j}$, and $k_{3,j}$ are -7.1 $\frac{\text{N}}{\text{mm}}$, -3.2 $\frac{\text{N}}{\text{mm}^2}$, and 2.9 $\frac{\text{N}}{\text{mm}^3}$ for all modules. Each module has mass m_j and damping coefficient b selected such that the linearized natural frequency and damping ratio at each module's low-energy stable state are $\omega_{n_i} = 119\frac{rad}{s}$ and $\zeta_j = 0.4$, respectively. The initial velocity of the end mass is prescribed as v_0, and all other masses are stationary in the low energy state (long configuration). The thin, dotted horizontal lines indicate the five displacements x_4 of the end mass for stable configurations of the four-module structure.

For an initial velocity $v_0 = 0.3\frac{\text{m}}{\text{s}}$, shown by the solid line, the initial energy $T_0 = \frac{1}{2}m_4v_0^2$ is insufficient to cause any of the four modules to snap through, and the structure remains in its initial

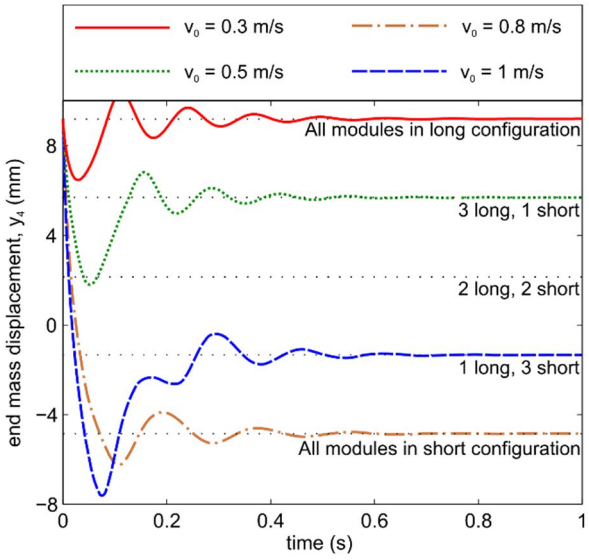

Figure 3-15. Displacements x_4 of a four-module structure's end mass due to impulsive excitations causing initial velocities v_0 when all modules are initially in their low-energy long states. Thin dotted lines indicate the five possible displacements under stable equilibrium conditions. The final configuration is strongly dependent on excitation level.

configuration. For a slightly greater initial velocity of $0.5\,\frac{\mathrm{m}}{\mathrm{s}}$, shown by the thick dotted line, one of the structure's modules snaps through to its short configuration. Since $k_{2,j} < 0$ for all j, each module's short configuration has higher potential energy than its long state and a portion of the initial kinetic energy is trapped as recoverable strain energy. An initial velocity $v_0 = 0.8\,\frac{\mathrm{m}}{\mathrm{s}}$, indicated by the dash-dot line, causes all four modules to snap to the short state, maximizing trapped strain energy. However, if the initial velocity is increased to $v_0 = 1\,\frac{\mathrm{m}}{\mathrm{s}}$, the residual kinetic energy after all modules have collapsed to their high-energy state is sufficient to force one module to escape its local potential well and snap back to the lower-energy long configuration, reducing the quantity of trapped strain energy.

3.4 Energy capture under impulsive excitation

The four initial conditions for which trajectories are plotted in Figure 3-15 result in four different final configurations and, due to the modules' asymmetric bistability, four different quantities of captured elastic potential energy ΔU. Energy trapping performance may be quantified using the ratio $R = \frac{\Delta U}{T_0}$, and by conservation of energy the total energy dissipated is $(1 - R)T_0$. While Figure 3-15 demonstrates that input energy strongly influences the structure's final configuration, a systematic investigation is required in order to uncover the effects of varying structural parameters and excitation levels on energy trapping performance.

3.4.1 Strain energy capture in a single asymmetrically bistable module

To illustrate these effects, Figure 3-16 presents contour plots showing the fraction of initial kinetic energy that is captured as recoverable strain energy in a single asymmetrically bistable module under a range of initial velocities v_0 and different levels of asymmetry. The linear and cubic stiffness parameters employed in simulation and analysis are $k_1 = -7.1\,\frac{\mathrm{N}}{\mathrm{mm}}$ and $k_3 = 2.9\,\frac{\mathrm{N}}{\mathrm{mm}^3}$.

Recalling that the asymmetry of a cubic nonlinear spring varies with k_2, the ratio $\frac{k_2}{k_3}$ is used as a measure of asymmetry. The module is initially at rest in its low-energy long configuration and prescribed a range of initial velocities v_0 in the direction of the unstable equilibrium. Dissipative effects are modeled with a linear damping coefficient selected such that the linearized damping ratio at the two stable equilibria of a symmetric module (where $k_2 = 0$) is $\zeta = 0.4$. Figure 3-16(a) presents analytically-predicted energy trapping performance using the approximation of Eq. (3-5) while Figure 3-16(b) shows results from direct numerical integration of Eq. (3-4).

No energy trapping is observed for low initial velocities since the initial energy is insufficient to induce snap-through. The modules' initial and final configurations are hence identical. A clear boundary is apparent where the initial velocity, and consequently the initial kinetic energy, becomes sufficient to cause the module to snap-through and settle in the higher-energy state following trajectories qualitatively similar to Figure 3-13(a). Very large initial velocities result in trajectories resembling Figure 3-13(b), demonstrating no energy trapping due to the module snapping back to

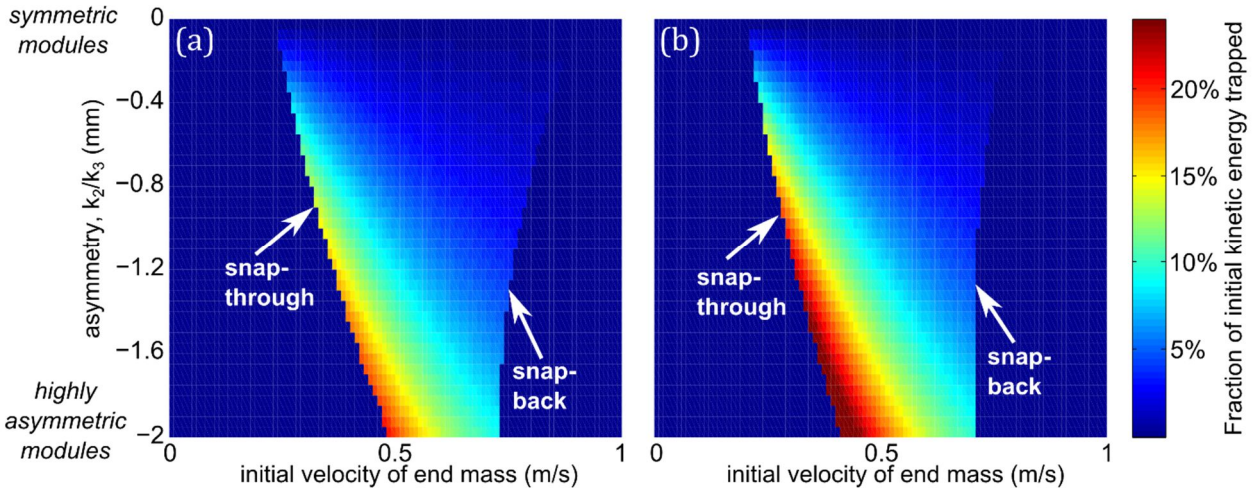

Figure 3-16. (a) Analytical prediction and (b) numerical simulation of fraction of initial kinetic energy T_0 from an impulsive excitation trapped as recoverable strain energy as level of asymmetry is varied under a range of initial velocities. Linear and cubic stiffness terms k_1 and k_3 are obtained from the cubic nonlinear approximation to the experimentally-obtained force-displacement profile shown in Figure 3-6 of the module with 2% beam curvature. The quadratic stiffness k_2 is varied along the vertical axis to tailor the asymmetry. Boundaries demarcating the onset of snap-through and snap-back are clearly visible.

its low-energy configuration. The analytical prediction of these boundaries differs slightly from the numerically-obtained results, which is reasonable given that the analytical method employs an approximation of the original system. As asymmetry is increased, a greater initial velocity is required before snap-through and energy trapping are observed. The greatest fraction of trapped energy is observed for large asymmetry, which is consistent with the explanations of Figure 3-3 and Figure 3-4, because greater asymmetry increases U_1 while decreasing U_2, resulting in a larger potential energy difference ΔU. However, large asymmetries also show a smaller range of velocities for which energy trapping is observed before the module snaps back to its low energy configuration, resulting in no strain energy capture.

3.4.2 Strain energy capture in a four-module structure

While Figure 3-9 demonstrates that a structure with asymmetrically bistable constituents will exhibit different quantities of stored energy in its stable configurations, its transient response and final configuration in consequence to dynamics loads depends strongly on input energy. To further understand these influences, Figure 3-17 presents a contour plot showing the percentage of initial kinetic energy trapped as recoverable strain energy in a four-module structure under a range of initial velocities v_0 and levels of asymmetry $\frac{k_2}{k_3}$, obtained via numerical integration of Eq. (3-8) using a fourth-order Runge-Kutta solver. Linear and cubic stiffness are nominally prescribed as $k_1 = -7.1\frac{\mathrm{N}}{\mathrm{mm}}$ and $k_3 = 2.9\frac{\mathrm{N}}{\mathrm{mm}^3}$, respectively, with a linearized damping ratio of $\zeta = 0.4$. A random variation is then applied to each module's parameters with a standard deviation of 5% of the nominal value. As the initial velocity v_0 is increased from 0, a clear color boundary is noted where the initial kinetic energy $T_0 = \frac{1}{2}mv_0^2$ is sufficiently large to cause one of the four modules to snap through to the higher-energy short configuration. Four such boundaries are visible, corresponding to each of the four layers collapsing from the long configuration to the short configuration. Consistent with the single module case shown in Figure 3-16, increasing the level of asymmetry results in a greater

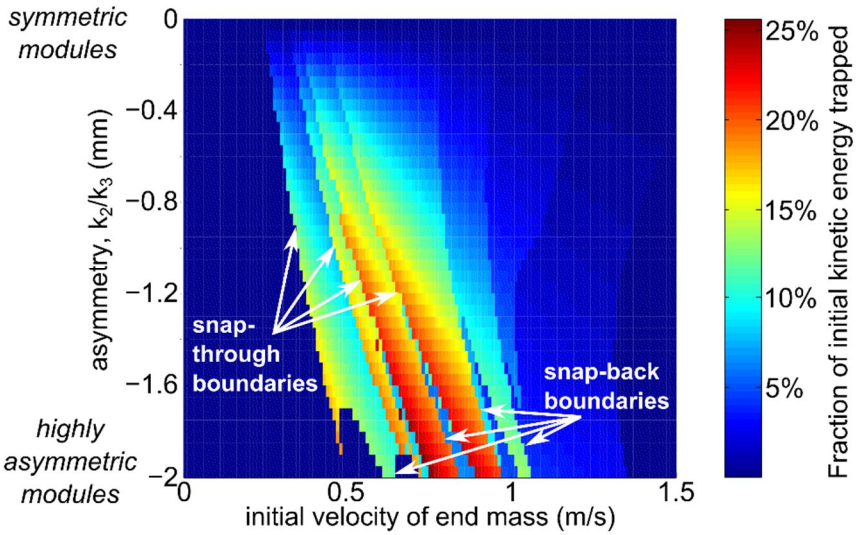

Figure 3-17. Fraction of initial kinetic energy T_0 that is trapped as recoverable elastic potential energy by the structure as the level of asymmetry and initial velocity of the end mass are varied. Linear and cubic stiffness parameters are obtained from a least-squares fit of a cubic nonlinear stiffness to the experimentally-obtained force-displacement profile of a module with 2% beam curvature. Damping coefficients are selected such that each module's linearized damping ratio is ζ = 0.4 at the low-energy configuration. The discrete boundaries of energy trapping performance indicate the occurrence of snap-through and snap-back. Greatest energy trapping performance is observed at high asymmetry levels, but this comes with an increased risk of snap-back.

minimum initial velocity being required before energy trapping is observed. In addition, highly asymmetric modules have a large difference ΔU between stable configurations, enabling a greater portion of the initial kinetic energy to be captured as recoverable strain potential energy rather than lost due to dissipation.

The snap-back phenomenon is apparent in Figure 3-17 where a sudden drop in energy trapping is observed as the initial velocity is increased, and explains the absence of energy trapping at very large initial velocities where all modules have snapped back to the long, low energy configuration. Snap-back boundaries are most pronounced for highly asymmetric modules where the energy difference between stable configurations is large, and these highly asymmetric structures exhibit only a small range of initial velocities for which peak energy trapping is observed. These results reveal that, when designing the level of asymmetry in energy trapping structures, a balance must be

considered between achieving the peak energy trapping required and minimizing the likelihood of snap-back.

3.4.3 Influence of viscous damping on energy capture

A structure's damping properties strongly influence energy trapping performance, since the conservation of energy requires that any portion of the initial kinetic energy T_0 that is not captured as strain energy must be dissipated. Furthermore, energy capture fundamentally requires a dissipation mechanism to ensure a multistable system experiencing snap-through oscillations will eventually settle in a potential well [114]. The fraction of initial kinetic captured as recoverable strain energy is $R = \Delta U/T_0$, while the ratio of captured to dissipated energy is $R/(1-R)$. Figure 3-18(a) and (b) present contour plots with the same ranges of excitation level and asymmetry, and the same color scale as shown in Figure 3-17. However, damping coefficients selected such that the modules' linearized damping ratios are now (a) $\zeta = 0.6$ and (b) $\zeta = 0.8$, respectively. Comparing the results of Figure 3-18 with those in Figure 3-17, it is observed that increased viscous damping reduces peak

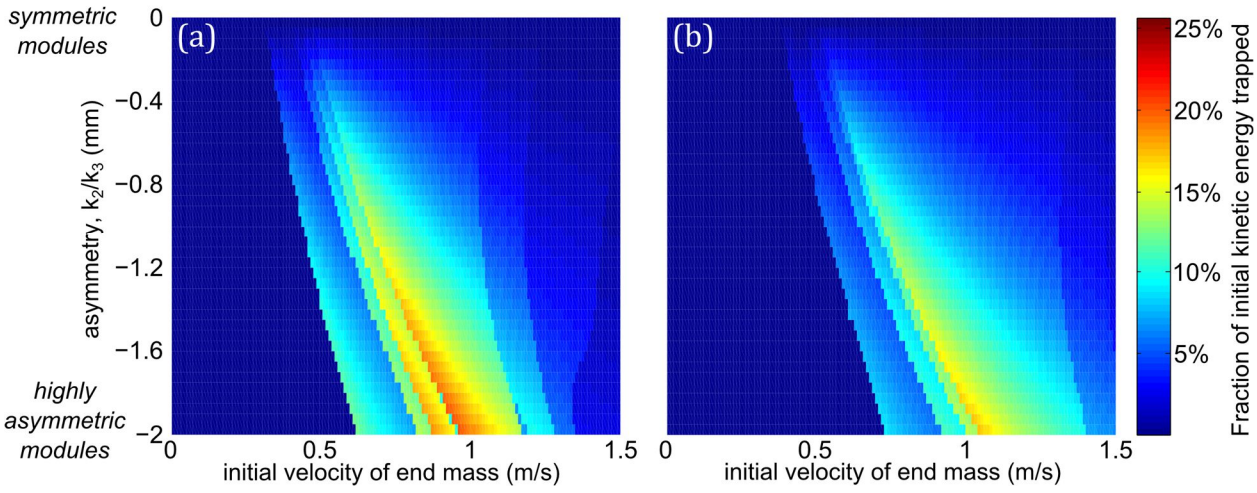

Figure 3-18. Fraction of initial kinetic energy T_0 that is trapped as recoverable elastic potential energy by the structure, as the level of asymmetry and initial velocity of the end mass are varied when damping coefficients are selected such that the linearized damping ratios are (a) ζ = 0.6 and (b) ζ = 0.8 in the low-energy configurations. Compared with the results for ζ = 0.4 in Figure 3-16, larger damping ratios generally degrade energy trapping performance, but result in a reduced risk of snap-back at higher asymmetry levels. Any initial kinetic energy that is not captured must be dissipated, so the reduced energy trapping performance at higher levels of damping corresponds to a greater proportion of dissipated energy.

energy trapping performance by dissipating a greater proportion of the initial kinetic energy. Large amplitude snap-through events dissipate large quantities of energy, and this characteristic is enhanced as damping levels are increased, reducing the likelihood of further snap-through or snap-back events. Moreover, as damping is increased, greater initial velocities and kinetic energies are required to induce snap-through events.

Hence, large dissipation is undesirable from an energy trapping perspective since the objective is to capture, rather than dissipate, the initial kinetic energy as recoverable strain energy. However, large dissipation also reduces the likelihood of snap-back as excitation level is increased. A balance is again observed between maximizing the fraction of initial kinetic energy that is trapped as recoverable strain energy, and maintaining robustness by minimizing the risk of snap-back to configurations at low strain energy levels.

3.4.4 Variation of module stiffness parameters

Prior results consider systems in which each module's stiffness parameters are nominally identical, so the critical static force required to induce snap-through is the same for all modules. To improve the robustness of energy capture performance, this section considers systems in which the linear stiffness component k_1 of the nonlinear stiffness varies across modules. For bistability, the condition $k_1 < 0$ must hold. Making k_1 more negative results in steeper negative stiffness region around the unstable equilibrium, and results in larger forces required to snap from one stable state to the other. The results of Figure 3-19 present energy capture performance where all system parameters except k_1 are the same as in Figure 3-17. In Figure 3-19(a), the four modules have $\left[k_{1,1}, k_{1,2}, k_{1,3}, k_{1,4}\right] = [1.15k_1^*, 1{,}05k_1^*, 0.95k_1^*, 0.85k_1^*]$, where k_1^* is the nominal linear stiffness employed in prior results. In Figure 3-19(b), $\left[k_{1,1}, k_{1,2}, k_{1,3}, k_{1,4}\right] = [1.30k_1^*, 1{,}10k_1^*, 0.90k_1^*, 0.70k_1^*]$. The consequence is that the element at the free end of the structure where the impulse is applied is

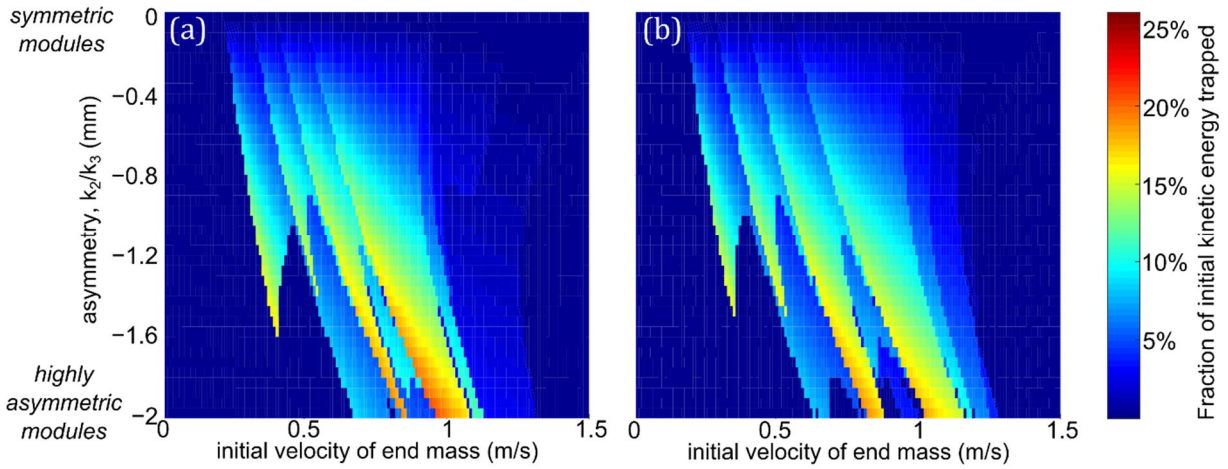

Figure 3-19. Fraction of initial kinetic energy T_0 that is trapped as recoverable elastic potential energy by the structure, as the level of asymmetry and initial velocity of the end mass are varied and there is (a) small and (b) large variation of the linear stiffness parameters k_1 across modules. Comparing these results with those of Figure 3-17, it is noted that strategic variation of k_1 can enable more predictable, sequential energy trapping with clearer separation between subsequent snap through boundaries. However, the peak energy trapping performance is reduced.

more susceptible to snap-through, while the element closest to the base is more resistant to a transition to the high-energy state.

Variation of geometric parameters of multistable structure have been shown to affect the stiffness parameters that may increase or decrease susceptibility to snap-through, allowing for deterministic and predictable snap-through or buckling sequences under quasi-static loads [110,111], but this feature may also be exploited under dynamic loads, as considered here. Comparison of Figure 3-19 with the results of Figure 3-17 suggests that strategic variation of the negative linear stiffness parameter reduces the initial velocity, and consequently the initial energy, required to activate energy capture. Additionally, there is more uniform separation between the four main snap-through boundaries as the variation is increased, as well as a greater range of initial velocities for which energy capture is observed, particularly at low levels of asymmetry. While the peak energy trapping performance is reduced when compared with Figure 3-17, deliberate variation of the negative stiffness parameter is shown to yield more predictable, sequential energy capture behavior. Such performance may be desirable for protective structures, and devices, where a predictable and

repeatable snap-through response to dissipate and capture energy can help ensure the system safety and integrity.

3.4.5 Influence of noise on energy trapping

Thermal noise strongly influences the mechanics of muscle sarcomeres and cross-bridges. In fact, macroscopic muscle length change and force generation is due to the combination of a control signal broadcast by the central nervous system and stochastic behaviors at the sarcomere level [74]. Local thermal noise acts as an additive white noise component to a nerve impulse, and collective behaviors arise due to the fact that a single motor neuron controls approximately a billion individual sarcomeres, averaging out individual responses [4]. The nerve impulse influences the probability of sarcomere state transitions, and feedback from muscle spindles leads to the modulation of the control signal in order to enable fine, continuous macroscopic length change and force generation.

However, thermal noise can inhibit the energy storage by facilitating potential well escape [55], since elements may be more likely to escape shallow potential wells at high energy levels into lower-energy configurations. To understand these influences, and to guide the development of energy trapping devices for applications such as actuators and energy absorbing devices used on micro and nano length scales, simulations are performed using the stochastic differential equation (SDE) Toolbox [115]. A four-module structure initially at the lowest-energy stable configuration with varying levels of asymmetry and a range of prescribed initial velocities, is subject to thermal noise modeled as a zero-mean random excitation on each module with a standard deviation $\sigma = 3\frac{\mathrm{mm}}{\mathrm{s}^2}$. Since the susceptibility of bistable systems to snap-through is strongly influenced by the presence of random excitations [55,116,117], and given the modules' parameters developed in Section 3.2, this level of noise is shown to be sufficient to prevent highly asymmetric modules from settling in their high energy states.

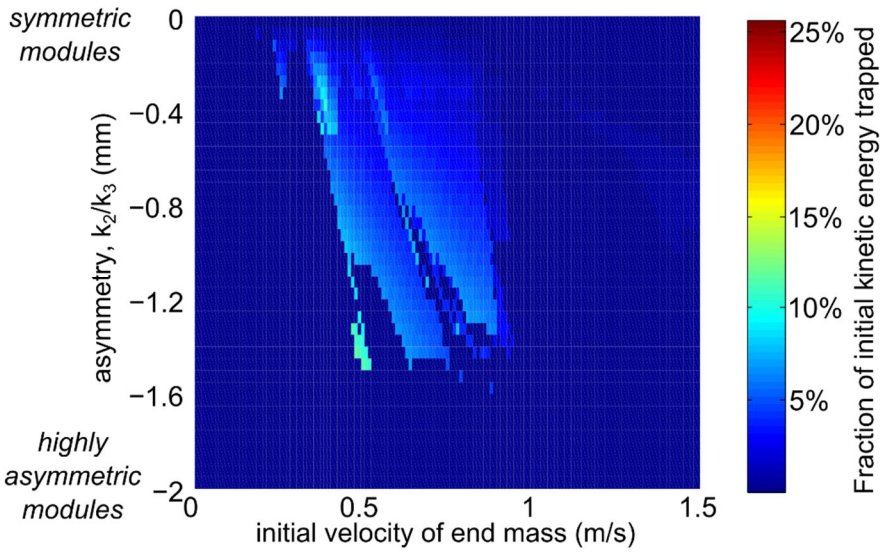

Figure 3-20. Energy trapping performance of a four-module structure for different levels of asymmetry and under various initial velocities $\boldsymbol{v_0}$. The system's modules are also subject to white noise excitation with $\boldsymbol{\sigma = 3\frac{mm}{s^2}}$. The presence of noise compromises energy trapping at large levels of asymmetry.

Figure 3-20 presents the resulting contour plot for simulations where nominal stiffness parameters of each module are those obtained from experimental force-displacement results of a module with 2% beam curvature. Compared with the results of Figure 3-17, the addition of noise is confirmed to greatly inhibit energy capture, with highly asymmetric structures exhibiting no energy trapping. Due to the relative depth of the potential wells of an asymmetrically bistable element and the energy required to overcome the local energy barrier, the presence of noise is more likely to cause transitions from the high-energy configuration to the low-energy configuration than vice-versa. As a result, a structure comprised of highly asymmetric modules is less likely to trap and store energy in high-energy states without the occurrence of noise-induced snap-back. Thus, when designing strain energy capture devices in applications where stochastic influences are non-negligible, the degree of asymmetry should be strategically selected based on the expected magnitude of the noise.

3.5 Strain energy release in asymmetrically multistable chains for actuation and deployment

Building on the results of the previous sections, this section of the chapter explores how transitions between configurations in structures exhibiting asymmetric, multi-well potential energy landscapes can be exploited to release stored elastic potential energy and generate macroscopic length change. While energy capture employs transitions from states with low potential energy to those with high potential energy, the release of trapped energy necessitates an activation of the opposite configuration change back to the lower-energy states. Here, insight is developed on the feasibility and efficiency of the various state transition pathways between the chains' numerous stable configurations on the potential energy landscape.

To facilitate a discussion on the activation energy requirements for these various transition paths, an alternative parametrization of asymmetry is introduced. Considering the force and energy equations for a single asymmetrically bistable element as presented in Eqs. (3-1) and (3-2), the following conditions are applied for consistency: $x_b = 1\text{m}$; $U(x = x_b) = -1\text{J}$; and $U(x = 0) = 0$. This leads to the following stiffness terms:

$$k_1 = Ax_a \tag{3-9a}$$

$$k_2 = -A(1 + x_a) \tag{3-9b}$$

$$k_3 = x_a \tag{3-9c}$$

where

$$A = \frac{12}{1-2x_a} \tag{3-9d}$$

for $-1 < x_a < 0$.

A consequence of the above conditions is that $U(x_b) < U(x_a)$. Thus a transition from x_b to x_a results in a net release of potential energy. Asymmetry in the energy landscape can be quantified by the relative depth of the two potential wells using the ratio $\psi = U(x_a)/U(x_b)$ where $0 < \psi < 1$ due to the prescribed direction of asymmetry. The equilibrium configuration $x = x_a < 0$ is here referred to as the *collapsed state*, and the configuration $x = x_b > 0$ is termed the *extended state* of the bistable element. When considering transitions from collapsed to extended configurations, ψ is the ratio between the energy required to activate the state transition and the potential energy released following activation. Figure 3-21(a) and (b) illustrate the influence of the parameter ψ on the potential energies and force-strain responses for bistable springs subject to the conditions in Eq. (3-9). Stable states are located at local minima of potential energy. These positions correspond to locations where the force response crosses the zero axis with positive slope, and are marked by filled dots. As ψ increases, greater activation energies and forces are necessary to trigger a transition from the collapsed to extended states. Notably, the behavior for $x > 0$ is similar for the range of ψ considered, despite the significant variation in behavior for $x < 0$. Thus, the conditions in Eq. (3-9) along with the parameter ψ provide suitable means to adjust the asymmetry of bistability and force

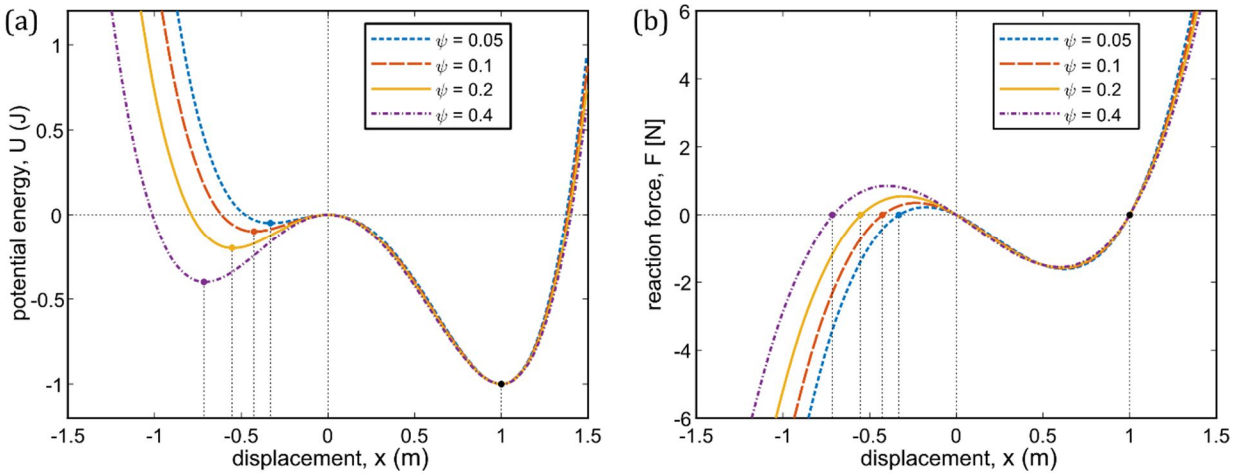

Figure 3-21. (a) Potential energy and (b) reaction force responses for an asymmetrically bistable spring governed by a cubic nonlinear stiffness, for different value of the asymmetry parameter ψ.

and energy responses in the high-energy collapsed state, while minimally affecting the responses in the extended state.

3.5.1 Force and energy landscapes of asymmetrically multistable chains

A schematic of a multistable chain is presented in Figure 3-22, which shows a mechanical system of n asymmetrically bistable elements. The representation is similar to that in Figure 3-14, but clearly denotes the local reaction froces and displacements of relevance in this section. The masses represent the inertia of each element, which exerts a strong influence on the system's dynamic response. Each bistable spring has the characteristic reaction force and potential energy profiles depicted in Figure 3-21.

Figure 3-23 presents the potential energy U and global reaction force response F_4 of a system with $n = 4$ units, as the end displacement x_4 is varied. Only forces and energies corresponding to statically stable configurations are shown. Since only x_4 is prescribed, the internal bistable links are allowed to settle at statically stable equilibria and many combinations of displacements x_1, x_2, x_3 are possible for a given global end displacement x_4. For example, consider the behavior of a chain with $\psi = 0.4$, shown by the dash-dot curves in Figure 3-23, where for an end displacement of $x_4 = -0.2$m,

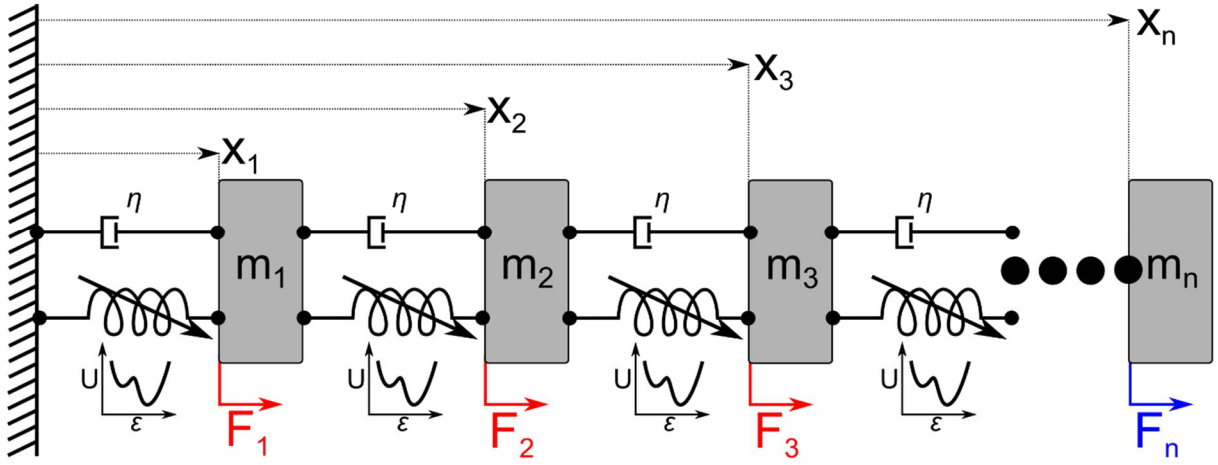

Figure 3-22. Schematic of a mechanical system composed of four masses connected by bistable springs. These bistable springs have cubic linear force response as presented in Eq. (3-1).

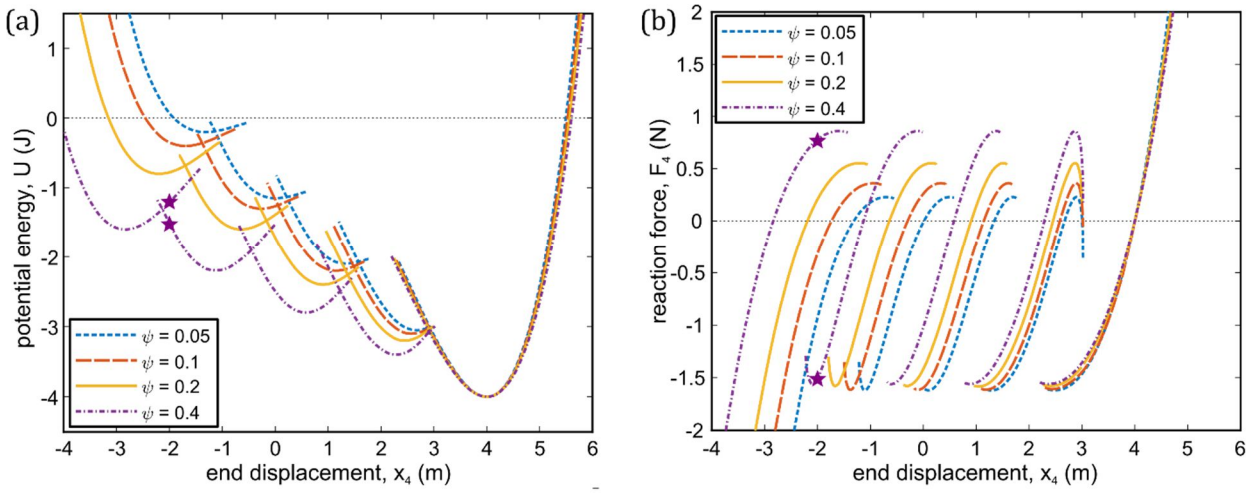

Figure 3-23. (a) Potential energy and (b) global end reaction force responses for a system composed of four serially-connected bistable elements as the end displacement x_4 is varied. Four values of ψ are considered, and only stable configurations are presented. The stars denote an example of a prescribed end displacement with two distinct internal configurations with different potential energies and force responses.

there are two distinct levels of potential energy and reaction force marked by stars. These two points correspond to different combinations of internal displacements that result in distinct global force and energy responses [118,119].

3.5.2 Quasi-static deployment paths of asymmetrically multistable chains

Due to the existence of multiple configurations and the sequence in which individual bistable links are deployed, there exist many possible pathways as the system transitions quasi-statically from a fully collapsed state to a fully extended state. A few examples are presented in Figure 3-24 for a structure with $n = 4$ elements, each with $\psi = 0.1$. To facilitate analysis and discussion in terms of local deformations, the following local strains are introduced:

$$\epsilon_i = x_i - x_{i-1} \text{ for } i \geq 1 \tag{3-10}$$

where $x_0 = 0$. $F(\epsilon_i)$ and $U(\epsilon_i)$ are governed by the single-element responses shown in Figure 3-21. The force response and potential energy landscape for prescribed x_4 are indicated by thin dotted curves. The *end-actuated path* follows a branch until it becomes unstable, and then snaps to a lower-energy configuration. This is repeated until all four bistable links are extended to their low-energy

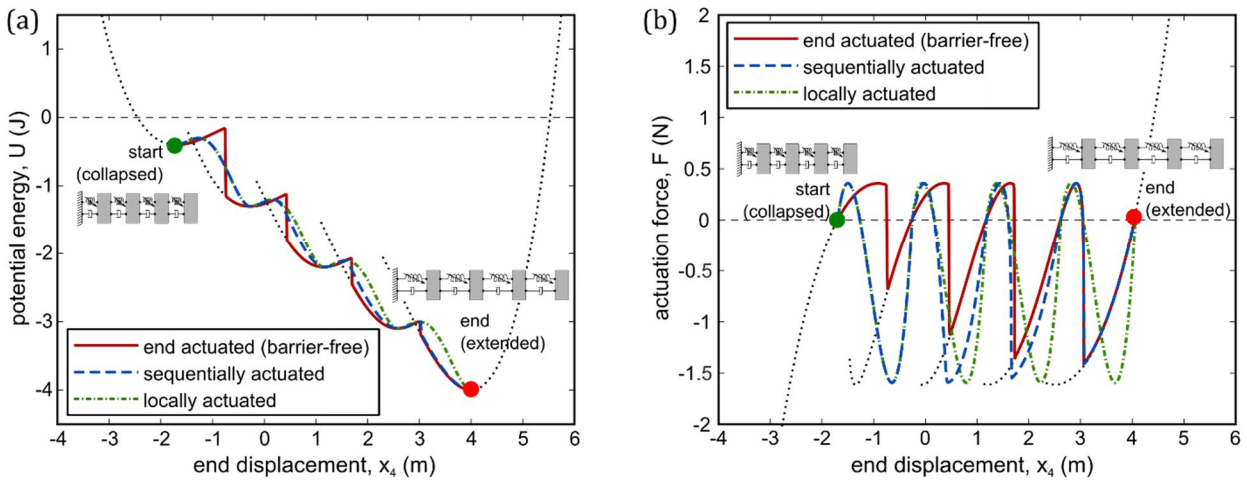

Figure 3-24. (a) Global potential energy and (b) local actuation force for three different quasi-static deployment paths of a system composed of four bistable elements with $\psi = 0.1$.

states. The end-actuated path is also known as a *barrier-free* path as it does not require any local energy barriers to be overcome. The system is always at a local energy minimum for a prescribed end strain x_4. The barrier-free path also maximizes hysteresis when considering a full cycle of deployment to the extended, low-energy state and compression back to the collapsed topology [106,109],

The trajectory that follows potential energy minima is known as the *Maxwell path.* This path involves internal state transitions that cross large local energy barriers for a fixed global topology [106]. These local energy barriers are overcome in systems that are subjected to local thermal noise and fluctuations, but represent an impractical transition path for controlled, deterministic systems [105,120]. However, the Maxwell path can be approximated here by enforcing conditions that result in only local state transitions. For example, the i^{th} bistable link may be deployed by fixing x_{i-1} while x_i is varied, along what is here referred to as the *locally-actuated path*. Thus, only ϵ_i undergoes a transition from ϵ_a to ϵ_b, while all other bistable links remain at an energy minimum with zero stress or local reaction force. This process is repeated for $i = 1 \dots n$. The dash-dot curves in Figure 3-24 illustrate the local actuation force required and total strain energy of the system along this path as a function of global displacement x_4. Since local state transitions are employed, the path does not overlap the global force

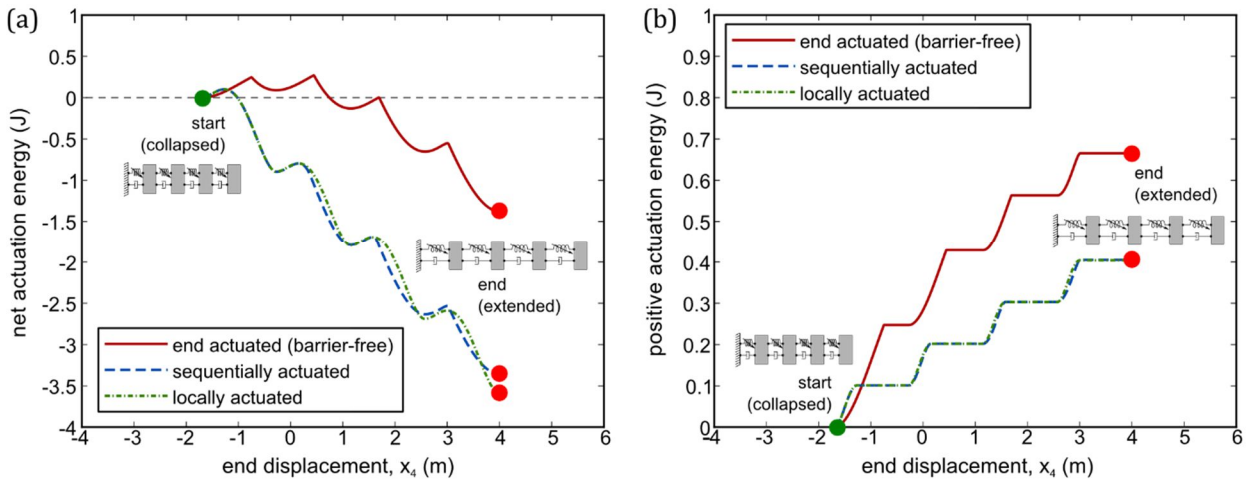

Figure 3-25. (a) Net and (b) positive actuation energies for the deployment of a four-element asymmetrically multistable chain, indicating that sequential or local actuation is more efficient than the barrier-free path.

and energy profiles of the thin dotted curve. A variant of the locally actuated path is a *sequentially-actuated path*, denoted by the dashed curve in Figure 3-24. Starting from the fully collapsed configuration, displacements $x_i = x_1, \dots, x_n$ are sequentially prescribed until the sub-system consisting of element masses $m_1, \dots, m_i$ is at the extended state. The sub-system is always at a static equilibrium as x_i is varied, thus there may be non-zero local stresses among the elements in this subsystem due to the force applied to mass m_i. This represents the main distinction from the locally actuated path, where only the i^{th} bistable element experiences local stresses.

The net work performed at the point of displacement control as the structure is extended is shown in Figure 3-25(a), and is obtained by direct integration of the corresponding force curves in Figure 3-24(a). Figure 3-25(b) presents the positive work performed during extension, considering only regions where the actuation force F satisfies $F > 0$, and reflecting the fact that mechanical work performed *on* an actuator is generally not recoverable. In effect, the positive actuation work is a measure of the cumulative activation energy required to deploy the chain to a given length. Results clearly indicate that extending the chain through local or sequential actuation of individual bistable links is more energy-efficient than the end-actuated, barrier-free path.

3.5.3 Dynamics of chain deployment

While the prior section provides insight into the different deployment pathways of a multistable chain, its findings are insufficient to understand the behavior when system dynamics are considered. Under dynamic loads, the structure will not smoothly follow the reaction force and energy profiles presented in Figure 3-23 and Figure 3-24, and the kinetic energy of the masses plays an important role. In fact, the energy released from one element as it transitions from high-to-low potential configuration may be sufficient to overcome the energy barrier of the subsequent link, resulting in a self-powered deployment sequence that propagates along the chain.

To better understand the conditions that can lead to this phenomenon, numerical studies are conducted on a four-element chain. Normalized masses m_i and linear damping coefficient η of each element are selected such that linearized natural frequencies and damping ratios in the vicinity of the low-energy stable state of each element are $w_n = 1$ and $\xi = 0.4$, respectively. The selection of asymmetry parameter $\psi = 0.1$ means that stiffness terms are identical to the quasi-static case considered in Figure 3-24 and Figure 3-25. The system is initially in the fully collapsed configurations, where all elements are in their high-potential stable state. One of the masses m_i is prescribed an initial velocity v_0, hence the initial energy of the system is $T_0 = 0.5(m_i v_0^2)$. The remaining elements are initially at rest. Figure 3-26 presents the transient results for an initial kinetic energy of $T_0 = 0.3\ J$ applied to (a) the first element, and (b) the end element. All element displacements x_i are offset for clarity. The thin dotted lines in Figure 3-26 denote displacements x_4 of the end mass corresponding to increasing numbers of state transitions. When the initial energy is applied to the first element, there is no configuration change and the initial and final element displacements are the same. Conversely, when the same energy is applied to the last element, a sequence of state switches is triggered. All four elements switch to the low energy state, fully deploying the structure. Notably, the initial energy $T_0 = 0.3\ J$ is less than the total activation energy required to quasi-statically deploy the structure as presented in Figure 3-25(b), despite the presence of dissipation in the dynamic case.

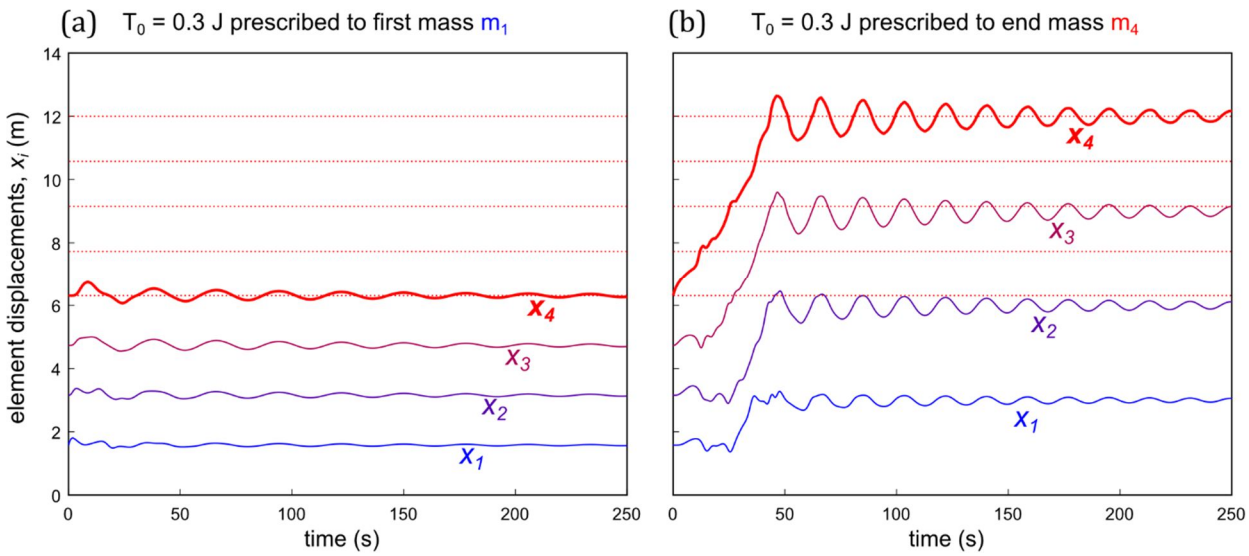

Figure 3-26. Transient results of element displacements in consequence to an impulsive excitation applied to (a) the first element and (b) last element of a four-element chain with $\psi = 0.1$, and a linearized damping ratio $\zeta = 0.4$ in the low-energy state. The same initial kinetic energy is prescribed in both cases, yet the system deploys to its low-energy configuration only if the initial energy is prescribed to the last element.

This implies that the impulse applied to the end element is sufficient to trigger a sequence of state transitions activated by the energy released from the previous transition event, and motivates further investigation to uncover the distinct transition pathways when considering dynamic rather than quasi-static deployment.

3.5.4 Experimental demonstration

The test bed presented in Figure 3-27(a) facilitates experimental investigation of the behavior shown in Figure 3-26. The apparatus consists of four nominally identical modules fabricated using a 3D printer. Bistable interactions between adjacent modules are achieved using a combination of spring steel beams to provide positive stiffness, and permanent magnets to provide negative stiffness. Asymmetry is generated by introducing an offset between the position of magnets and the mounting points of the spring steel beams. Linear electromagnetic actuators are mounted to each module, providing means to deliver impulsive force to an element. The entire assembly is on mounted

rails via linear bearings. A laser vibrometer mounted to the table records the displacement and velocity of the end element m_4, while a video camera records the experiments from above.

Figure 3-27(b) presents aggregate results from repeated tests where the structure is initially in the high-energy collapsed state and an individual element is impacted by the solenoid actuator. The horizontal axis shows current applied to the solenoid, which is related to the measure of initial energy, and the vertical axis indicates the number of elements deployed to the low-energy state in consequence to the impulse. Five tests are conducted for each condition. The points indicate the mean and error bars indicate standard deviation. A minimum current level is required before snap-through events are activated. More elements are deployed when applying this critical current level to the last element in the chain as compared to the first element, which corroborates the observations from Figure 3-26.

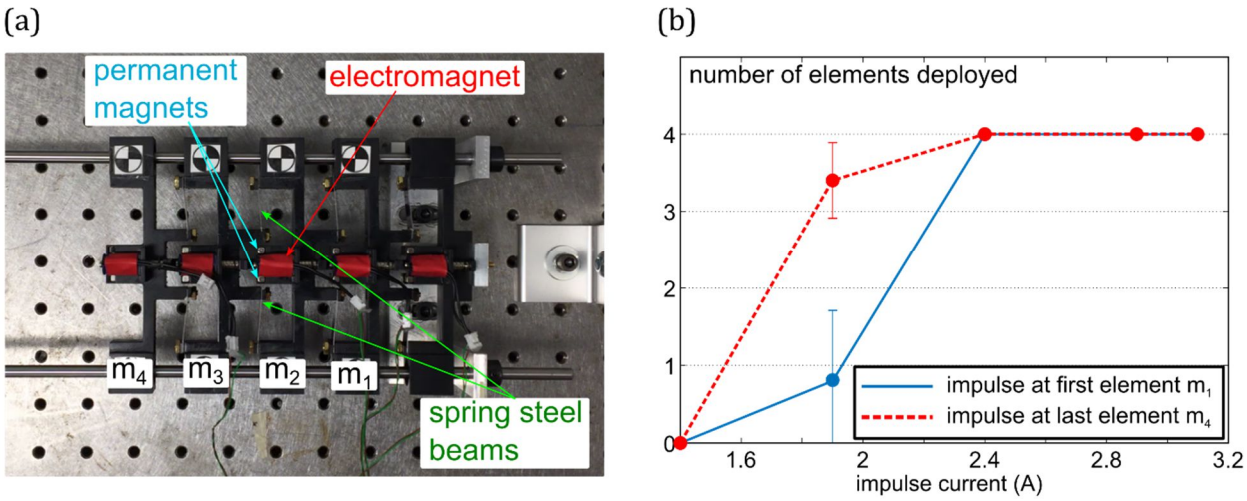

Figure 3-27. (a) Testbed to facilitate dynamic experiment into deployment of asymmetrically multistable chains. (b) Aggregate results from $n = 5$ trials at each condition, showing the number of deployed elements in consequence to impulsive excitation at the first (solid line) and last (dashed line) element. Applying the impulse to the last element as opposed to the first element is shown to result in more deployed elements for lower input energy levels

3.5.5 Analysis and discussion

The behavior illustrated in Figure 3-27 is observed for a range of asymmetries and initial energies. To facilitate a more comparison for impulse thresholds that result in deployment of a four-element chain, Figure 3-28 presents contour plots obtained from numerical analyses, colored by the number of bistable links deployed in consequence to an impulse applied (a) at the first element, closest to the base of the structure and (b) at the last element in the chain. All elements are initially in the high-energy, collapsed state. Results are presented for a range of initial kinetic energy T_0 and asymmetry ψ, while linear viscous damping coefficient is such that the linearized damping ratio in the low energy state is $\zeta = 0.4$. When the impulse is applied to the last element in the chain, the minimum energy required to trigger deployment is lower than the case for which the impulse is applied at the base, and this behavior is noted for all levels of asymmetry considered. Furthermore, full deployment, where all four links are deployed, also typically requires less energy when the impulse is applied to the last element in the chain. The dotted lines show the activation energy required to trigger a transition in a *single* element, and the dashed lines show the activation energy

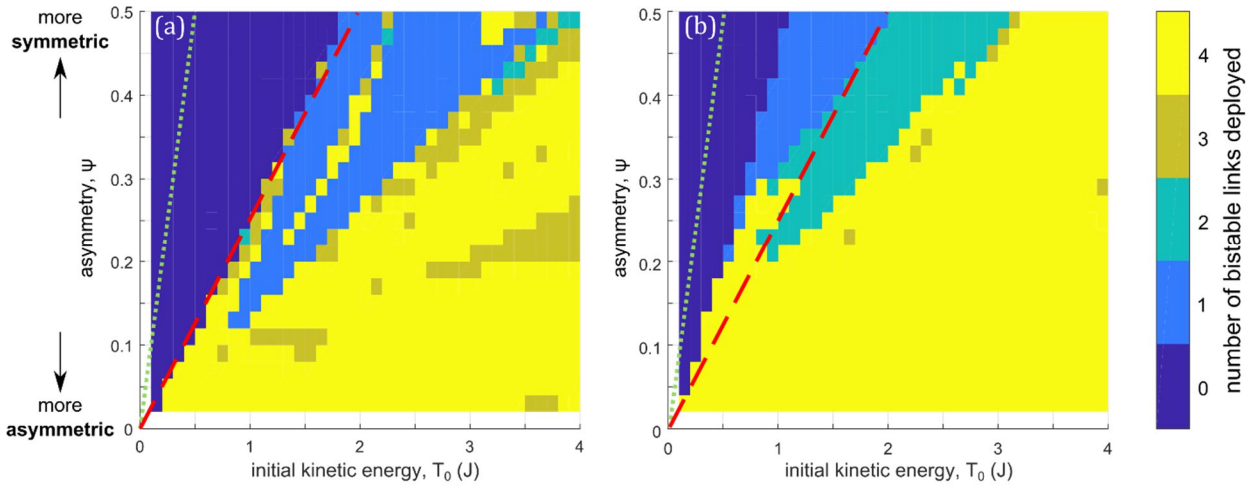

Figure 3-28. Number of bistable links deployed in consequence to an impulse applied (a) at the first element, closest to the base of the structure and (b) at the last element in the four-element chain. Asymmetry and the length of the chain are varied. Linearized damping ratio is $\zeta = 0.4$ in the low energy state for each element. Dotted lines show the activation energy required to trigger a transition in a single element. Dashed lines show the activation energy required to deploy the entire chain under quasi-static, locally-actuated conditions.

required to deploy the *entire* chain under the quasi-static, locally-actuated conditions described in Section 3.6.2. There is a region of parameters in Figure 3-28(b) for which dynamic deployment of the four-element chain requires less energy than the quasi-static case, and the cases considered in Figure 3-26 lie within this region. Analysis of time-series data shows that deployment of bistable links in the case where the initial impulse is applied closest to the base does not begin at the base element itself, but at the free end, after the initial impulse has propagated through the entire chain.

The discussion has thus far been limited to a four-element chain, but the benefits of dynamic deployment may be further enhanced by considering chains of greater length, where conversion of potential to kinetic energy can trigger further state transitions along the chain. Figure 3-29 presents results in a manner similar to Figure 3-28, but where the chain length is varied along the vertical axis and the asymmetry parameter $\psi = 0.1$ for all elements. As before, dotted and dashed lines show the quasi-static activation energy for the deployment of a single element, and the entire chain, respectively. Figure 3-29(a) shows results when an impulse is applied to the first element, closest to the fixed base, while (b) presents the case when the impulse is applied to the last element in the chain.

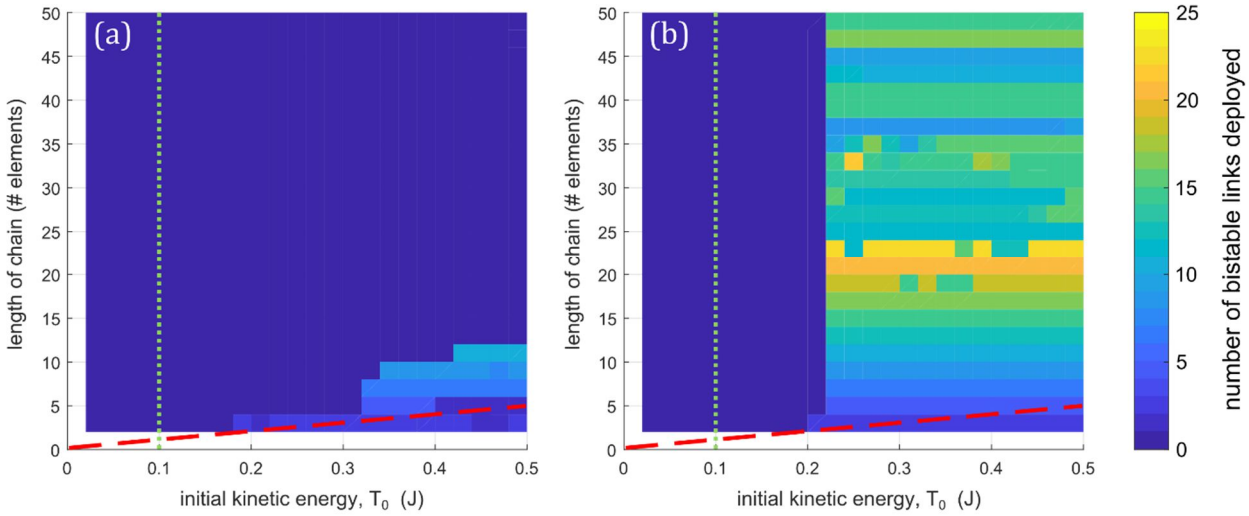

Figure 3-29. Number of bistable links deployed in consequence to an impulse applied (a) at the first element, closest to the base of the structure and (b) at the last element in the chain. Initial kinetic energy and length of the chain are varied. Linearized damping ratio $\zeta = 0.4$ in the low energy state for each element, and asymmetry parameter $\psi = 0.1$. Dotted lines show the activation energy required to trigger a transition in a single element. Dashed lines show the activation energy required to deploy the entire chain under the quasi-static, locally-actuated conditions.

Most of the parameter space considered in Figure 3-29(a) does not result in deployment, with the exception of short chains subject to an impulse with large energy. This, again, is due to the links being deployed after the initial impulse has propagated through the length of the entire chain. In longer chains, more energy is likely to be dispersed and dissipated before the last element begins to oscillate, and hence these oscillations are less likely to overcome the local energy barrier required for link deployment.

In contrast, there is a clear minimum of energy in Figure 3-29(b) above which deployment is observed for all chain lengths considered. For impulses with an energy above this threshold, chains up to a length of approximately 20 elements are completely deployed. Since the transient dynamics of long multistable chains are a complex interaction of large-amplitude transition waves and smaller-amplitude oscillations, both of which can be reflected at the fixed and free boundaries [121], the deployment is general not sequential. For large chain length in Figure 3-29(b), not all bistable links are extended, despite an impulse of sufficient energy to trigger deployment of some elements in the chain. Nevertheless, the findings indicate the ability to exploit stored energy to trigger dynamic deployment and length change of multistable chains with much less energy than needed for equivalent quasi-static deployment.

Making certain simplifying assumptions facilitates further intuition and insight into the reasons behind the significantly different behavior in consequence to impulses applied to the two ends of the chain. This is achieved by considering the transient dynamics only on the individual module at which the impulse is provided. Based on the assumptions summarized in Figure 3-30, the energy barrier for the case when the impulse is applied to the first element is augmented as:

$$U_1^* = U_1 - \frac{1}{2}\left(\frac{d^2U_1}{d_x^2}\right)_{x_a} x_a^2 \tag{3-11}$$

where U_1 is the nominal potential energy at the high-energy well corresponding to the initial state of each element, while x_a is the bistable spring deflection from the neutral position at this configuration.

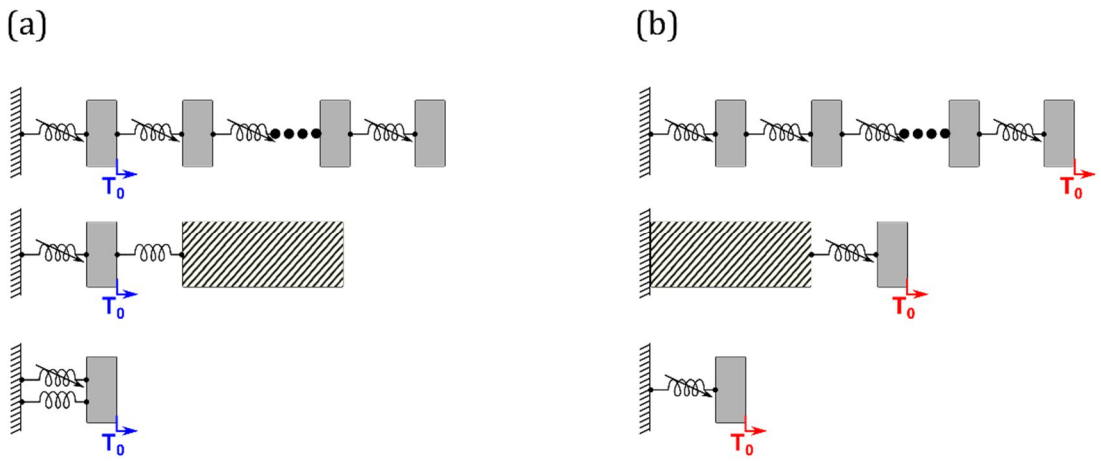

Figure 3-30. Simplifying assumptions used to facilitate prediction of the onset of energy-releasing state transitions when an impulse is applied at the (a) first element in the chain and (b) last element in the chain. The key assumption made here is that the impulsive excitation causes the element to transition before a significant proportion of the initial kinetic energy has an opportunity to disperse among other elements in the chain. When an impulse if applied at the first element, the influence of the stiffness connected to the rest of the chain must be included when computing the energy barrier that must be crossed in order to initiate state transitions.

Note that U_1^* now includes the additional energy barrier associated with overcoming the linearized stiffness in this potential over the displacement x_a, reflecting the influence of the additional stiffness element in Figure 3-30(a). According to the derived stiffness parameters of Eq. (3-9) based on the asymmetry and energy barrier, the approach described earlier in this chapter and in Appendix B can be applied to predict the onset of energy-releasing state transitions. As an illustrative example, a ten-element chain is considered in Figure 3-31. Contour plots showing the number of elements deployed due to impulsive excitations of various magnitude at (a) the first element in the chain and (b) the last element in the chain. The red boundary shown denotes the onset of energy-releasing state transitions as predicted from the single-element approximation of Figure 3-30, demonstrating a good quantitative prediction in both cases.

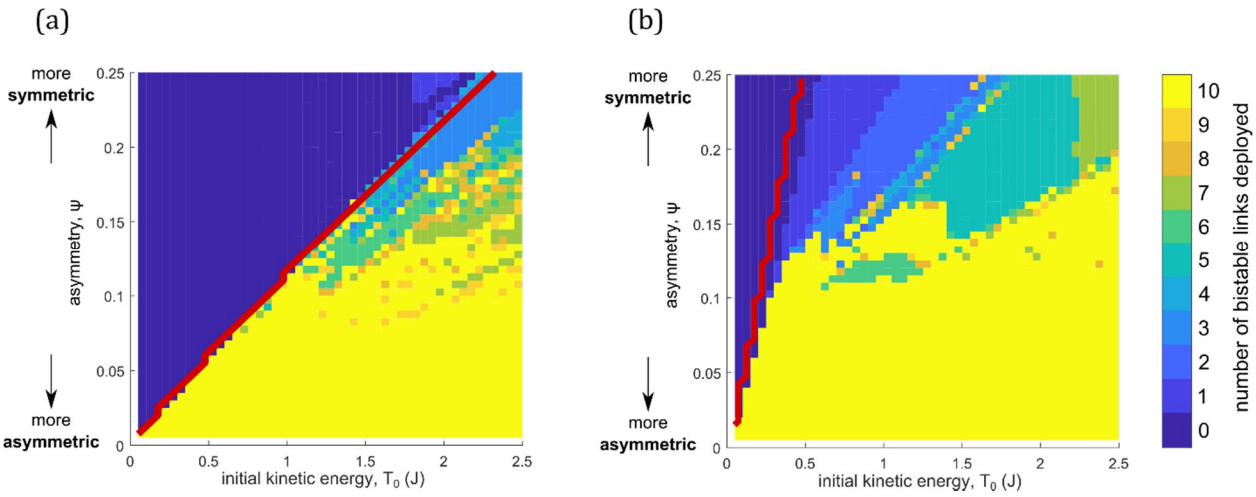

Figure 3-31. Number of bistable links deployed in consequence to an impulse applied (a) at the first element, closest to the base of the structure and (b) at the last element in a ten-element chain. Initial kinetic energy and asymmetry are varied. The red solid denotes the onset for state-transitions as predicted by the single-element analysis approach using the simplifying assumptions summarized in Figure 3-32.

3.6 Conclusions

The energetic versatility and functionality exhibited by skeletal muscle provides great inspiration for the development of advanced structures and materials. Inspired by these characteristics, and by the mechanics of muscle micro- and nano-scale building blocks – sarcomeres and cross-bridges – this chapter investigates the ability of modular structures composed of asymmetrically bistable constituents to capture and store recoverable strain energy in higher-energy stable configurations. Individual one-dimensional modules are designed, fabricated, and comprehensively studied, providing insight into how geometric parameters influence asymmetrically bistable strain energy landscapes. System identification enables analytical prediction of the transient dynamics of asymmetrically bistable modules using Jacobi elliptic functions. Modular assembly of asymmetrically bistable constituents is then explored, generating complex, multiwall strain energy landscapes and enhancing opportunities for strain energy capture by exploiting the different energy levels of the structure's stable configurations. The energy trapping behaviors of single modules and multiple-

module structures under impulsive excitations is investigated, demonstrating their ability to capture a portion of the initial kinetic energy of the excitation as recoverable strain energy. The influences of asymmetry, dissipation, and noise are explored, revealing a balance between maximizing the amount of captured energy and minimizing the risk of the structure snapping back to its low-energy state.

To study the release of this stored energy to enable efficient actuation and deployment, a comparison of quasi-static state transition pathways of single- and multi-element structures is undertaken. Analysis shows that deployment through a series of localized, sequential transition events requires less total activation energy and is more efficient than deployment by controlling the global end displacement along a barrier-free path. When dynamics are considered, the activation energy required for deployment may be *less* than the quasi-static case by leveraging the energy released from one element to facilitate the activation of subsequent state-transitions. Numerical and experimental results demonstrate that the location of the initial energy input to activate is influential in determining the effectiveness in initiating full deployment of the asymmetrically multistable chain.

Chapter 4. Modular material systems inspired by skeletal muscle's microscale geometry and architecture

4.1 Introduction

Many of the characteristics that make skeletal muscle a great inspiration for advanced structural and material systems, such as robustness, versatility, and adaptability [5,14], arise from interactions demonstrated between constituents across its various length scales, from muscle fibers down to microscale sarcomeres and nanoscale cross-bridges [4,54]. Across these different length scales, skeletal muscle's constituents take advantage of geometries and multidimensionality for force generation or length change along a desired axis. Myocytes, the striated cells commonly called muscle fibers, consist of bundles of myofibrils that are sectioned into units called sarcomeres. The length-tension responses of sarcomeres, the basic force generating unit of muscle, are strongly governed by the spacing between its adjacent thin and thick filaments [37]. In the macroscale, a muscle's fiber architecture and orientation depend on its location and function. Certain muscles in the hands, shoulders, and quadriceps have a *pennate* architecture, where fibers are oriented obliquely to the tendon and whole muscle motions [5,22]. Pennation helps prevent over-straining during large displacements and enhances force generation by exploiting an effective mechanical gearing effect [7,17]. The contractile forces observed in pennate muscles depend on the amount of overlap between actin and myosin filaments of the sarcomere contractile units as well as the fiber pennation angle [23,122].

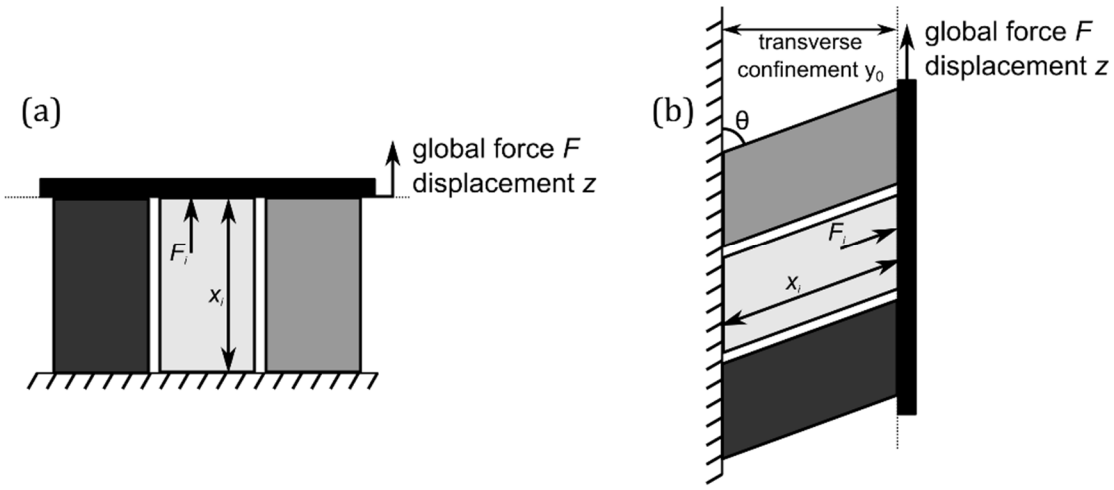

Figure 4-1. (a) Parallel and (b) pennate configurations of three constituent elements.

Inspired by these aforementioned behaviors at different scales, this chapter investigates how the incorporation of multidimensionality and interactions between axial and transverse displacements influences the mechanics of structures exhibiting multistability and metastability. In contrast to the dynamic features studied in previous sections, this chapter will focus primarily on how modulation of transverse effects and system geometries can influence the mechanical response of structural and material systems. However, as illustrated in Chapters 2 and 3, a thorough understanding of static features provides valuable knowledge and intuition on the system's dynamic response.

There are several examples of multistable structures that rely on fixed transverse confinements to enforce post-buckled configurations of their constituent elements when subject to axial loads [96,104,123,124]. However, the advantageous force and velocity amplifications observed in pennate muscles arise from global force and displacement actions that are not aligned with the motions of its constituent fibers [68]. Furthermore, metastability is an important feature in skeletal muscle mechanics that helps explain its rapid, passive tension recovery in response to length change and the coordinated force generation of sarcomeres [40,54]. Therefore, this chapter aims to uncover the rich mechanics that can arise in structural and material systems that specifically combine multi- and

metastability with oblique motions to activate state transitions. To illustrate this concept, Figure 4-1(a) depicts three elements in a parallel configuration subject to a single global displacement z, which is aligned with the axes of the elements' individual deformations x_i. Each of these elements may individually exhibit bistability or metastability, and the global reaction force F is the sum of the individual modules' reaction forces F_i in consequence to the global displacement. For the pennate architecture presented in Figure 4-1(b) under prescribed transverse, horizontal confinement y_0, the global displacement z along the vertical axis is oblique to individual module deformations x_i, and the global reaction force F depends on the individual modules' reaction forces F_i and orientation angle θ.

4.1.1 Preliminary experimental investigation

Investigation of the mechanics facilitated by the oblique orientation of metastable and multistable constituents is undertaken using silicone rubber specimens with circular voids. Such architected material systems have been shown to exhibit intriguing mechanical properties, including

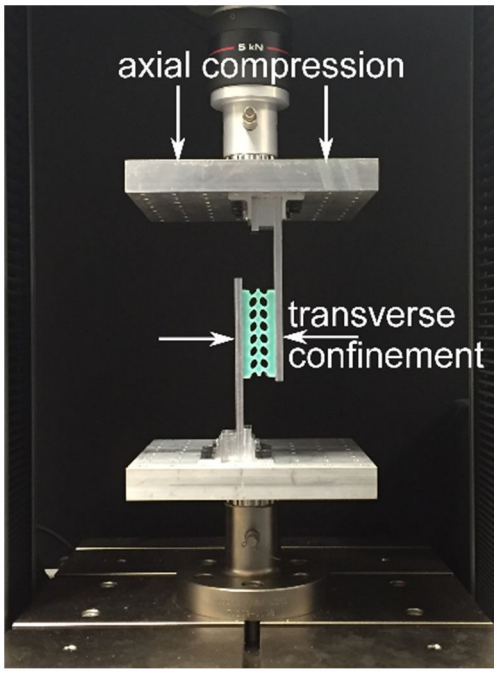

Figure 4-2. Experimental setup indicating directions of horizontal transverse confinement and vertical axial compression.

tailorable buckling [124], negative Poisson's ratio [125], and pattern switching [126,127]. Notably, this architecture may exhibit metastability – the existence of multiple possible internal configurations for prescribed global boundary conditions [124,128]. While the influence of transverse confinement on pattern switching has been identified [124], the mechanics that arise from their oblique global motions as depicted in Figure 4-1, analogous to large macroscopic shear, have not yet been explored.

Specimens are fabricated from a two-component silicone rubber (Smooth-On Mold Star 15 SLOW [129]) mixed at a 1:1 ratio. Following mixture, the rubber is allowed to rest for 15 minutes to allow trapped air bubbles to escape before being poured into molds fabricated using a stereolithographic 3D printer (Form 2, Formlabs Inc., USA). The printer employs a black photopolymer resin (GPBK02, Formlabs Inc., USA) a 50 μm print resolution. The silicone rubber is cured for four hours at room temperature (23 °C) before being extracted from the molds, and the specimens are allowed to dry for at least 24 hours prior to testing. Specimens are tested as depicted in Figure 4-2. Transverse confinement is provided in the horizontal direction by 6.4 mm thick aluminum beams clamped to the upper and lower fixtures of an Instron 5950 universal testing machine. Uniaxial compression tests are performed, causing the specimen's right hand side to be displaced vertically with respect to the left hand side.

To gain preliminary insight, uniaxial compression tests are performed on a specimen with a length of 70 mm and width of 28 mm. Circular voids with a diameter of 8 mm are arranged in two columns such that transverse compression causes the voids to collapse together in a predictable manner. The center-to-center distance between adjacent voids is 10 mm. The experimental setup presented in Figure 4-2 shows this specimen under a transverse confinement of 25.4 mm, imparting a transverse compression of 2.6 mm. Force-displacement profiles obtained from uniaxial compression tests in this configuration are shown in Figure 4-3(a). The solid and dotted curves represent two different orientations of the specimen. The observed reaction force exhibits a slight negative slope, indicating negative stiffness, between vertical displacements of approximately -4 mm

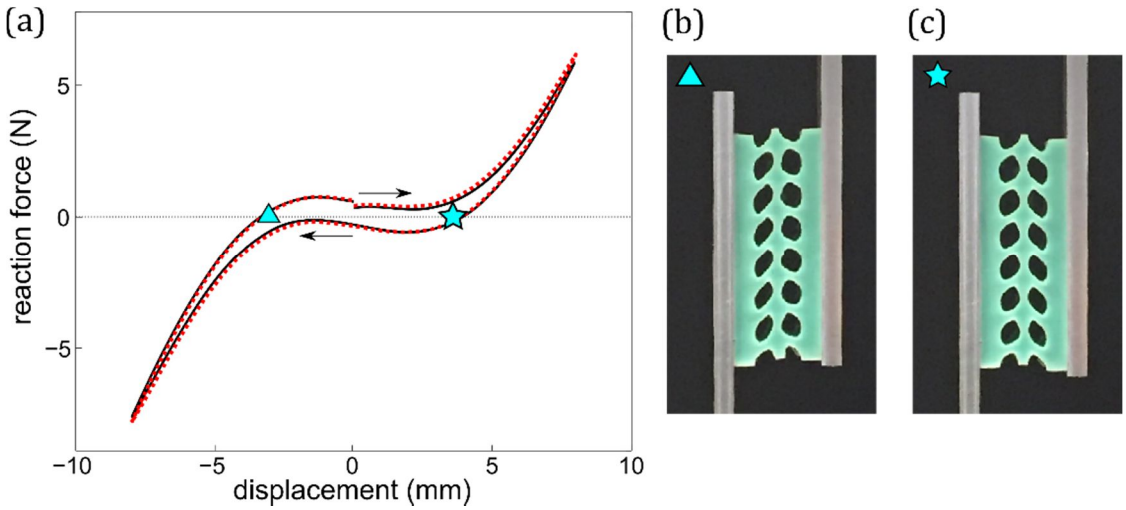

Figure 4-3. (a) Force-displacement profile under 2.6 mm transverse compression and a vertical displacement rate of 0.1 mm/s. The solid and dotted curves show responses from specimen orientations that are rotated by 180 degrees. (b,c) Still images showing deformations of the specimen at the corresponding marked points on the force-displacement profile.

and 4 mm. Two locations where the reaction force crosses the horizontal axis are marked by a triangle and star in Figure 4-3(a), while Figure 4-3(b) and (c) present images of the corresponding configurations. The specimen exhibits relatively small local deformations under these two prescribed global displacements.

Under a transverse confinement of 19.1 mm, equivalent to a compression of 8.9 mm from the specimen's natural width, uniaxial compression tests yield the highly non-monotonic reaction force-displacement profile presented in Figure 4-4(a). The images in Figure 4-4 (b-d) depict the deformations at three distinct configurations where the measured reaction force curves cross the zero axis with positive slope, denoting stable configurations. Compared with the results shown in Figure 4-3, the local deformations for these configurations are much larger and the circular voids are almost entirely collapsed. In addition, there is an increased discrepancy between loading and unloading paths, which arises due to contact and friction between the silicone rubber sections surrounding the voids.

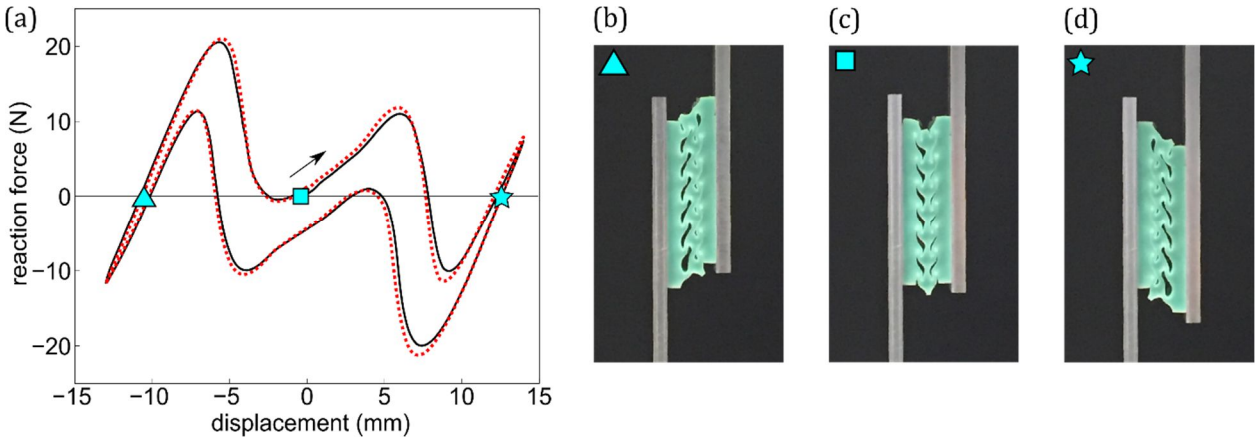

Figure 4-4. (a) Force-displacement profile under 8.9 mm transverse compression and a vertical displacement rate of 0.1 mm/s. The solid and dotted curves show responses from specimen orientations that are rotated by 180 degrees. (b-d) Images showing deformations of the specimen at the corresponding marked points on the force-displacement profile.

The results of Figure 4-3 and Figure 4-4 demonstrate the significant influence of transverse confinement and oblique motions on the multistability of a material specimen with circular voids. If the material is considered as a section of a bulk architected material, the outcomes illustrate highly non-monotonic shear stresses. However, despite exhibiting strong multistability, there is no observed metastability. For a given vertical displacement, the distortion of all voids in each of the two columns is almost identical. Furthermore, the voids' deformations are uniform. The deformed shapes of the collapsed voids at the both the top and bottom of the specimen are the same. An architected material with local deformations that vary throughout its domain can more fully exploit the advantages of combining metastability and modularity.

4.2 An architected material system inspired by skeletal muscle's microscale geometry

To achieve locally-targeted deformations that vary across the material domain, an architecture is developed that is inspired by skeletal muscle's exploitation of geometric confinements for length and force response controls. Specifically, the proposed material system takes inspiration from the arrangement of attached cross-bridge elements in sarcomere contractile units, presented in Figure 4-5(c-d). The geometric frustrations imposed by sarcomere length and lattice spacing geometric influence the mechanics of the cross-bridge power stroke [37,57,130], in which the myosin head undergoes a conformational change due to adenosine triphosphate (ATP) hydrolysis. These constraints also influence its ability to store strain energy [6]. Cross-bridges are oriented obliquely to actin and myosin filaments, and there is a strong interaction between axial contractile motions, transverse or radial forces, and elastic energy storage in skeletal muscle cross-bridges [38]. The material architecture under consideration is presented in Figure 4-5(e-h), and is composed of unit modules consisting of four circular voids. These units buckle under compression and undergo

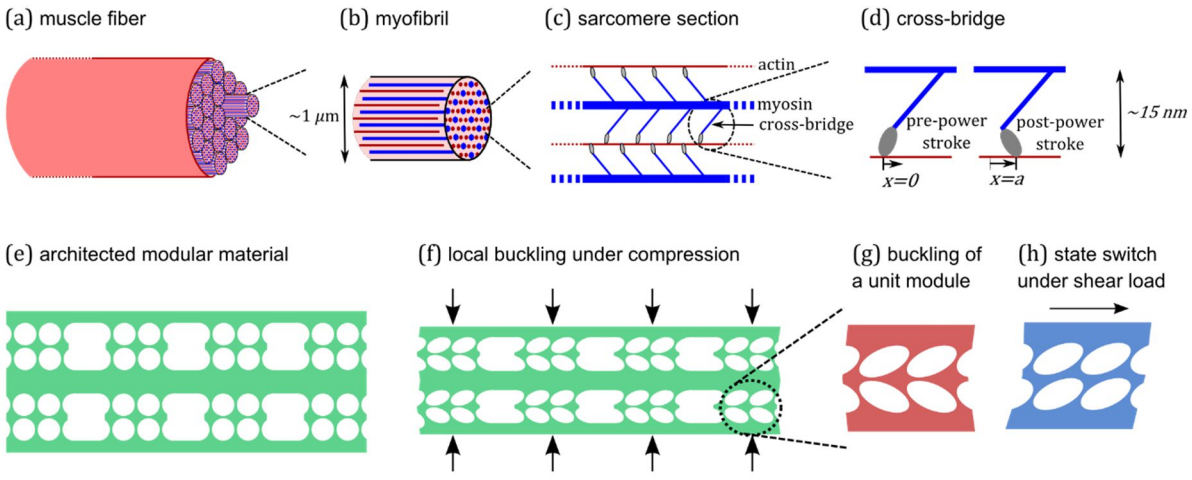

Figure 4-5. (a) Muscle fibers are composed of bundles of rod-like myofibrils (b), which consist of actin and myosin proteins arranged in a lattice and sectioned into units called sarcomeres (c). Actin and myosin are connected by cross-bridges (d), with power-stroke mechanics influenced by lattice geometry. (e) A section of proposed architected modular material system subject to compression (f), resulting in local buckling of constituent modules (g). Application of a shear load causes a state switch (h) in the void pattern.

discrete state-switches when subjected to shear loads. Neighboring units are separated by larger, rectangular voids which allow adjacent modules to express unique deformed topologies.

The unique topologies of adjacent four-void modules within a larger section of the material reflect the fact that each attached cross-bridge may be in either a pre- or post-power stroke state. While there is coordination among cross-bridges in a sarcomere, there are a large number of possible combinations of cross-bridge conformations in a single sarcomere [54]. Thus, myofibrils and sarcomere contractile units may exhibit passive *multistability*, the existence of numerous possible myofibril lengths for a given external load. Furthermore, they exhibit *metastability*, the existence of multiple possible combinations of cross-bridge conformations for a prescribed sarcomere length [13,54,75]. This metastability has been proposed as the key ingredient that may explain the passive tension recovery of skeletal muscle fibers at very short time scales [54].

The architected material proposed here indeed gives rise to both multistability and metastability. Multiple equilibrium topologies of the modular constituents are seen in in Figure 4-6, which shows undeformed and deformed topologies for specimens composed of (a) a 2x2 arrangement of modules,

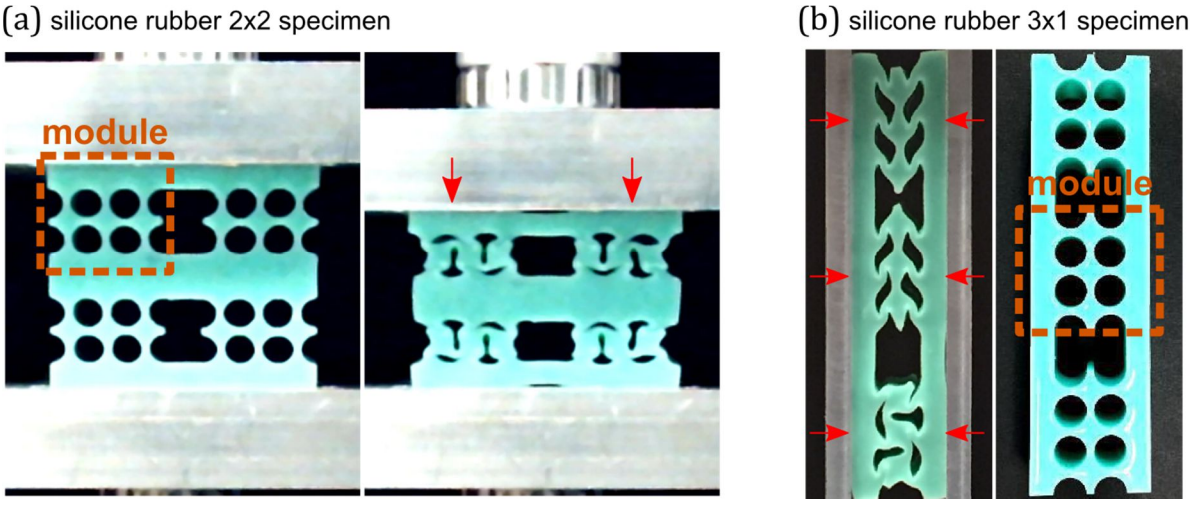

Figure 4-6. Specimens highlighting a four-void constituent module with a natural width of 30 mm. (b) two serially-connected sets of two modules in parallel showing local buckling under compression. (b) A three-module specimen under transverse confinement, where each of the three modules exhibits a different deformation patterns despite being subject to the same confinement.

and (b) a 3x1 arrangement. A single four-void constituent module is highlighted for reference, and all modules are nominally identical. The two examples clearly demonstrate how the architected material design incorporating large voids to separate modules can lead to deformation patters that are localized to each module. Further, the 3x1 specimen clearly shows the existence of multiple statically stable equilibrium topologies for the same level of compression. To gain a comprehensive understanding of the unique mechanics afforded by the proposed material arrangement at the unit module level, numerical and experimental investigations are carried out on a single four-void constituent module.

4.3 Experimental and numerical analysis methods

Key geometric parameters for the architected material specimens are presented in Figure 4-7(a). The four voids have alternating diameters d_1 and d_2. All specimens have height $h = 15$ mm, width $w = 15$ mm, wall thickness $t = 0.88$ mm, and average void diameter $\frac{d_1+d_2}{2} = 4.12$ mm. The center-to-center distance between adjacent voids is 5 mm. A transverse compression δ_x as shown in Figure

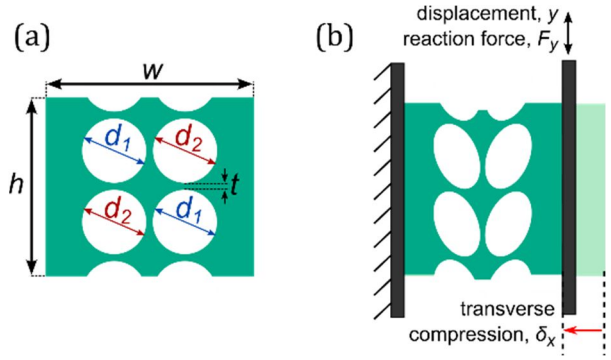

Figure 4-7. (a) Schematic of a unit module considered in this research, indicating important dimensions. (b) Transverse compression $\boldsymbol{\delta_x}$ applied by aluminum plates. As shown in Figure 4-2, the plate on the left side is clamped to the base of a tensile testing machine, while the plate on the right side is clamped to the upper fixture and load cell.

4-7(b) is enforced by rigid aluminum plates clamped to the upper and lower fixtures of an Instron 5950 universal testing machine. Initial configurations are manually set by adjusting the module after it is placed in the test fixture. This is necessary to fully explore the range of displacements in which the various configurations are observed.

To supplement and guide experimental efforts, and provide a deeper understanding of state-switching behaviors in the architected material, numerical simulations are conducted using the ABAQUS software package (Dassault Systèmes Simulia Corp., USA). The Mold Star 15 SLOW silicone rubber material is modelled using a Neo-Hookean approximation. Young's modulus is obtained from a fit to experimental data for bulk material specimens, as shown in Figure 4-8. The uniaxial Neo-Hookean stress-strain relationship for an incompressible material [131] is:

$$\sigma = 2C_1\left(\epsilon + 1 - \frac{1}{(\epsilon+1)^2}\right) \tag{4.1}$$

where C_1 is a material constant equal to $\frac{E}{6}$ for the incompressible case, and σ and ϵ are the engineering stress and strain, respectively. The finite element model employs a nearly-incompressible Poisson's

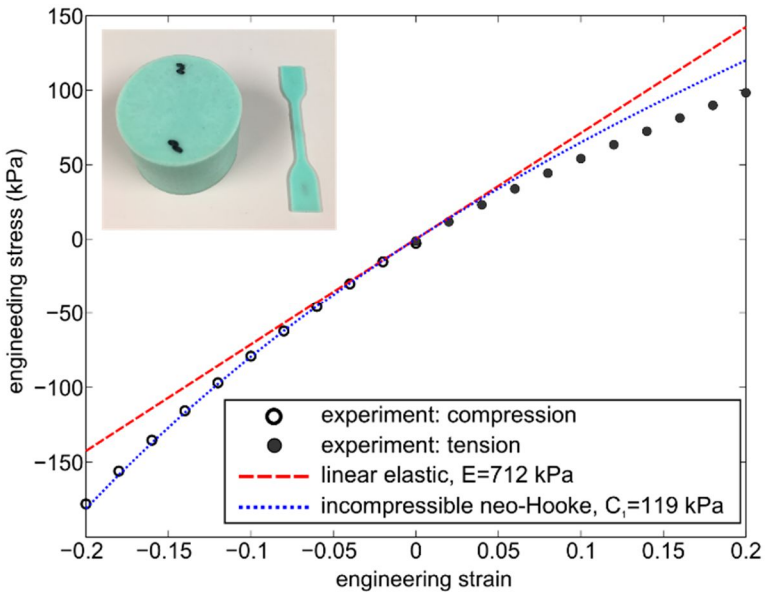

Figure 4-8. Stress-strain relationship of Mold Star 15 Slow silicone rubber from tension and compression tests. Linear-elastic and Neo-Hooke approximations are also presented. Inset: Bulk material specimens used in (left) compression and (right) tension tests.

ratio to avoid numerical stability issues that would arise from a purely incompressible material with infinite bulk modulus [132]. The 2D domain is meshed with plane-strain six-node modified hybrid quadratic elements (element type CPE6MH). Under large transverse compression, material self-contact is possible when the voids completely collapse. This behavior is incorporated in the finite element model by including a self-contact property, avoiding material interference.

In order to capture state transitions, dynamic numerical analyses are conducted using the implicit ABAQUS/Standard solver. The left-most edge of the module is fixed in space while the right-most edge is vertical displaced. Several combinations of transverse compression and vertical displacement paths are employed to reach the various configurations of a unit module. A small damping factor and slow displacement rates help enforce quasi-static conditions while capturing the locations of discrete state transitions. The force responses of interest are obtained by a summation of the vertical reaction forces (RF2) of the nodes on the right-hand-side boundary of the element, while strain energy is extracted from the ALLSE variable.

4.4 Results and discussion

4.4.1 Experimental results

As illustrated by the image shown in Figure 4-6(b) of a 3x1 arrangement of nominally identical units, each module may exhibit one of many possible configurations. Thus, to properly probe the full range of displacements under which each configuration is observed, cyclic loading is applied from the zero-displacement position in both directions, under a variety of initial conditions.

Figure 4-9 presents measurements of vertical reaction force, F_y, for a module with $d_1 = d_2 = 4.12$ mm under cyclic loading up to 6 mm in both directions for a transverse compression of $\frac{\delta_x}{w} = 0.18$..

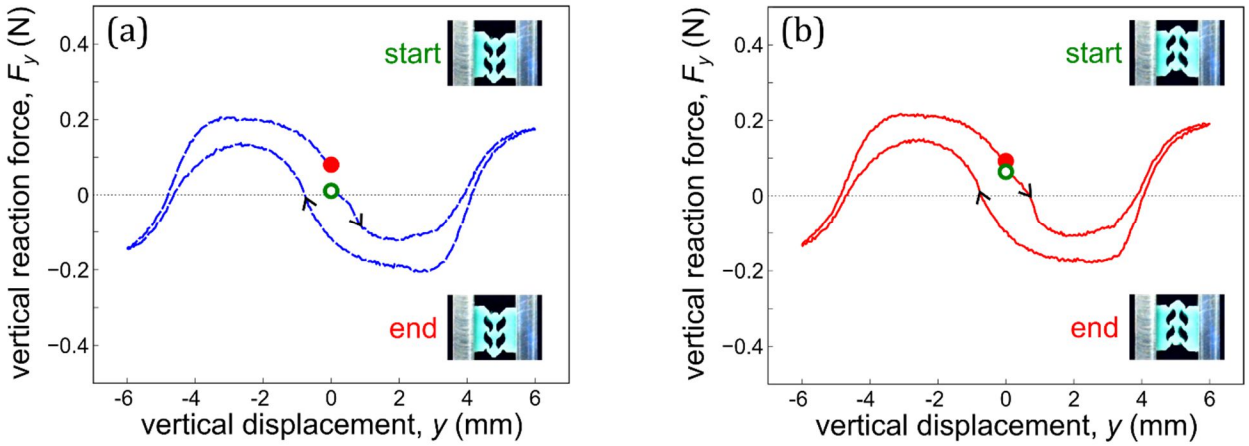

Figure 4-9. Force displacement results a full loading cycle when the module has an initial deformed configurations characterized by (a) voids pointed upwards and (b) voids pointed downwards. The final state is the same as the initial state in both instances.

Loading direction is indicated by the arrows and the starting and ending points are indicated by the hollow and filled circles, respectively. In Figure 4-9(a), the initial, final, and intermediate deformed shape of the module are characterized by the voids that point downwards, resulting in a downward translation of the central vertical member of the module with respect to the left and right edges. In Figure 4-9(b), the deformations are characterized by a symmetric configuration in which the voids are pointed in the upward direction. There is a large region of negative stiffness or negative slope around the zero-displacement position. Two positive stiffness regions are noted near the upper and lower limits of vertical displacement considered in these experiments.

When the initial configuration is characterized by voids that alternate between horizontally- and vertically-dominant shapes, half-cycle loading and unloading tests generate the responses presented in Figure 4-10. Only half cycles are considered since these response curves include a transition to the configurations shown in Figure 4-9. Hence, completion of the full cycle would simply replicate a portion of the prior results. Figure 4-10 (a) and (b) present results from tests where the initial configuration is characterized the upper left void that is deformed such that its major axis is in the

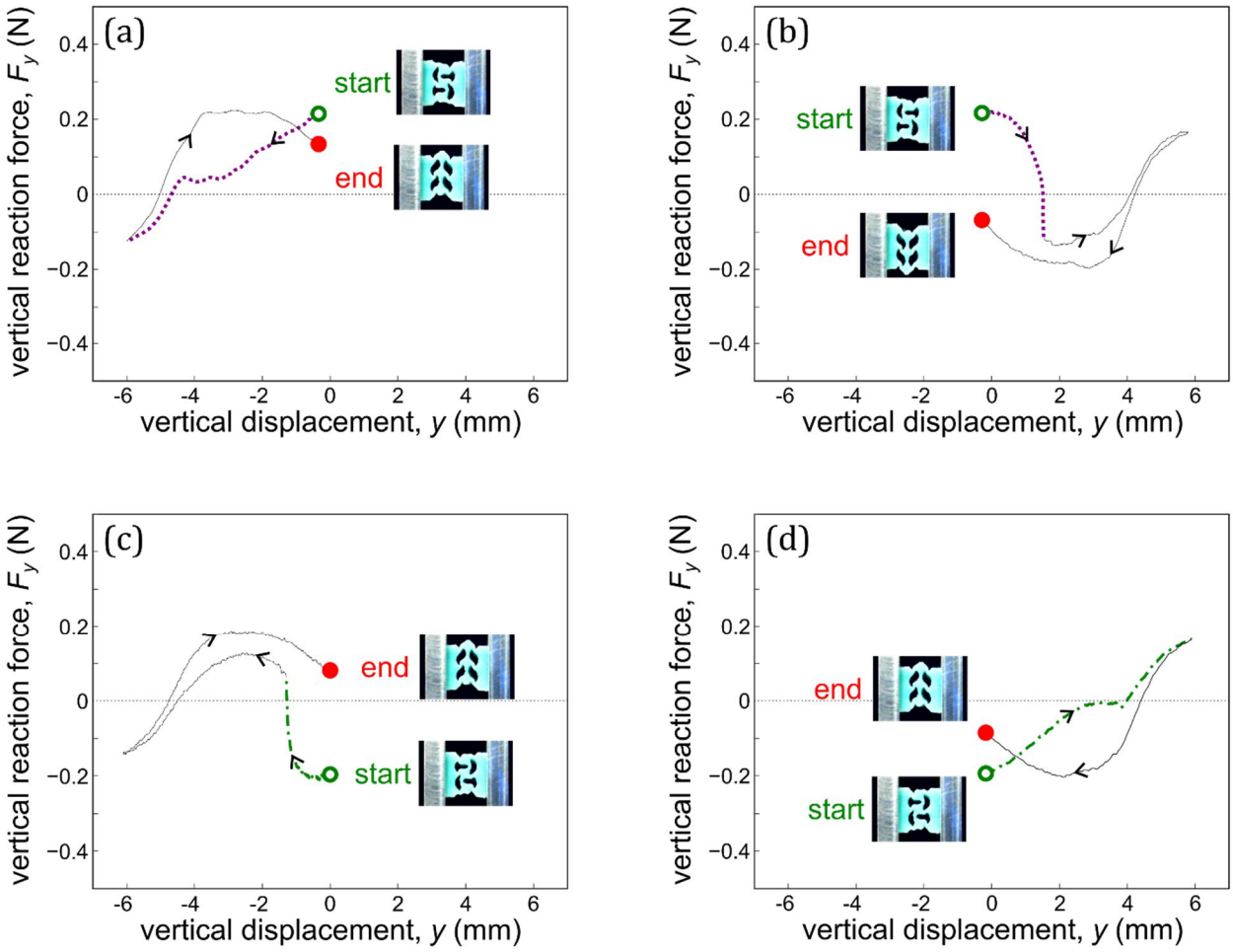

Figure 4-10. Responses from compression and extension tests where the initial configuration is characterized the upper left void deformed such that it is extended (a,b) vertically and (c,d) horizontally. These responses include transitions to configurations presented in Figure 4-9, and the final configurations are presented in each case. The thick curves represent the portions of the cycles in which the starting configuration is maintained, while the thin segments denote portions of the cycle following a transition to a different configuration.

vertical direction. On the other hand, Figure 4-10 (c) and (d) present results from tests where the initial configuration is characterized a horizontal shape of the upper left void. To probe the full extent of these configuration, loading cycles are initiated in both directions from the starting point. The segments of these tests highlighted by thick dotted and dash-dotted curves represent the portions in which the module retains the starting configuration. These segments are later aggregated (in Figure 4-11 and Figure 4-13) to show more comprehensive force response results under all observed configurations. On the other hand, the portions of the response shown by the thin black lines

correspond to segments where the configuration duplicates one of the paths shown in Figure 4-9, and are thus excluded from the aggregated results. One notable feature of the responses shown in Figure 4-10 is the discrete state transitions from the initial configuration. These are indicated by vertical segments of the force response that cross the horizontal axis, resulting in sudden changes to reaction force magnitude and direction.

4.4.2 Influence of transverse confinement on material response

Aggregated measurements of vertical reaction force, F_y, for a module with $d_1 = d_2 = 4.12$ mm are presented in Figure 4-11(a-c) for three different levels of transverse compression δ_x. The approach outlined in the prior section is adopted to aggregate the responses from several loading cycles for each compression level, to capture the full extent of the observed configurations. For example, the response shown in Figure 4-9 and Figure 4-10 are collected to generate the results shown in Figure 4-11(b).

Overall, reaction force magnitudes are greater with the increase of δ_x, which is intuitive based on larger local stresses associated with greater transverse compressions. Further, increased transverse compression results in larger hysteresis. The hysteresis is likely due to the onset of self-contact and friction as the voids collapse when subjected to the increased confinement, as suggested by the insets in Figure 4-11(a-c) and the results of Figure 4-3 and Figure 4-4. The four curves (solid, dashed, dotted, and dash-dotted) denote different deformed shapes, correspond to the segments of the same line styles shown in Figure 4-9 and Figure 4-10. The shaded regions around the zero-displacement positions highlight the range of displacements within which all four configurations are observed in experiments. This region is termed the *highly metastable range*, and the polygon labels in Figure 4-11(b) correspond to the distinct metastable states shown Figure 4-11(d,e) for the case of $y = 0$ and δ_x = 2.7 mm.

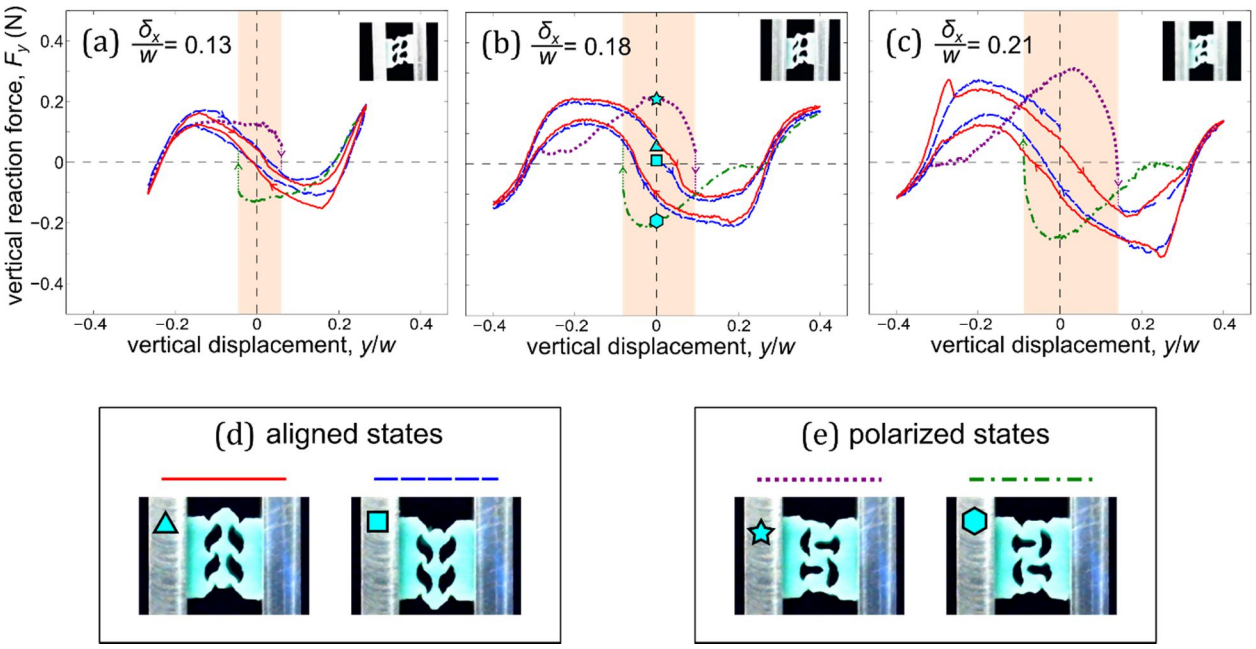

Figure 4-11. (a-c) Experimentally-measured vertical reaction force-displacement responses for three levels of transverse compression $\frac{\delta_x}{w}$ for a module with $d_1 = d_2 = 4.12\ mm$. Thin vertical dotted lines marked with arrows at the boundaries of the shaded *strongly metastable range* indicate discrete state transitions. Line styles correspond to the aligned and polarized topologies presented in (d) and (e).

The configurations are classified in two types according to the nature of the deformations. *Aligned* topologies are shown by solid and dashed curves, and denote deformations of the voids that are all aligned in the same direction. *Polarized* topologies, indicated by dotted and dash-dotted curves, are characterized by a rotation of the central segment, causing void deformations to alternate between horizontally- and vertically- dominant shapes.

The highly metastable ranges provide an opportunity to dramatically adapt stiffness and reaction force by switching between topologies while boundary conditions remain unchanged. Reaction force responses of the aligned configurations are characteristic of a bistable element, with a negative slope (i.e. negative stiffness) for a region surrounding vertical displacement y = 0, and positive slope or stiffness outside this region [96]. On the other hand, the polarized states exhibit near-zero stiffness in

the highly metastable range for $\frac{\delta_x}{w}$ = 0.13 and greater stiffness as transverse compression is increased. The shaded metastable regions in Figure 4-11(a-c) are bounded by vertical dotted lines marked with arrows indicating observed polarized-to-aligned state transitions that occur passively in consequence to global displacements exceed the highly metastable range. These transitions correspond to sudden changes in reaction force magnitude and direction. The ability to switch between configurations within the metastable range would similarly result in a sudden change in reaction force magnitude, representative of the conformational change representing the power stroke in muscle cross-bridges.

Finite element analyses establish a deeper understanding of these state-switching behaviors. In a procedure similar to the one pursued for the experimental investigations, cyclic simulations with slowly varying boundary conditions are undertaken from various starting positions. The aggregated results of reaction force are presented in Figure 4-12(a-c) showing trends that are comparable with the experimental results in Figure 4-11 for the three considered levels of transverse compression δ_x. The points highlighted in Figure 4-12(b) correspond to the aligned an polarized topologies in Figure 4-12(d,e), which are equivalent to the experimental results presented in Figure 4-11(d,e).

Crucially, finite element simulations facilitate an examination of system energies, which is not possible directly from the experimental force response results in the presence of sudden, dissipative state transitions [106]. The numerical results presented in Figure 4-12(f-h) reveal that strain energy levels increase with transverse compression, which is an expected result given that greater transverse compressions impart higher strains. Further, they reveal that the polarized configurations are at a higher energy level than the aligned topologies, and that polarized-to-aligned transitions are enabled by rapid releases of strain energy. The quantity of energy released in consequence to these transitions also increases with transverse compression.

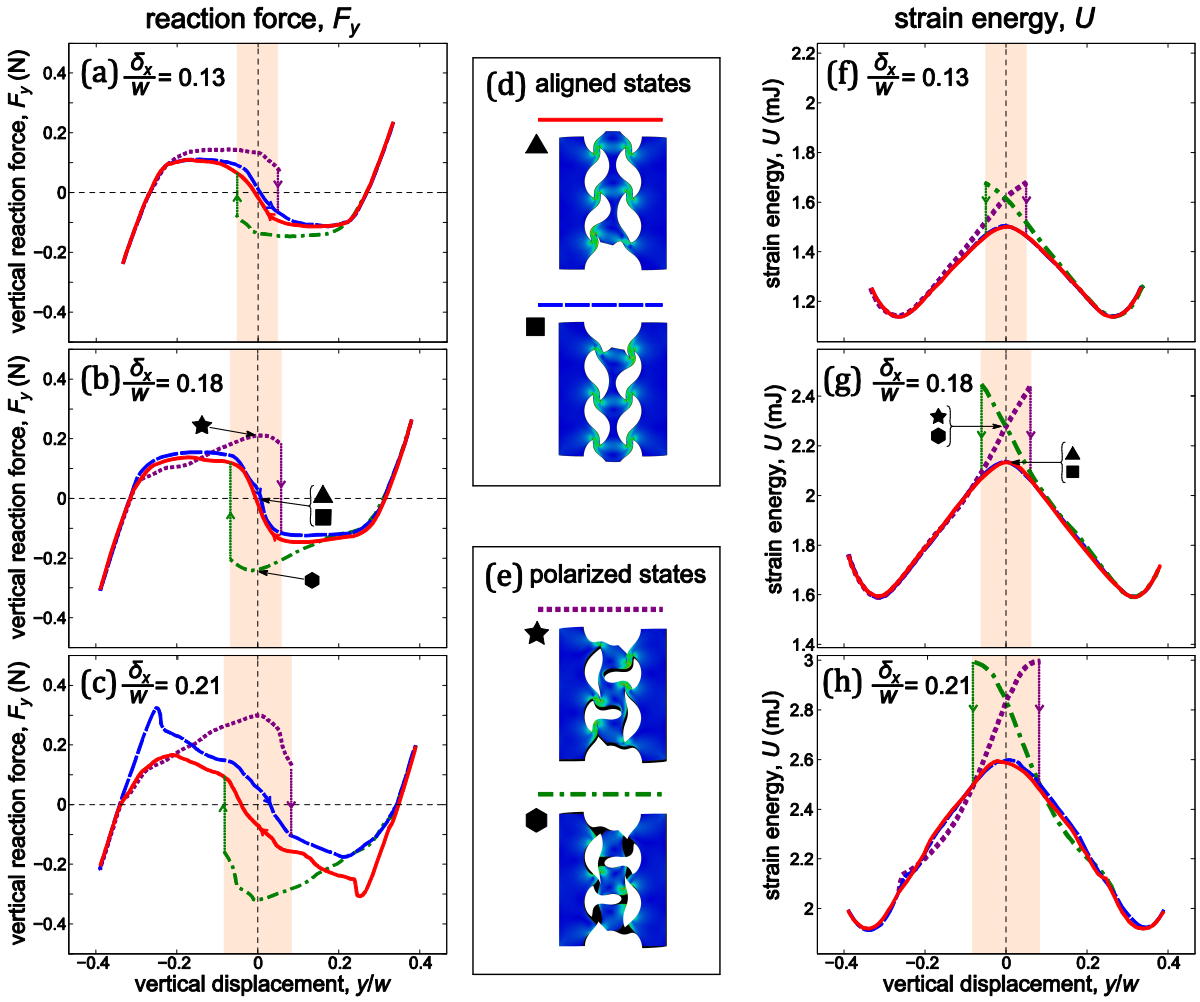

Figure 4-12. Numerical results of a module with uniform void geometry subject to oblique displacements under three different levels of transverse compression. (a-c) Trends in reaction force responses show reasonable agreement with the experimental results shown in Figure 4-11(a-c). (f-h) Strain energy curves reveal the large strain energies stored in the polarized states within the shaded highly metastable regions. (d,e) Images showing aligned and polarized topologies as predicted by the finite element model, with line styles corresponding to the curves in (a-c, f-h).

The variation in the number of available metastable configurations of the four-void unit as the boundary conditions are modulated shares some similarities with the recruitment of cross-bridges in activated muscle. For sarcomeres extended far beyond the natural length, there is reduced overlap between adjacent actin and myosin filaments, which reduces the likelihood of cross-bridge formation, [39] and hence the number of metastable configurations. The reduction in the number of cross-bridges available for recruitment also compromises the maximum possible active forces that sarcomeres can generate. Similarly, for sarcomere lengths much less than the natural elongation, thin

filaments may overlap, and the radial distance between the thick filament and thin filament may increase [4,39]. This can similarly compromise cross-bridge recruitment and force generation.

4.4.3 Influence of void geometry on material response

While varying transverse geometric confinements provides a means to tailor mechanical properties, certain behaviors may be programmed into the material itself by selection of geometric parameters. For instance, asymmetry can be introduced by varying void diameters d_1 and d_2 while keeping the wall thickness t separating the voids at fixed $t = 0.88$mm. An analytical approximation (see Section 4.5) suggests that such an approach may yield force and energy responses biased to one of the polarized configurations. Figure 4-13(a-c) present vertical force-displacement responses for units with (a) $d_1 = d_2$, and (b,c) $d_1 < d_2$. Corresponding numerical results for strain energy are shown in Figure 4-13(d-f). As the difference between diameters d_1 and d_2 grows, polarized states marked by dotted curves are observed for a larger range of vertical displacements, and are generally at a lower strain energy than those marked by dash-dotted curves. Thus, an asymmetry or bias is introduced towards polarized topologies characterized by vertically dominated deformed shapes of

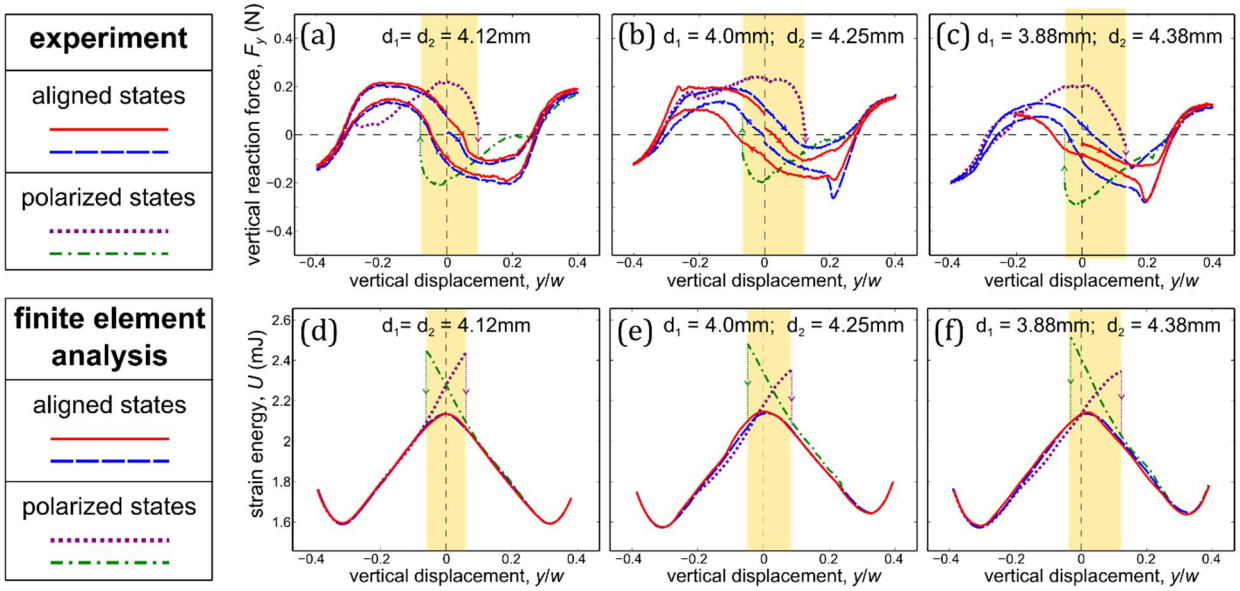

Figure 4-13. Force and energy responses of modules with non-uniform void diameters. (a-c) Experimental results showing vertical reaction force-displacement responses and (d-f) numerical results showing strain energies as void diameters d_1 and d_2 are varied, demonstrating a bias towards one of the polarized states as the difference between d_1 and d_2 increases. Void geometry also influences the locations and extents of the highly metastable range

the smaller voids. This bias also influences the extent of the shaded highly metastable ranges and the locations of the polarized- to-aligned state transitions, which suggests an opportunity to program and tune the hysteresis and mechanical response of these modular constituents by means of strategic selection of void geometries.

4.4.4 Programmable response

The results of Figure 4-13(a-c) show elements with varying ratios of diameters $\frac{d_2}{d_1}$, resulting in different metastable ranges in which the polarized configurations are observed, The arrangement of several modules with varying void geometry provides a means to program the mechanical response by prescribing the order in which these transitions will occur in consequence to global shear motions. The results of Figure 4-14 illustrate how a section of the material composed of multiple modules with different void geometries can yield a programmable response under global shear. The uppermost element has $d_1 = d_2$, the central module has $d_1 = 0.9\, d_2$, and the lower module has $d_1 = 0.8\, d_2$.

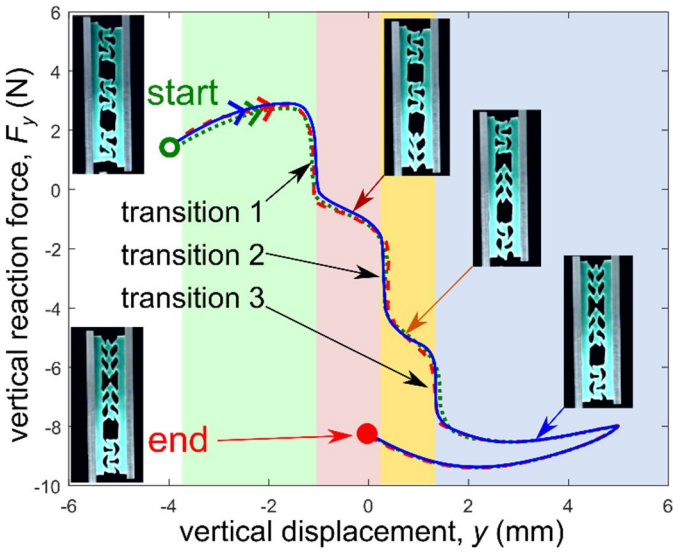

Figure 4-14. Programmable response in an arrangement of modules with different void geometries. The upper modules has $d_1 = d_2$, the central module has $d_1 = 0.9\, d_2$, while the lower module has $d_1 = 0.8\, d_2$. If the initial configuration is such that all three modules are the polarized state characterized by a vertical shape of the upper left void, prescribing shear motions will result in different thresholds for which sudden polarized-to-aligned transitions occur. These transitions are indicated by vertical jumps in reaction force. Results from three trials are presented, indicating repeatability.

Overall material dimensions are twice those of the prior section, facilitating easier manual adjustment of initial topologies. All three elements are initially in the polarized configuration characterized by a vertical shape of the upper left void. However, due to the varying bias introduced by the void geometry, the polarized states suddenly jump to aligned topologies at three different levels of shear. First, the module with greatest experiences this transition, followed by the central module, and then the symmetric element at the top of the material section. The regions for which the different combinations of configurations are observed are shaded. Results from three experiments are presented, indicated repeatability of the observed phenomena.

4.5 Analytical approximation using Euler's elastica

Examination of the central horizontal member of a unit module under transverse confinement, as shown in Figure 4-15(a), suggests that the deformation of this member may be approximated by large-scale deformations of an elastic beam clamped at both ends, providing some insight into the coexistent metastable configurations of the module. Enforcement of a nonzero clamp angle β, as shown in Figure 4-15(b), reflects conditions of unequal void diameters in the module. To further develop the elastica model as a meaningful prediction of trends in the material module's force and strain energy responses, elastic curve solutions are presented for the parameters and boundary conditions described in Figure 4-15(c). A flexible beam with length L, Young's modulus E, second moment of inertia I, is clamped at both ends at an angle β with respect to the horizontal. The two

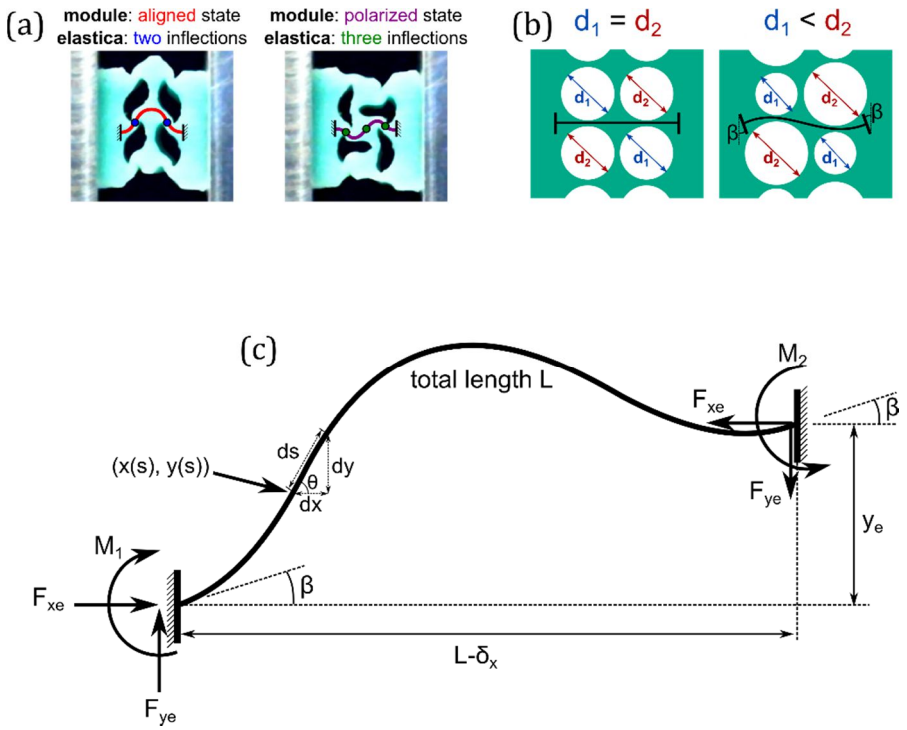

Figure 4-15. (a) Unit module highlighting deformations of central horizontal member in polarized and aligned deformed topologies. (b) A nonzero clamp angle β reflects the geometry of a module with unequal void diameters. (c). Schematic of a flexible beam with boundaries clamped at an angle β. Insets show photographs of a unit module, highlighting the deformations of the central horizontal member and motivating their approximation by an elastic beam under large deformations with parameters as shown.

clamped ends are separated by a horizontal distance of $L - \delta_x$ and a vertical distance of y_e, respectively. Here, the method developed by Shoup and McLarnan [133] is adopted, and further details are presented in Appendix D. The equations that result from this solution approach are solved using the built-in MATLAB function *fsolve* to yield solutions for the five unknowns. Since *fsolve* employs iterative solvers, suitable initial estimates must be provided. Appropriate initial guesses are employed to obtain elastica curves with the desired number of inflection points and concavities at the clamped ends [133] corresponding to the aligned and polarized topologies presented in Figure 4-15(a). Then, the solutions are used to compute the bending strain energy in the beam

Nondimensionalized vertical reaction force and strain energy plots of the elastica model are presented in Figure 4-16(a-c) and (d-f), respectively, showing solutions with different numbers of inflection points. The bias observed in Figure 4-13(b,c) and (e,f) for material modules with $d_1 \neq d_2$ is accounted for in the elastica model by prescribing a nonzero clamp angle β at both ends, which predisposes the beam towards certain elastic curve solutions. The simple elastica model provides some insight into the force responses and strain energies of the different topologies of a unit module. Forces responses show a clear negative stiffness region for the two-inflection solutions that represent the aligned topologies. As presented in Figure 4-16 (e,f), the elastic curve solutions with three inflection points, which are an analogue to the polarized states of the module, are at a higher strain energy level than the two-inflection solutions.

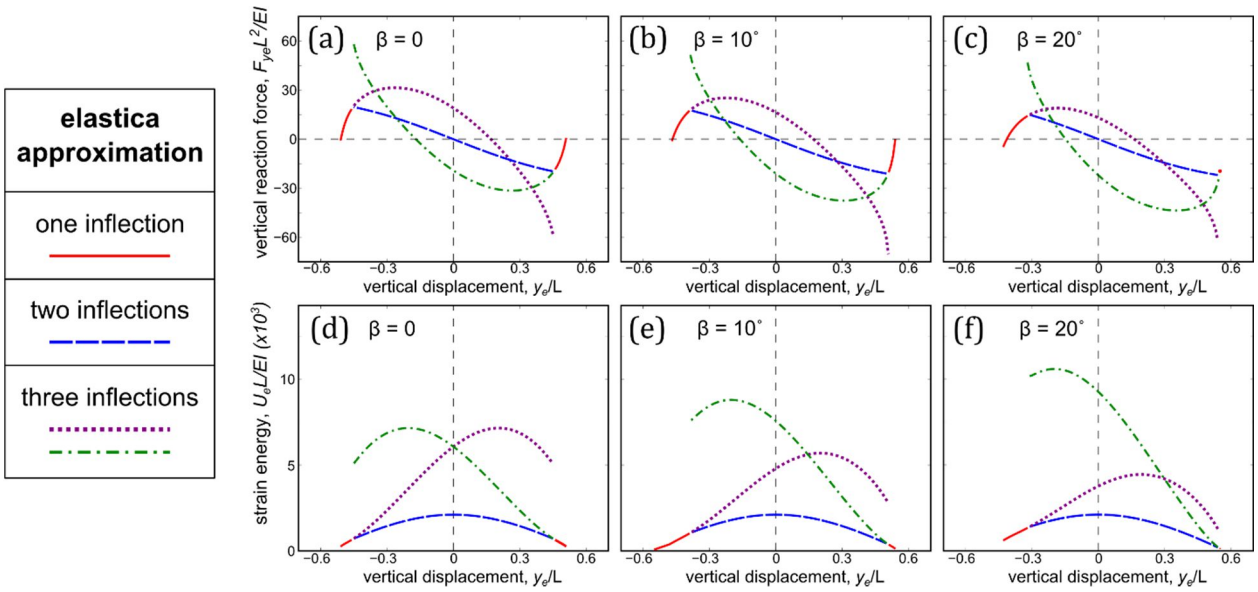

Figure 4-16. Nondimensionalized (a-c) reaction force and (d-f) strain energy for the clamped elastica, with bias reflected by introducing a nonzero clamp angle β. Numerical results and the elastica model show that the polarized or three-inflection states are at higher strain energy levels than the aligned or two-inflection states

The influence of bias is clearly noted, and the difference between the strain energies of the three-inflection solutions grows as the clamp angle is increased. Stability of the elastica solutions is not considered, and the assumption of inextensibility in the elastica model and the absence of intersecting vertical members leads to an over-prediction of the range in which polarized (three-inflection) states are observed. Nevertheless, key features such as the negative stiffness region in the aligned configurations, higher strain energy in the polarized states, and discrete changes in strain energy level during transitions from polarized states are reflected in the behaviors of a clamped elastic beam, providing perhaps a first approximation to the module response as key geometric parameters are varied, This is especially useful given the relative computational complexity required to solve the elastica model compared to the finite element model. The equations describing the elastic curve solutions can be solved numerically within seconds, while each cycle of the finite element model constructed in ABAQUS can take upwards of one hour on a PC with a Core i7 processor and 16GB of installed RAM. Furthermore, the finite element model requires careful tuning of initial transverse compression and vertical displacement values for each variation of module geometry to

probe all the configurations. On the other hand, solutions corresponding to different selection points of the elastica model are obtained by following simple, intuitive guidelines governing initial guesses for the segment angles at each boundary [133]. These characteristics could make the elastica approximation a valuable design tool for the development of architected material systems composed of large numbers of modules with varying geometries.

Models employing flexible beams to explain muscle's microscale features have been previously explored by physiologists as a means to visualize and understand the apparent stability of sarcomeres in the negative stiffness 'descending limb' [10,39]. An example is presented in Figure 4-17, where Allinger et al. [32] express bound cross-bridges by contact between bristles that extend from rigid bars representing the actin and myosin filaments. As the length is increased, the number of bristles available for contact decreases, which reduces the maximum possible forces F that can

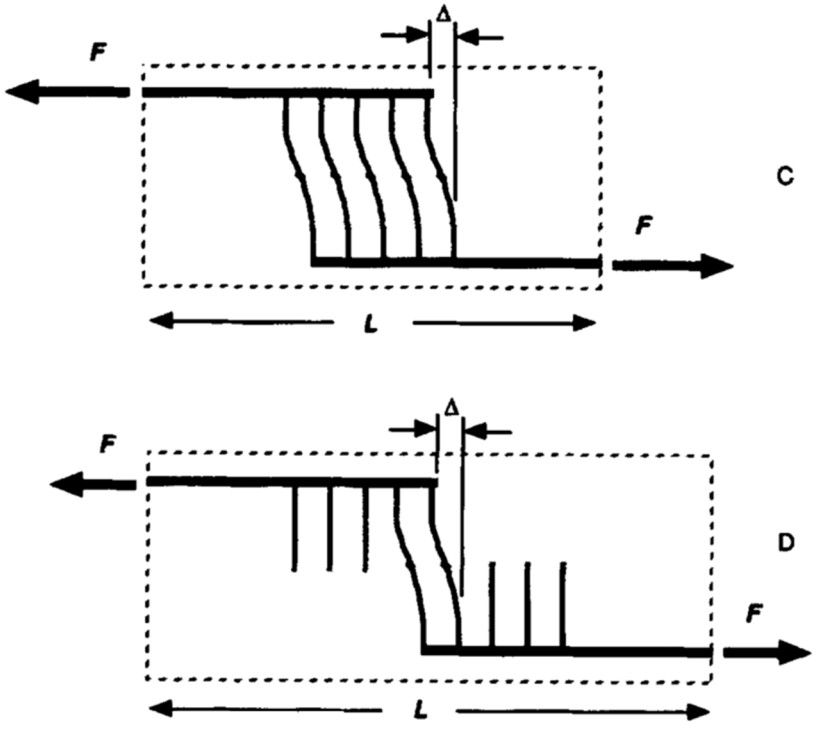

Figure 4-17. Model proposed by Allinger et al [32] to explain sarcomere stability in the descending limb. Cross-bridge recruitment is illustrated by contact between flexible 'bristles' extending from both filaments. Image reproduced from [32] with written permission from the publisher.

supported by the sarcomere for this given length but ensures a local positive stiffness. While the connected bristles are intended to represent cross-bridges, the model does not account for the conformational changes in cross-bridges that result in force generation or passive tension recovery. Such conformational changes could be accounted for by different post-buckled configurations of the four-void unit module or the elastica approximation to the central horizontal member presented in this chapter.

4.6 Conclusions

Inspired by the geometry and architecture of skeletal muscle constituents, and by local conformation changes in microscale elements that serve as the origin for macroscopic force-generation and length change in muscle, the research presented in this chapter illustrates the potential to create novel, advanced architected material systems that gives rise to intriguing material response not revealed by previous work. Multiple *metastable* configurations are uncovered for prescribed boundary conditions, which demonstrates means to drastically adapt stiffness, reaction force, and stored strain energy in the material system when subjected to unchanging boundary conditions. Oblique, shear-like loads, representative of pennate muscle movements and the sliding motions between adjacent actin and myosin filaments during sarcomere length change, give rise to energy-releasing state transitions that cause discrete changes in reaction force magnitude and direction. These behaviors may be tailored by varying the level of transverse confinement, while biases to certain configurations arise when void diameters are non-uniform. A model of module deformations is developed using Euler's elastica, allowing for insight to be obtained from a simplified analogue of the complex architected material behavior.

Consideration of a section the proposed architected material composed of several constituents units in parallel would greatly enhance the properties adaptivity presented here, since their combined response would arise from a superposition of the individual module responses [76]. By introducing a material architecture that leverages the coexistence of multiple locally stable configurations and discrete energy-releasing state transitions, this research offers the potential to achieve mechanical properties and functionalities previously unexplored.

Chapter 5.
Summary and conclusions

5.1 Summary of contributions

This dissertation investigates concepts for structural and material systems inspired by the architecture of skeletal muscle's constituents, and specifically by its ability to exploit *metastability* in conjunction with *conformational changes* or buckling to achieve novel system responses. These features are explored both in a static and dynamic context, revealing large adaptation in energy dissipation properties, the capture and storage of energy in high-potential configurations and subsequent release for efficient actuation and deployment, and the ability to tailor mechanical properties along a desired axis by tailoring transverse geometries.

- The first major contribution of this thesis is a thorough understanding of the dynamic response of a fundamental, one-dimensional metastable element. Investigations uncover several, qualitatively distinct, dynamic regimes in response to harmonic excitation near resonance. These distinct regimes are exploited to achieve highly adaptable energy dissipation characteristics that vary by up to two orders of magnitude. While large variation in dynamic response and energy dissipation are observed among regimes, the introduction of a static offset or asymmetry results in continuously tunable energy dissipation performance.

- Second, this dissertation develops and investigates structures composed of asymmetrically bistable constituents for energy capture, storage, and release. Outcomes reveal the key role of energetic asymmetry on the ability of multistable system to capture and store the energy from impulsive excitations in higher-energy stable states. Investigations on the influences of various system parameters uncover a balance between energy storage performance – measured by the fraction of initial kinetic energy trapped as recoverable potential energy – and the risk of compromised performance due to unwanted transitions back to the low-energy states. In multistable systems with stored elastic energy, it is shown that consideration of system dynamics and the conversion of potential to kinetic energy may facilitate deployment with a lower energy cost than what is required under quasi-static conditions.
- Evoking the shear-like motions of adjacent filaments and cross-bridge conformational changes during muscle contraction, this thesis explores how transverse influences can be exploited to adapt and tune the mechanical response in a desired direction. Through development, fabrication, and analysis, this thesis presents an architected material system capable of tailorable discrete, rapid changes in reaction force amplitude and direction. Numerical investigations reveal that these conformation changes coincide with sudden releases of strain energy.
- A few analytical or semi-analytical tools are presented in this dissertation. The first is a one-term harmonic balance method used to approximate the steady-state harmonic response of the one-dimensional metastable unit in Chapter 2. This allows for a prediction of the dynamic responses in different intrawell and snap-through regimes. Second, a semi-analytical approach employs Jacobi elliptic functions to predict the onset of snap-through, and hence energy trapping, of asymmetrically bistable units under transient, impulsive excitations in Chapter 3. Lastly, noting that the central horizontal member of a unit module presented in

Chapter 4 exhibits different numbers of inflection points in its various configurations, this element is modeled as a segment of Euler's elastica, offering prediction of the relative strain energies and reaction forces of these configurations.

5.2 Broader impacts and opportunities for future research

This dissertation leverages key features of the microscale assembly and functionality of skeletal muscle's constituents for structural and material systems with unique responses. The outcomes of this thesis reveal the potential to develop dampers and absorbers with large and adaptable energy dissipation capabilities, which could be useful in engineered systems that require variation in dissipative characteristics depending on operating conditions. For example, a system may ordinarily call for low dissipation to effectively transmit vibrational signals for structural health monitoring, but require greater dissipation in the face of larger excitations [98]. Insights gained from investigations on the energy capture in asymmetrically multistable structures could foster the development of actuators that effectively capture, store, and release energy, as well as adaptive, robust, and reusable armors and protective devices.

5.2.1 Active configuration changes and system dynamics

A major theme of this thesis is the static and dynamic properties adaptivity that is enabled by switching between different configurations or topologies. However, the system properties explored in this thesis are largely *passive* in nature. With the exception of Section 3.6, no *active* properties employing local actuation capabilities are considered or discussed. Skeletal muscle is a multifunctional system finely tuned for effective energy conversion and release for robust force-generation and shape change. While the passive features such as energy absorption and tension recovery are critical to muscle performance, tetanized muscle is fundamentally an active system with the flow of chemical energy governed by an integrated feedback mechanism. Due to this constant

energy flow, it is sometimes undesirable to study or describe muscle behaviors in terms of static or fixed *energy landscapes* [35], despite such a description offering useful insight into certain muscle behaviors [54]. With that in mind, there are broad opportunities to further enhance the work presented in this dissertation by considering a combination of active and passive features.

One such opportunity is the integration of the features described in this thesis within the framework of *binary robotics* [71,134,135], where actuators operate in discrete steps governed by the passive constraints by the underlying mechanical architecture of the actuator. The advantage of these actuators is that discrete positioning is possible without the need for low-end feedback control [136]. These discrete positions generally correspond to local minima of energy with respect to the coordinates that describe the actuators' motions. The results of Chapter 3 of this thesis can help improve the efficiency of such binary robotics systems in situations where these systems are acted upon by external loads, allowing the energy from these loads to be captured and stored, and later exploited when needed to reconfigure the system as desired. Further, as described in the latter half of Chapter 3, consideration of these configuration changes as dynamic rather than quasi-static processes may greatly enhance opportunities to leverage stored energies for reconfiguration. Oftentimes, the reconfiguration of deployable and multistable systems is considered quasi-statically [137–139]. On the other hand, dynamic configuration changes may not smoothly follow the energy landscapes derived under these static conditions. When system dynamics are considered, it is insufficient to consider simply the sequence of actuator inputs to deploy bistable links. The timing and magnitude of these inputs must also be taken into account due to the transient dynamic responses that may arise. Obtaining energy-optimal or time-optimal inputs that may give rise to these configuration changes is not trivial. Such a problem may require the integration of optimal control routines that explicitly consider actuator capabilities and power requirements [140].

A current limitation of binary actuator systems are the fixed parameters of the discrete positions that can be maintained without energy input. Depending on application requirements, these desired

positions may be required to vary over time, but introducing additional binary mechanisms to permit a modulation of this geometry would introduce significant complexity. Incorporation of transverse geometries, as in Chapter 4 of this thesis, may offer a solution to overcome this limitation by providing means to tailor the location of the actuator's stable configurations. By embedding the intelligence of the system within its structure and geometry, algorithms to control positioning do not need to rely on accurate feedback. Consideration of ways in which discrete configuration changes can be used to generate programmable movements and motions of soft material systems could foster the development of robust soft robots. In order to actively generate these configuration changes, several actuation methods can be explored, including pneumatic or fluidic methods [141,142] or using incorporating ferromagnetic elements that can cause portions of the material system to react to changes in magnetic fields [143].

5.2.2 Emerging design, manufacturing, and analysis methods

While the first set of broad opportunities for future work incorporate an extension from passive to active behaviors, the second set of recommendations for future work describe possible approaches to enhance the manufacturability and scalability of engineered structural and materials systems described in this thesis. While binary robotics systems share similarities with digital electronics, the former are currently limited to a small number of states due to present manufacturing constraints [71]. Concepts for large-scale systems incorporating binary actuation with muscle-like feedback control have been explored numerically [74], and may be extended to explicitly account for energetic asymmetries through methods often employed in stochastic and molecular dynamics simulations that consider biases or unequal energy barriers [25,144]. Given the pace of innovation in additive manufacturing technologies, such systems may become physically realizable in the near future.

There are a number of ways in which structural and material systems can be designed to give rise to the phenomena studied in this dissertation. The experimental systems explored in this thesis are

developed primarily to facilitate investigations of the relevant system properties, and are composed of elementary units such beams, linkages, springs, and relatively simple elastomer units. On the other hand, application of these features in actuators and robotics, protective devices, and deployable can greatly benefit from advances in 3D printing and additive manufacturing. As these technologies continue to improve, there will be increasing opportunities to design and fabricate complex geometries from a variety of materials that exhibit higher durability, lower damping, and greater toughness than available today [145–147]. Origami-based structures and mechanisms provide another great opportunity for the the manufacture and analysis of systems exhibiting many properties described in this research. Origami structures have been shown to exhibit bistability, tailorable stiffness, and reconfigurability [141,148,149]. The integration of the novel concepts for structural and material systems explored in this dissertation with emerging design and fabrication paradigms offers vast possibilities for advanced muscle-inspired engineered systems that strategically exploit a multitude of stable configurations and transitions between them for a variety of applications.

Appendices

Appendix A.
Harmonic balance solution to steady-state dynamics of a metastable module excited near resonance

Consider a single-degree-of-freedom system governed by:

$$m\ddot{x} + b\dot{x} + k_1 x + k_2 x^2 + k_3 x^3 - k_L(z + d - x) = 0 \quad \text{(A-1)}$$

where m is the lumped internal mass, b is the damping coefficient, and k_1, k_2, k_3 are the linear, quadratic, and cubic stiffness coefficients, respectively. z is a harmonic excitation with static offset d that is coupled to the inertia by a linear spring with stiffness k_L. The solution to Eq. (A-1) is approximated using a fundamental Fourier series expansion:

$$x(t) = f(t) + g(t)\sin(\omega t) + h(t)\cos(\omega t) \quad \text{(A-2)}$$

where the coefficients f, g, and h are assumed to slowly vary in time with respect to the primary period of oscillation. The excitation z considered here is a harmonic in frequency ω and amplitude z_0:

$$z(t) = z_0\cos(\omega t) \quad \text{(A-3)}$$

Substituting Eqs. (A-2) and (A-3) into (A-1), assuming slowly varying harmonic coefficients such that $\ddot{f}(t) = \ddot{g}(t) = \ddot{h}(t) = 0$, and retaining only those harmonic terms proportional to the assumed solution expansion, the following equations are obtained via balancing the coefficients of the constant, sine, and cosine terms respectively.

$$-b\dot{f} = k_1 f + k_2 f^2 + \frac{k_2}{2} r^2 + k_3 \left(\frac{3}{2} f r^2 + f^3\right) + k_L (f - d) \tag{A-4a}$$

$$2m\omega\dot{h} - b\dot{g} = k_1 g + 2k_2 gf + k_3 \left(\frac{3}{4} g r^2 + 3gf^2\right) + k_L g - mg\omega^2 - bh\omega \tag{A-4b}$$

$$-2m\omega\dot{g} - b\dot{h} = k_1 h + 2k_2 hf + k_3 \left(\frac{3}{4} h r^2 + 3hf^2\right) + k_L h - k_L z_0 - mh\omega^2 + bg\omega \tag{A-4c}$$

The amplitude of the motion of x is expressed by $r = [g^2 + h^2]^{1/2}$. Assuming steady-state response, which implies that $\dot{f}(t) = \dot{g}(t) = \dot{h}(t) = 0$, Eqs. (A-4 a,b,c) are combined to yield a system of two equations for r and f, representing response amplitude and offset, respectively.

$$k_3 f^3 + k_2 f^2 + \left(k_1 + k_L + \frac{3}{2} k_3 r^2\right) f + \frac{1}{2} k_2 r^2 - d k_L = 0 \tag{A-5a}$$

$$\frac{9}{16} k_3 r^6 + \frac{3}{2} k_3 (-m\omega^2 + k_1 + k_L + 3k_3 f^2 + 2k_2 f) r^4$$

$$+ [(-m\omega^2 + k_1 + k_L + 3k_3 f^2 + 2k_2 f)^2 + b^2\omega^2] r^2 - k_L^2 z_0^2 = 0 \tag{A-5b}$$

The Eqs. (A-5a,b) are nonlinearly coupled and must be solved numerically, although the solutions are an analytical approximation to the steady-state dynamics of the metastable module. The solutions must then be evaluated for stability. From Eq. (A-4b,c), the response coefficients may be expressed using

$$g = -\frac{b k_L z_0 \omega}{\Gamma^2 + b^2\omega^2} \tag{A-6a}$$

$$h = -\frac{k_L z_0}{\Gamma^2 + b^2\omega^2} \tag{A-6b}$$

where

$$\Gamma = k_1 + 2k_2 f - m\omega^2 + k_3\left(3f^2 + \frac{3}{4}r^2\right) + k_L \tag{A-7}$$

Eq. (A-4) is then expressed in a conventional form using $\mathbf{x} = [f, g, h]^T$

$$\mathbf{Q}\dot{\mathbf{x}} = \mathbf{P}(\mathbf{x}) \tag{A-8}$$

where **Q** and **P** are determined by consideration of Eq. (A-4). Then, linearizing the system around one of the fixed points $\mathbf{x}^* = [f, g, h]^T$ obtained from solving Eqs. (A-5) and (A-6), the stability of the fixed point is found by evaluating the eigenvalues of the Jacobian matrix of the linearized system, where the Jacobian is $\mathbf{J} = \mathbf{D}_{\mathbf{x}}\left(\mathbf{Q}^{-1}\mathbf{P}(\mathbf{x})\right)_{\mathbf{x}^*}$. The fixed point solution is stable if all eigenvalues of the Jacobian have negative real parts.

Appendix B.

Semi-analytical solution to the transient response of an asymmetric bistable Duffing oscillator

This section presents a semi-analytical solution for the transient dynamics of an asymmetric bistable Duffing oscillator to determine the final snap-through and predict the equilibrium state to which the system eventually settles. The results are based upon and extend those presented by Zhang et al. [114]. Consider a single-degree-of-freedom system governed by:

$$\ddot{x} + \eta\dot{x} + \alpha x + \beta x^2 + \gamma x^3 = 0 \tag{B-1}$$

with $\eta > 0, \alpha < 0$, and $\gamma > 0$. In order to eliminate the quadratic stiffness β causing the asymmetry, the system is approximated by two different, symmetric bistable Duffing oscillators, each approximating the behavior of the original system in one of the two potential wells.

$$\ddot{x} + \eta\dot{x} + \alpha_1 x + \gamma_1 x^3 = 0;\ x \leq 0 \tag{B-2a}$$

$$\ddot{x} + \eta\dot{x} + \alpha_2 x + \gamma_2 x^3 = 0;\ x > 0 \tag{B-2b}$$

The stiffnesses $\alpha_1, \gamma_1, \alpha_2$, and γ_2 are obtained from a least-squares regression of the asymmetrically bistable spring reaction force in Eq. (B-1). Given initial displacement and velocity x_0 and $\dot{x}_0$, the initial energy of the system is:

$$E_0 = \frac{1}{2}\dot{x}_0^2 + \frac{1}{2}\alpha_i x_0^2 + \frac{1}{4}\gamma_i x_0^4 \tag{B-3}$$

where $i = 1$ if $x \leq 0$ and $i = 2$ otherwise. If $E_0 > 0$, the initial oscillatory response is interwell, or snap-through, and is assumed to take the form:

$$x = C_1(t)cn(u_1, k_1);\ x \leq 0 \tag{B-4a}$$

$$x = C_2(t)cn(u_2, k_2);\ x > 0 \tag{B-4b}$$

$C_i(t)$ is the time-varying snap-through vibration amplitude, and u_i and k_i are the argument and modulus, respectively, of the cn Jacobian elliptic function. To compute initial amplitude and phase, the undamped case ($\eta = 0$) is first considered, hence the oscillation amplitude $C_i(t) = C_{i0}$ and modulus k_i are constants, and the argument u_i is:

$$u_i = \omega_i t + \phi_{i0} \tag{B-5}$$

where ω_i is a constant parameter and ϕ_{i0} is the initial argument determined by initial conditions. Substituting Eq. (B-4) and its time derivatives into Eq. (B-2) yields the following:

$$\omega_i^2 = \gamma_i C_{i0} \tag{B-6a}$$

$$k_i^2 = \frac{\gamma_i C_{i0}^2}{2(\gamma C_{i0} + \alpha)} \tag{B-6b}$$

The Jacobian elliptic functions require k_i to be constrained such that $0 \leq k_i \leq 1$, which leads to the following condition:

$$0 \leq -\frac{\alpha_i}{\gamma_i C_{io}^2} \leq \frac{1}{2} \tag{B-7}$$

Eqs. (B-2) and (B-6) are combined with the elliptic function identities $sn^2(u,k) + dn^2(u,k) = 1$ and $k^2 sn^2(u,k) + dn^2(u,k) = 1$ to yield the following expressions for initial amplitude, phase, and system energy:

$$C_{io} = \left(\frac{\left(-\alpha_i + \left(\left(\alpha_i + \gamma_i x_o^2 \right)^2 + 2\gamma_i \dot{x}_0^2 \right) \right)^{\frac{1}{2}}}{\gamma_i} \right)^{\frac{1}{2}} \tag{B-8a}$$

$$sn(\psi_{i0}, k_i)\frac{dn(\psi_{i0},k_i)}{cn(\psi_{i0},k_i)} = -\frac{\dot{x}_0}{\omega_i x_0} \tag{B-8b}$$

$$E_0 = \frac{1}{4}C_{io}^2\left(2\alpha_i + \gamma_i C_{io}^2\right) \tag{B-8c}$$

Hence, $C_{io}^2 > -\frac{2\alpha_i}{\gamma_i}$ must be satisfied to ensure $E_0 > 0$, which is the condition under which snap-through oscillations are observed for the undamped case. If damping is present in the system, system energy will satisfy $E(t) \leq E_0$ for all $t \geq t_0$, so if the above condition on initial oscillation amplitude is not met, no snap-through events are predicted and oscillations remain confined to the local potential well. Following the solution approach for the snap-through, transient response of a symmetric bistable Duffing oscillator [114], and letting C_i, ω_i, u_i, and k_i vary with time, the following expression is obtained for the snap-through oscillation amplitude $C_i(t)$ and argument $u_i(t)$

$$C_i(t) = \left[\left(\gamma_i^2 C_0^4 + \frac{a}{b}\alpha_i^2\right)e^{-4b\eta_i t} - \frac{a}{b}\alpha_i^2\right]^{\frac{1}{4}}\gamma_i^{\frac{1}{2}} \tag{B-9a}$$

$$u_i(t) = 4K_i\psi_i \tag{B-9b}$$

where the coefficients $a = -0.78592$ and $b = 0.32051$ are parameters from a polynomial fit to permit an approximation of $\int \dot{C}_i(t)dt$ over an oscillation period, C_0 is the initial amplitude, and $K_i = K_i(k_i)$ is the complete elliptic integral of the first kind. By averaging over one period $4K_i$, the parameter ψ_i is approximated by

$$\psi_i(t) \cong \frac{\phi_{i0}}{4K_i} + \int_{t_0}^{t}\frac{\omega_i}{4K_i}dt \tag{B-10}$$

and the instantaneous displacement $x_i(t)$ may be computed according to Eq. (B-4). Recalling that the system will not undergo further snap-through oscillations for $C_i(t)^2 \leq -\frac{2\alpha_i}{\gamma_i}$, the time at which point snap-through oscillations are no longer predicted is found by solving for t in (B-9a) as:

$$t_{end} = -\ln\left[\frac{\left(4+\frac{a}{b}\right)\alpha_i^2}{\left(\gamma_i^2 C_{i0}^4 + \frac{\alpha_i^2 a}{b}\right)}\right]/4b\eta_i \tag{B-11}$$

The system switches between Eqs. (B-4a) and (B-4b) each time a snap-through event occurs at $x(t_{snap}) = 0$. If $t_{end} > t_{snap}$, a new initial amplitude is found based on the parameters of the new local potential well as

$$C_{j0} = \left[\frac{\left(-\alpha_j + \left(\alpha_j^2 + 2\gamma_j \dot{x}_{snap}^2 \right) \right)^{\frac{1}{2}}}{\gamma_j} \right]^{\frac{1}{2}} \tag{B-12}$$

where $\dot{x}_{snap}$ is the velocity at time t_{snap}, and $j = 1$ for $\dot{x}_{snap} < 0$ and $j = 2$ for $\dot{x}_{snap} > 0$. Setting $t_0 = t_{snap}$, the procedure outlined in Eqs. (B-9 – B-12) is the repeated until $t_{end} < t_{snap}$, which is the condition that indicates that the final snap-through event has occurred and any further oscillations will remain confined to the local potential well as local intrawell oscillations.

Appendix C.
Approximation to module deformation using Euler's elastica

This section presents a solution to the elastica curves approximating the deformation of the central horizontal member of a single module considered in Chapter 4, and an expression for the bending strain energy stored in the beam. The method developed by Shoup and McLarnan [133] is adopted here.

The differential equation describing the curvature of an Euler-Bernoulli beam at any arbitrary point along the beam is [133,152]:

$$EI\frac{d\theta}{ds} = M(s) \tag{C-1}$$

where $M(s)$ is moment required for static equilibrium at $(x(s), y(s))$. Equating moments about this arbitrary point and differentiating with respect to s yields:

$$EI\frac{d\theta}{ds} = M_1 - F_{xe}\,y + F_{ye}\,x \tag{C-2}$$

$$EI\frac{d^2\theta}{ds^2} = -F_{xe}\frac{dy}{ds} + F_{ye}\frac{dx}{ds} \tag{C-3}$$

Noting that $\frac{dy}{ds} = \sin(\theta)$, and $\frac{dx}{ds} = \cos(\theta)$, the overall length of the elastica and the geometry of the boundary points can be expressed as:

$$\int_0^{S^*} ds = L \tag{C-4a}$$

$$\int_0^{S^*} \cos(\theta)\, ds = L - \delta_x \tag{C-4b}$$

$$\int_0^{S*} \sin(\theta)\, ds = y_e \tag{C-4c}$$

In order to make use of these conditions, Eq. (C-3) is first rewritten and integrated with respect to θ.

$$\int EI \frac{d^2\theta}{ds^2}\, d\theta = -F_{xe} \int \sin(\theta)\, d\theta + F_{ye} \int \cos(\theta)\, d\theta \tag{C-5}$$

$$\frac{1}{2} EI \left(\frac{d\theta}{ds}\right)^2 = F_{xe} \cos(\theta) + F_{ye} \sin(\theta) + Z \tag{C-6}$$

where Z is a constant of integration. Rearranging gives:

$$ds = \left(\frac{EI}{2\left(F_{xe} \cos(\theta) + F_{ye} \sin(\theta)\right) + Z}\right)^{\frac{1}{2}} d\theta \tag{C-7}$$

Eq. (C-7) can be substituted into Eq. (C-4), however the expressions cannot be integrated across points of inflection $\left(\frac{d\theta}{ds} = 0\right)$[153]. This is addressed by introducing new parameters that allow equations (C-4a-c) to be expressed using elliptic integrals [133,154].

$$P \cos(\alpha) = \frac{2F_{xe}}{EI} \tag{C-8a}$$

$$P \sin(\alpha) = \frac{2F_{ye}}{EI} \tag{C-8b}$$

$$C = \frac{2Z}{EI} \tag{C-8c}$$

which can be combined with basic trigonometric identities giving:

$$ds = \left(\frac{1}{P \cos(\alpha) \cos(\theta) + P \sin(\alpha) \sin(\theta) + C}\right)^{\frac{1}{2}} d\theta$$

$$ds = \left(\frac{1}{P \cos(\alpha - \theta) + C}\right)^{\frac{1}{2}} d\theta$$

Further, a change in the variable of integration is facilitated by the following transformations:

$$2k^2 = \frac{C}{P} + 1 \tag{C-9a}$$

$$1 - 2k^2 \sin^2 \phi = \cos(\alpha - \theta) \tag{C-9b}$$

Differentiating and rearranging (C-9b) by using trigonometric identities yields:

$$d\theta = -\frac{4k^2 sin\phi cos\phi}{\sin(\theta-\alpha)}\, d\phi \tag{C-10a}$$

$$d\theta = -\frac{4k^2 sin\phi cos\phi}{(1-\cos^2(\theta-\alpha))^{\frac{1}{2}}}\, d\phi \tag{C-10b}$$

$$d\theta = -\frac{4k^2 sin\phi cos\phi}{2k\,\sin(\phi)\sqrt{1-k^2\sin\phi}}\, d\phi \tag{C-10c}$$

$$d\theta = 2k\cos(\phi)\,(1-k^2\sin^2(\phi))^{-\frac{1}{2}}\, d\phi \tag{C-10d}$$

and:

$$\sin(\theta) = \sin(\alpha)\,(1-2k^2\sin^2(\phi)) + \cos(\alpha)\,(2k\sin(\phi)\,(1-k^2\sin^2(\phi))^{\frac{1}{2}} \tag{C-10e}$$

$$\cos(\theta) = \cos(\alpha)\,(1-2k^2\sin^2(\phi)) - \sin(\alpha)\,(2k\sin(\phi)\,(1-k^2\sin^2(\phi))^{\frac{1}{2}} \tag{C-10f}$$

To allow integration using the new variables introduced in Eq. (C-9), the following elliptic integrals are employed [154]:

$$F_e(\phi,k) = \int_0^{\phi}(1-k^2\sin^2(\phi))^{-\frac{1}{2}}\, d\phi \tag{C-11a}$$

$$E_e(\phi,k) = \int_0^{\phi}(1-k^2\sin^2(\phi))^{\frac{1}{2}}\, d\phi \tag{C-11b}$$

$F_e(\phi,k)$ and $E_e(\phi,k)$ are the incomplete elliptic integrals of the first and second kind, respectively. These elliptic integrals are combined with Equations (C-6) and (C-10) to rewrite (C-7).

$$L = \left(\frac{2}{P}\right)^{\frac{1}{2}}\left(F_e(\phi_2,k) - F_e(\phi_1,k)\right) \tag{C-12a}$$

$$L - \delta_x = \left(\frac{2}{P}\right)^{\frac{1}{2}}\left[\cos(\alpha)\left(-F_e(\phi_2,k) + F_e(\phi_1,k) + 2E_e(\phi_2,k) - 2E_e(\phi_1,k)\right) + 2k\sin(\alpha)\,(\cos(\phi_2) - \cos(\phi_1))\right] \tag{C-12b}$$

$$y_e = \left(\frac{2}{P}\right)^{\frac{1}{2}}\left[\sin(\alpha)\left(-F_e(\phi_2,k)+F_e(\phi_1,k)+2E_e(\phi_2,k)-2E_e(\phi_1,k)\right)+\right.$$
$$\left.2k\cos(\alpha)\left(-\cos(\phi_2)+\cos(\phi_1)\right)\right] \quad \text{(C-12c)}$$

In Eqs. (C-12a-c), ϕ_1 and ϕ_2 are amplitudes corresponding to the left and right ends of the flexible beam respectively. Since $\theta(s=0)=\beta=\theta(s=L)$ is prescribed at the ends, ϕ_1 and ϕ_2 may be found by solving (C-10b at both ends):

$$\sin(\beta)=\sin(\alpha)\left(1-2k^2\sin^2(\phi_1)\right)+\cos(\alpha)\left(2k\sin(\phi_1)\left(1-k^2\sin^2(\phi_1)\right)^{\frac{1}{2}}\right. \quad \text{(C-12d)}$$

$$\sin(\beta)=\sin(\alpha)\left(1-2k^2\sin^2(\phi_2)\right)+\cos(\alpha)\left(2k\sin(\phi_2)\left(1-k^2\sin^2(\phi_2)\right)^{\frac{1}{2}}\right. \quad \text{(C-12e)}$$

Eqs. (C-12a-e) are solved using the built-in MATLAB function *fsolve* to yield solutions for ϕ_1, ϕ_2, k, P, and α. Since *fsolve* employs iterative solvers, suitable initial estimates must be provided. Noting that points of inflection occur for $\phi = n\pi + \frac{\pi}{2}$ for $n \in \mathbb{Z}$, appropriate initial guesses for ϕ_1 and ϕ_2 are employed to obtain elastica curves with the desired number of inflection points along the beam and concavities at the clamped ends [133], corresponding to the aligned and polarized topologies presented in Figure 4-15(a). Symmetry is exploited to solve for opposite concavities and boundary conditions.

Following the same approach as above, appropriate changes of variable and manipulations can be applied to the expression for bending strain energy. This allows the energy to be computed directly from the solutions to (C-12a-e). First, the bending strain energy in an infinitesimal segment is integrated over the beam length [152]:

$$U = \int_0^{S*} \frac{EI}{2}\left(\frac{d\theta}{ds}\right)^2 ds \quad \text{(C-13)}$$

Using (C-6) - (C-8) to change the variable of integration, this can be rewritten as:

$$U = \sqrt{\frac{EI}{2}}\int \sqrt{\left(F_{xe}\cos(\theta)+F_{ye}\sin(\theta)+Z\right)}d\theta \quad \text{(C-14)}$$

$$U = \frac{EI}{2}\int \sqrt{(P\cos(\alpha-\theta)+C)}d\theta \quad \text{(C-15)}$$

Then, applying (C-9) and (C-10):

$$U = \frac{EI}{2}\int \sqrt{P\left((2k^2 - 1) + \ (1 - 2k^2\sin^2(\phi))\right)}\ d\theta \tag{C-16}$$

$$U = \frac{EI}{2}\int \sqrt{P\ \left(2k^2(1 - \sin^2(\phi))\right)}\frac{2k\cos(\phi)}{\sqrt{(1-k^2\sin^2(\phi))}}\ d\phi \tag{C-17}$$

$$U = \sqrt{2P}EI\int \frac{k^2\left(1-\sin^2(\phi)\right)}{\sqrt{(1-k^2\sin^2(\phi))}}\ d\phi \tag{C-18}$$

$$U = \sqrt{2P}EI\int \frac{k^2-1+1-k^2\sin^2(\phi)}{\sqrt{(1-k^2\sin^2(\phi))}}\ d\phi \tag{C-19}$$

$$U = \sqrt{2P}EI\ \left(\ (k^2 - 1)\int (1 - k^2\sin^2(\phi))^{-\frac{1}{2}}\,d\phi + \ \int (1 - k^2\sin^2(\phi))^{\frac{1}{2}}\,d\phi\right) \tag{C-20}$$

This is can then be written using the elliptic integrals in (C-11) as a finite integral from ϕ_1 to ϕ_2 as:

$$U = EI(2P)^{\frac{1}{2}}\ \left(\ (k^2 - 1)\left(F_e(\phi_2, k) - F_e(\phi_1, k)\right) + \ \left(E_e(\phi_2, k) - E_e(\phi_1, k)\right)\right) \tag{C-21}$$

This can be computed directly after solving for P, k, ϕ_1, ϕ_2 in (C-12).

Appendix D.

Publications, proceedings and comments regarding copyright permissions

The following is a list of publications and proceedings whose contents are included in this thesis. Relevant copyright permissions have been obtained as required.

[98] Kidambi N, Harne RL, Wang KW. Adaptation of energy dissipation in a mechanical metastable module excited near resonance. *J Vib Acoust*. 2016;138(1):11001. doi:10.1115/1.4031411.

[118] Kidambi N, Harne RL, Wang KW. Energy capture and storage in asymmetrically multistable modular structures inspired by skeletal muscle. *Smart Mater Struct*. 2017;26(8). doi:10.1088/1361-665X/aa721a.

[155] Kidambi N, Harne RL, Wang KW. Modular architected material systems inspired by skeletal muscle. *(submitted)*. 2018.

[156] Kidambi N, Harne RL, Wang KW. Asymmetric influences on the energy dissipation performance of a metastable module excited near resonance. In: *Proceedings of the 25th Canadian Congress of Applied Mechanics*. Vol London, ON, Canada; 2015.

[157] Kidambi N, Harne RL, Wang KW. Multistability inspired by the oblique, pennate architectures of skeletal muscle. In: *Active and Passive Smart Structures and Integrated Systems XI*. Vol 10164. Portland, OR, USA; 2017:1016415. doi:10.1117/12.2259990.

[158] Kidambi N, Zheng Y, Harne RL, Wang KW. Energy release for the actuation and deployment of muscle-inspired asymmetrically multistable chains. In: *Active and Passive Smart Structures and Integrated Systems XII*. Vol 1059510. Denver, CO, USA; 2018:35. doi:10.1117/12.2296583.

Figures 1-1 – 1-7 also include published images for which relevant permissions have been obtained.

Bibliography

1. Wagg DJ, Neild SA. *Nonlinear Vibration with Control for Flexible and Adaptive Structures*. Vol 58. Springer; 2010. doi:10.3397/1.3455047.

2. Chopra I. Review of State of Art of Smart Structures and Integrated Systems. *AIAA J*. 2002;40(11):2145-2187. doi:10.2514/2.1561.

3. Sun JQ, Jolly MR, Norris MA. Passive, Adaptive and Active Tuned Vibration Absorbers—A Survey. *J Vib Acoust*. 1995;117(B):234. doi:10.1115/1.2838668.

4. Lieber RL. *Skeletal Muscle Structure, Function, and Plasticity*. Vol 3rd ed. Baltimore, MD: Lippincott Williams & Wilkins; 2010.

5. Tortora GJ, Nielsen MT. *Principles of Human Anatomy*. Vol 12th ed. New York, USA: Wiley; 2012. doi:10.1007/s13398-014-0173-7.2.

6. George NT, Irving TC, Williams CD, Daniel TL. The Cross-Bridge Spring : Can Cool Muscles Store Elastic Energy? *Science*. 2013;340(June):1217-1220. doi:10.1126/science.1229573.

7. Azizi E, Brainerd EL, Roberts TJ. Variable gearing in pennate muscles. *Proc Natl Acad Sci*. 2008;105(5):1745-1750. doi:10.1073/pnas.0709212105.

8. Lappin AK, Monroy JA, Pilarski JQ, Zepnewski ED, Pierotti DJ, Nishikawa KC. Storage and recovery of elastic potential energy powers ballistic prey capture in toads. *J Exp Biol*. 2006;209(Pt 13):2535-2553. doi:10.1242/jeb.02276.

9. Zack TI, Claverie T, Patek SN. Elastic energy storage in the mantis shrimp's fast predatory strike. *J Exp Biol*. 2009;212:4002-4009. doi:10.1242/jeb.034801.

10. Epstein M, Herzog W. *Theoretical Models of Skeletal Muscle*. New York, NY: Wiley; 1998.

11. Shimamoto Y, Suzuki M, Mikhailenko S V., Yasuda K, Ishiwata S. Inter-sarcomere coordination in muscle revealed through individual sarcomere response to quick stretch. *Proc Natl Acad Sci U S A*. 2009;106(29):11954-11959. doi:10.1073/pnas.0813288106.

12. Marcucci L, Truskinovsky L. Muscle contraction: A mechanical perspective. *Eur Phys J E Soft Matter*. 2010;32(4):411-418. doi:10.1140/epje/i2010-10641-0.

13. Caruel M, Allain J-M, Truskinovsky L. Mechanics of collective unfolding. *J Mech Phys Solids*. 2015;76:237-259. doi:10.1016/j.jmps.2014.11.010.

14. Lombardi V, Piazzesi G, Linari M. Rapid regeneration of the actin-myosin power stroke in contracting muscle. *Nature*. 1992;355:638-641.

15. Sato K, Ohtaki M, Shimamoto Y, Ishiwata S. A theory on auto-oscillation and contraction in striated muscle. *Prog Biophys Mol Biol*. 2011;105(3):199-207. doi:10.1016/j.pbiomolbio.2010.12.003.

16. Herzog W. Mechanisms of enhanced force production in lengthening (eccentric) muscle contractions. *J Appl Physiol*. 2014;116(11):1407-1417. doi:10.1152/japplphysiol.00069.2013.

17. Azizi E, Roberts TJ. Geared up to stretch: pennate muscle behavior during active lengthening. *J Exp Biol*. 2014;217:376-381. doi:10.1242/jeb.094383.

18. Monroy JA, Lappin AK, Nishikawa KC. Elastic Properties of Active Muscle - On the Rebound? *Exerc Sport Sci Rev*. 2007;35(4).

19. Magid A, Law DJ. Myofibrils Bear Most of the Resting Tension in Frog Skeletal Muscle. *Science*. 1985;230(4731):1280-1282.

20. Cooper GM. Actin, Myosin, and Cell Movement. In: *The Cell: A Molecular Approach*. Vol Sunderland, MA: Sinauer Associates; 2000.

21. Ishikawa M, Komi P V, Grey MJ, Lepola V, Bruggemann G-P. Muscle-tendon interaction and elastic energy usage in human walking. *J Appl Physiol*. 2005;99(2):603-608. doi:10.1152/japplphysiol.00189.2005.

22. Scott SH, Winter DA. A comparison of three muscle pennation assumptions and their effect on isometric and isotonic force. *J Biomech*. 1991;24(2):163-167. doi:10.1016/0021-9290(91)90361-P.

23. Woittiez RD, Huijing PA, Rozendal RH. Influence of muscle architecture on the length-force diagram of mammalian muscle. *Pflügers Arch Eur J Physiol*. 1983;399(4):275-279. doi:10.1007/BF00652752.

24. Piazzesi G, Lombardi V. A cross-bridge model that is able to explain mechanical and energetic properties of shortening muscle. *Biophys J*. 1995;68(5):1966-1979. doi:10.1016/S0006-3495(95)80374-7.

25. Givli S, Bhattacharya K. A coarse-grained model of the myofibril: Overall dynamics and the evolution of sarcomere non-uniformities. *J Mech Phys Solids*. 2009;57(2):221-243. doi:10.1016/j.jmps.2008.10.013.

26. Denoth J, Stüssi E, Csucs G, Danuser G. Single muscle fiber contraction is dictated by inter-sarcomere dynamics. *J Theor Biol*. 2002;216(1):101-122. doi:10.1006/jtbi.2001.2519.

27. Novak I, Truskinovsky L. Nonaffine response of skeletal muscles on the "descending limb." *Math Mech Solids*. 2014;20(6):1081286514551504-. doi:10.1177/1081286514551504.

28. Wareham AC. Muscle. *Anaesth Intensive Care Med*. 2011;12(6):249-252. doi:10.1016/j.mpaic.2011.03.009.

29. Hill AV. The series elastic component of muscle. *Proc R Soc Lond A*. 1950;137(887):273-280.

30. Hill AV. The mechanics of active muscle. *Proc R Soc B Biol Sci*. 1953;141(902):104-117.

31. Hill AV. The heat of shortening and the dynamic constants of muscle. *Proc R Soc B Biol Sci*. 1938;126(843):136-195. doi:10.1098/rspb.1938.0050.

32. Allinger TL, Epstein M, Herzog W. Stability of muscle fibers on the descending limb of the force-length relation. A theoretical consideration. *J Biomech*. 1996;29(5):627-633. doi:10.1016/0021-9290(95)00087-9.

33. Morgan DL, Proske U. Sarcomere popping requires stretch over a range where total tension decreases with length. *J Physiol*. 2006;574(2):627-628. doi:10.1113/jphysiol.2006.574201.

34. Morgan DL. New insights into the behavior of muscle during active lengthening. *Biophys J*. 1990;57(2):209-221. doi:10.1016/S0006-3495(90)82524-8.

35. Caruel M, Truskinovsky L. Physics of muscle contraction. *Reports Prog Phys*. 2017.

36. Irving TC, Konhilas J, Perry D, Fischetti R, de Tombe P. Myofilament lattice spacing as a function of sarcomere length in isolated rat myocardium. *Am J Hear Circ Physiol*. 2000;279(5):H2568-H2573. doi:10.1152/ajpheart.2000.279.5.H2568.

37. Williams CD, Salcedo MK, Irving TC, Regnier M, Daniel TL. The length–tension curve in muscle depends on lattice spacing. *Proc R Soc B Biol Sci*. 2013;280(1766):697. doi:10.1098/rspb.2013.0697.

38. Williams CD, Regnier M, Daniel TL. Elastic energy storage and radial forces in the myofilament lattice depend on sarcomere length. *PLoS Comput Biol*. 2012;8(11):e1002770. doi:10.1371/journal.pcbi.1002770.

39. Gordon AM, Huxley AF, Julian FJ. The variation in isometric tension with sarcomere length in vertebrate muscle fibres. *J Physiol*. 1966;184(1):170-192. doi:5921536.

40. Caruel M. Mechanics of fast force recovery in striated muscles. 2011.

41. Lindstedt SL, LaStayo PC, Reich TE. When active muscles lengthen: Properties and consequences of eccentric contractions. *Physiology*. 2001;16(6):256-261. doi:10.1113/jphysiol.1976.sp011515.

42. Benichou I, Givli S. Structures undergoing discrete phase transformation. *J Mech Phys Solids*. 2013;61(1):94-113. doi:10.1016/j.jmps.2012.08.009.

43. Benichou I, Givli S. The hidden ingenuity in titin structure. *Appl Phys Lett*. 2011;98(9):91904. doi:10.1063/1.3558901.

44. Marszalek PE, Lu H, Li H, et al. Mechanical unfolding intermediates in titin modules. *Nature*. 1999;402(November):100-103. doi:10.1038/47083.

45. Cohen T, Givli S. Dynamics of a discrete chain of bi-stable elements: A biomimetic shock absorbing mechanism. *J Mech Phys Solids*. 2014;64(1):426-439. doi:10.1016/j.jmps.2013.12.010.

46. Huxley HE. Fifty years of muscle and the sliding filament hypothesis. *Eur J Biochem*. 2004;271(8):1403-1415. doi:10.1111/j.1432-1033.2004.04044.x.

47. Huxley AF, Niedergerke R. Structural changes in muscle during contraction: Interference microscopy of living muscle fibres. *Nature*. 1954;173(4412):971-973. doi:10.1038/173971a0.

48. Huxley HE, Hanson J. Changes in the cross-striations of muscle during contraction and stretch and their structural interpretation. *Nature*. 1954;173(4412):973-976.

49. Huxley HE. The double array of filaments in cross-striated muscle. *J Cell Biol*. 1957;3(5):631-648.

50. Huxley AF. The mechanism of muscular contraction. *Science*. 1969;164(3886):1356-1365. doi:10.1113/jphysiol.1974.sp010740.

51. Lymn RW, Taylor EW. Mechanism of adenosine triphosphate hydrolysis by actomyosin. *Biochemistry*. 1971;10(25):4617-4624. doi:10.1021/bi00801a004.

52. Marcucci L, Truskinovsky L. Mechanics of the power stroke in myosin II. *Phys Rev E*. 2010;81(5):51915. doi:10.1103/PhysRevE.81.051915.

53. Huxley AF, Simmons RM. Proposed mechanism of force generation in striated muscle. *Nature*. 1971;233(5321):533-538. doi:10.1038/233533a0.

54. Caruel M, Allain J-M, Truskinovsky L. Muscle as a metamaterial operating near a critical point. *Phys Rev Lett*. 2013;110(24):248103. doi:10.1103/PhysRevLett.110.248103.

55. Caruel M, Truskinovsky L. Mechanical bi-stability resistant to fluctuations. *J Mech Phys Solids*. 2017. http://arxiv.org/abs/1612.05732.

56. Ishiwata S, Shimamoto Y, Fukuda N. Contractile system of muscle as an auto-oscillator. *Prog Biophys Mol Biol*. 2011;105(3):187-198. doi:10.1016/j.pbiomolbio.2010.11.009.

57. Williams CD, Regnier M, Daniel TL. Axial and radial forces of cross-bridges depend on lattice spacing. *PLoS Comput Biol*. 2010;6(12):e1001018. doi:10.1371/journal.pcbi.1001018.

58. Collins S, Ruina A, Tedrake R, Wisse M. Efficient bipedal robots based on passive-dynamic walkers. *Science*. 2005;307(5712):1082-1085. doi:10.1126/science.1107799.

59. Garcia E, Jimenez MA, De Santos PG, Armada M. The evolution of robotics research. *IEEE Robot Autom Mag*. 2007;14(1):90-103. doi:10.1109/MRA.2007.339608.

60. Beer RD, Quinn RD, Chiel, Hillel J, Ritzmann RE. Biologically inspired approaches to robotics: What can we learn from insects? *Commun ACM*. 1997;40(3).

61. Yao X, Song Y, Jiang L. Applications of bio-inspired special wettable surfaces. *Adv Mater*. 2011;23(6):719-734. doi:10.1002/adma.201002689.

62. Munch E, Launey ME, Alsem DH, Saiz E, Tomsia AP, Ritchie RO. Tough, bio-inspired hybrid materials. *Science*. 2008;322(5907):1516-1520. doi:10.1126/science.1164865.

63. Ilievski F, Mazzeo AD, Shepherd RF, Chen X, Whitesides GM. Soft robotics for chemists. *Angew Chemie - Int Ed*. 2011;50(8):1890-1895. doi:10.1002/anie.201006464.

64. Martinez R V., Glavan AC, Keplinger C, Oyetibo AI, Whitesides GM. Soft actuators and robots that are resistant to mechanical damage. *Adv Funct Mater*. 2014;24(20):3003-3010. doi:10.1002/adfm.201303676.

65. Vandesteeg NA, Anquetil PA, Madden PGA, et al. Artificial muscle technology: Physical principles and naval prospects. *IEEE J Ocean Eng*. 2004;29(3):7006-7028. doi:10.1109/JOE.2004.833135.

66. Huber JE, Fleck NA, Ashby MF. The selection of mechanical actuators based on performance indices. *Proc R Soc London A Math Phys Eng Sci*. 1997;453(1965):2185-2205. doi:10.1098/rspa.1997.0117.

67. Tondu B, Lopez P. Modeling and control of McKibben artificial muscle robot actuators. *IEEE Control Syst Mag*. 2000;20(2):15-38. doi:10.1109/37.833638.

68. Azizi E, Roberts TJ. Variable gearing in a biologically inspired pneumatic actuator array. *Bioinspir Biomim*. 2013;8(2):26002. doi:10.1088/1748-3182/8/2/026002.

69. Bar-Cohen J, ed. *Electroactive Polymer (EAP) Actuators as Artificial Muscles*. Vol 2nd ed. Bellingham, WA: SPIE; 2004.

70. Biggs J, Danielmeier K, Hitzbleck J, et al. Electroactive polymers: Developments of and perspectives for dielectric elastomers. *Angew Chemie - Int Ed*. 2013;52(36):9409-9421. doi:10.1002/anie.201301918.

71. Chouinard P, Plante JS. Bistable antagonistic dielectric elastomer actuators for binary robotics and mechatronics. *IEEE/ASME Trans Mechatronics*. 2012;17(5):857-865. doi:10.1109/TMECH.2011.2135862.

72. Mohd Jani J, Leary M, Subic A, Gibson MA. A review of shape memory alloy research, applications and opportunities. *Mater Des*. 2014;56:1078-1113. doi:10.1016/j.matdes.2013.11.084.

73. Gao Y, Zhang C. Structure-function relationship of skeletal muscle provides inspiration for design of new artificial muscle. *Smart Mater Struct*. 2014;under revi(3):33002. doi:10.1088/0964-1726/24/3/033002.

74. Ueda J, Odhner L, Asada HH. Broadcast Feedback of Stochastic Cellular Actuators Inspired by Biological Muscle Control. *Int J Rob Res*. 2007;26(11-12):1251-1265. doi:10.1177/0278364907082443.

75. Wu Z, Harne RL, Wang KW. Exploring a modular adaptive metastructure concept inspired by muscle's cross-bridge. *J Intell Mater Syst Struct*. 2016;27(9):1189-1202. doi:10.1177/1045389X15586451.

76. Harne RL, Wu Z, Wang KW. Designing and harnessing the metastable states of a modular metastructure for programmable mechanical properties adaptation. *J Mech Des*. 2016;138(2):21402. doi:10.1115/1.4032093.

77. Sellers JR, Veigel C. Direct observation of the myosin-Va power stroke and its reversal. *Nat Struct Mol Biol*. 2010;17(5):590-595. doi:10.1038/nsmb.1820.

78. Kochmann DM. Stable extreme damping in viscoelastic two-phase composites with non-positive-definite phases close to the loss of stability. *Mech Res Commun*. 2014;58:36-45. doi:10.1016/j.mechrescom.2013.09.003.

79. Klatt T, Haberman MR. A nonlinear negative stiffness metamaterial unit cell and small-on-large multiscale material model. *J Appl Phys*. 2013;114(3). doi:10.1063/1.4813233.

80. Lakes RS. Extreme damping in compliant composites with a negative-stiffness phase. *Philos Mag Lett*. 2001;81(2):95-100. doi:10.1080/09500830010015332.

81. Wang YC, Ludwigson M, Lakes RS. Deformation of extreme viscoelastic metals and composites. *Mater Sci Eng A*. 2004;370(1-2):41-49. doi:10.1016/j.msea.2003.08.071.

82. Barbarino S, Pontecorvo ME, Gandhi FS. Energy Dissipation of a Bi - Stable von - Mises Truss under Harmonic Excitation. In: *AIAA/ASME/ASCE/AHS/ASC Structures, Structural Dynamics, and Materials Conference*. Vol Honolulu, HI; 2012.

83. Johnson DR, Thota M, Semperlotti F, Wang KW. On achieving high and adaptable damping via a bistable oscillator. *Smart Mater Struct*. 2013;22(11):115027. doi:10.1088/0964-1726/22/11/115027.

84. Nadkarni N, Daraio C, Kochmann DM. Dynamics of periodic mechanical structures containing bistable elastic elements : From elastic to solitary wave propagation. *Phys Rev E*. 2014;23204:1-13. doi:10.1103/PhysRevE.90.023204.

85. Bažant ZP, Cedolin L. *Stability of Structures: Elastic, Inelastic, Fracture, and Damage Theories*. Hackensack, NJ: World Scientific Publishing Company; 2010.

86. Lakes RS, Drugan WJ. Dramatically stiffer elastic composite materials due to a negative stiffness phase? *J Mech Phys Solids*. 2002;50(5):979-1009. doi:http://dx.doi.org/10.1016/S0022-5096(01)00116-8.

87. Virgin LN. *Vibration of Axially Loaded Structures*. Cambridge University Press; 2007. doi:10.1017/CBO9780511619236.

88. Rao SS. *Mechanical Vibrations*. Vol 4th ed. Upper Saddle River, NJ: Prentice Hall; 2003.

89. Kovacic I, Brennan MJ. *The Duffing Equation: Nonlinear Oscillators and Their Behavior*.; 2011.

90. Nayfeh AH, Mook DT. *Nonlinear Oscillations*. Weinheim: Wiley; 1995.

91. Harne RL, Thota M, Wang KW. Concise and high-fidelity predictive criteria for maximizing performance and robustness of bistable energy harvesters. *Appl Phys Lett*. 2013;102(5):1-5. doi:10.1063/1.4790381.

92. Lakes RS. *Viscoelastic Materials*. Vol 1st ed. New York, NY: Cambridge University Press; 2009.

93. Wiebe R, Virgin LN, Stanciulescu I, Spottswood SM, Eason TG. Characterizing Dynamic Transitions Associated With Snap-Through: A Discrete System. *J Comput Nonlinear Dyn*. 2012;8(1):11010. doi:10.1115/1.4006201.

94. Sheshka R, Truskinovsky L. Power-stroke-driven actomyosin contractility. *Phys Rev E - Stat Nonlinear, Soft Matter Phys*. 2014;89(1):1-12. doi:10.1103/PhysRevE.89.012708.

95. Hu N, Burgueño R. Buckling-induced smart applications: recent advances and trends. *Smart*

Mater Struct. 2015;24(6):63001. doi:10.1088/0964-1726/24/6/063001.

96. Harne RL, Wang KW. *Harnessing Bistable Structural Dynamics: For Vibration Control, Energy Harvesting and Sensing*. Chichester, UK: Wiley; 2017.

97. Lakes RS. Extreme damping in composite materials with a negative stiffness phase. *Phys Rev Lett*. 2001;86(13):2897-2900. doi:10.1103/PhysRevLett.86.2897.

98. Kidambi N, Harne RL, Wang KW. Adaptation of energy dissipation in a mechanical metastable module excited near resonance. *J Vib Acoust*. 2016;138(1):11001. doi:10.1115/1.4031411.

99. Correa DM, Klatt T, Cortes S, Haberman MR, Kovar D, Seepersad CC. Negative stiffness honeycombs for recoverable shock isolation. *Rapid Prototyp J*. 2015;21(2):193-200. doi:10.1108/RPJ-12-2014-0182.

100. Qiu J, Lang JH, Slocum AH. A curved-beam bistable mechanism. *J Microelectromechanical Syst*. 2004;13(2):137-146. doi:10.1109/JMEMS.2004.825308.

101. Winkelmann C, Kim SS, La Saponara V. Design and development of hybrid composite bistable structures for energy absorption under quasi-static tensile loading. *Compos Struct*. 2010;93(1):171-178. doi:10.1016/j.compstruct.2010.06.002.

102. Rafsanjani A, Akbarzadeh A, Pasini D. Snapping mechanical metamaterials under tension. *Adv Mater*. August 2015. doi:10.1002/adma.201502809.

103. Shan S, Kang SH, Raney JR, et al. Multistable architected materials for trapping elastic strain energy. *Adv Mater*. 2015;27(17). doi:10.1002/adma.201501708.

104. Restrepo D, Mankame ND, Zavattieri PD. Phase transforming cellular materials. *Extrem Mech Lett*. 2015;4:52-60. doi:10.1016/j.eml.2015.08.001.

105. Benichou I, Givli S. Rate dependent response of nanoscale structures having a multiwell energy landscape. *Phys Rev Lett*. 2015;114(9):95504. doi:10.1103/PhysRevLett.114.095504.

106. Puglisi G, Truskinovsky L. Mechanics of a discrete chain with bi-stable elements. *J Mech Phys Solids*. 2000;48(1):1-27. doi:10.1016/S0022-5096(99)00006-X.

107. Comte JC, Marquié P, Remoissenet M. Dissipative lattice model with exact traveling discrete kink-soliton solutions: discrete breather generation and reaction diffusion regime. *Phys Rev E Stat Phys Plasmas Fluids Relat Interdiscip Topics*. 1999;60(6):7484-7489. doi:10.1103/PhysRevE.60.7484.

108. Nadkarni N, Daraio C, Abeyaratne R, Kochmann DM. A universal energy transport law for dissipative and diffusive phase transitions. *Phys Rev B*. 2016;93(10):104109. doi:10.1103/PhysRevB.93.104109.

109. Puglisi G, Truskinovsky L. Thermodynamics of rate-independent plasticity. *J Mech Phys Solids*. 2005;53(3):655-679. doi:10.1016/j.jmps.2004.08.004.

110. Che K, Yuan C, Wu J, Jerry Qi H, Meaud J. Three-Dimensional-Printed Multistable Mechanical Metamaterials With a Deterministic Deformation Sequence. *J Appl Mech*. 2016;84(1):11004.

doi:10.1115/1.4034706.

111. Oh YS, Kota S. Synthesis of multistable equilibrium compliant mechanisms using combinations of bistable mechanisms. *J Mech Des*. 2009;131(2):21002. doi:10.1115/1.3013316.

112. Bravo Yuste S, Diaz Bejarano J. Improvement of a Kyrlov-Bogoliubov method that uses Jacobi elliptic functions. *J Sound Vib*. 1990;139(1):151-163.

113. Okabe T, Kondou T, Ohnishi J. Elliptic averaging methods using the sum of Jacobian elliptic delta and zeta functions as the generating solution. *Int J Non Linear Mech*. 2011;46(1):159-169. doi:10.1016/j.ijnonlinmec.2010.08.004.

114. Zhang C, Harne RL, Li B, Wang KW. Reconstructing the transient, dissipative dynamics of a bistable Duffing oscillator with an enhanced averaging method and Jacobian elliptic functions. *Int J Non Linear Mech*. 2016;79:26-37. doi:10.1016/j.ijnonlinmec.2015.11.002.

115. Picchini U. SDE Toolbox: Simulation and Estimation of Stochastic Differential Equations with MATLAB. 2007. http://sdetoolbox.sourceforge.net/.

116. Daqaq MF. On intentional introduction of stiffness nonlinearities for energy harvesting under white Gaussian excitations. *Nonlinear Dyn*. 2012;69(3):1063-1079. doi:10.1007/s11071-012-0327-0.

117. Harne RL, Dai Q. Characterizing the robustness and susceptibility of steady-state dynamics in post-buckled structures to stochastic perturbations. *J Sound Vib*. 2017;395:258-271. doi:10.1016/j.jsv.2017.02.006.

118. Kidambi N, Harne RL, Wang KW. Energy capture and storage in asymmetrically multistable modular structures inspired by skeletal muscle. *Smart Mater Struct*. 2017;26(8). doi:10.1088/1361-665X/aa721a.

119. Puglisi G, Truskinovsky L. Rate independent hysteresis in a bi-stable chain. *J Mech Phys Solids*. 2002;50:165-187. doi:10.1016/S0022-5096(01)00055-2.

120. Benichou I, Zhang Y, Dudko OK, Givli S. The rate dependent response of a bistable chain at finite temperature. *J Mech Phys Solids*. 2016;95:44-63. doi:10.1016/j.jmps.2016.05.001.

121. Cherkaev A V., Cherkaev E, Slepyan LI. Transition waves in bistable structures. I. Delocalization of damage. *J Mech Phys Solids*. 2005;53(2):383-405. doi:10.1016/j.jmps.2004.08.002.

122. Maganaris CN. Force-length characteristics of the in vivo human gastrocnemius muscle. *Clin Anat*. 2003;16(3):215-223. doi:10.1002/ca.10064.

123. Fulcher BA, Shahan DW, Haberman MR, Seepersad CC, Wilson PS. Analytical and Experimental Investigation of Buckled Beams as Negative Stiffness Elements for Passive Vibration and Shock Isolation Systems. *J Vib Acoust*. 2014;136:31009. doi:10.1115/1.4026888.

124. Florijn B, Coulais C, van Hecke M. Programmable mechanical metamaterials. *Phys Rev Lett*. 2014;113:175503. doi:10.1103/PhysRevLett.113.175503.

125. Bertoldi K, Reis PM, Willshaw S, Mullin T. Negative poisson's ratio behavior induced by an

elastic instability. *Adv Mater*. 2010;22(3):361-366. doi:10.1002/adma.200901956.

126. Mullin T, Deschanel S, Bertoldi K, Boyce MC. Pattern transformation triggered by deformation. *Phys Rev Lett*. 2007;99(8):1-4. doi:10.1103/PhysRevLett.99.084301.

127. Mullin T, Willshaw S, Box F. Pattern switching in soft cellular solids under compression. *Soft Matter*. 2013;9(20):4951. doi:10.1039/c3sm27677e.

128. Pihler-Puzović D, Hazel AL, Mullin T. Buckling of a holey column. *Soft Matter*. 2016;12:7112-7118. doi:10.1039/C6SM00948D.

129. Smooth-On. Mold Star 15, 16 and 30 Technical Bulletin. https://www.smooth-on.com/tb/files/MOLD_STAR_15_16_30_TB.pdf.

130. da Rocha HB, Truskinovsky L. Functionality of disorder in muscle mechanics. 2017;4(1):1-5. http://arxiv.org/abs/1711.01160.

131. Ogden RW. *Non-Linear Elastic Deformations*. New York, USA: Dover; 1997.

132. Zienkiewicz OC, Taylor RL. *The Finite Element Method*. Vol 5th Editio. Oxford, UK: Butterworth-Heinemann; 2000.

133. Shoup TE, McLarnan CW. On the use of the undulating elastica for the analysis of flexible link mechanisms. *J Eng Ind*. 1971;93(1):263-267.

134. Chirikjian GS. Kinematic Synthesis of Mechanisms and Robotic Manipulators With Binary Actuators. *J Mech Des*. 1995;(March 1995):3-10.

135. Wingert A, Lichter MD, Dubowsky S. On the design of large degree-of-freedom digital mechatronic devices based on bistable dielectric elastomer actuators. *IEEE/ASME Trans Mechatronics*. 2006;11(4):448-456. doi:10.1109/TMECH.2006.878542.

136. Hafez M, Lichter MD, Dubowsky S. Optimized binary modular reconfigurable robotic devices. *IEEE/ASME Trans Mechatronics*. 2003;8(1):18-25. doi:10.1109/TMECH.2003.809156.

137. Zhai Z, Wang Y, Jiang H. Origami-inspired, on-demand deployable and collapsible mechanical metamaterials with tunable stiffness. *Proc Natl Acad Sci U S A*. 2018;0:201720171. doi:10.1073/pnas.1720171115.

138. Puig L, Barton A, Rando N. A review on large deployable structures for astrophysics missions. *Acta Astronaut*. 2010;67(1-2):12-26. doi:10.1016/j.actaastro.2010.02.021.

139. Filipov ET, Liu K, Tachi T, Schenk M, Paulino GH. Bar and hinge models for scalable analysis of origami. *Int J Solids Struct*. 2017;124:26-45. doi:10.1016/j.ijsolstr.2017.05.028.

140. Roussel L, Canudas-de-Wit C, Goswami A. Generation of energy optimal complete gait cycles for biped robots. *Int Conf Robot Autom*. 1998;(May):2036-2041. doi:10.1016/j.jsb.2011.03.007.

141. Li S, Wang KW. Fluidic origami: A plant-inspired adaptive structure with shape morphing and stiffness tuning. *Smart Mater Struct*. 2015;24(10). doi:10.1088/0964-1726/24/10/105031.

142. Mosadegh B, Polygerinos P, Keplinger C, et al. Pneumatic networks for soft robotics that actuate rapidly. *Adv Funct Mater*. 2014;24(15):2163-2170. doi:10.1002/adfm.201303288.

143. Harne RL, Deng Z, Dapino MJ. Adaptive magnetoelastic metamaterials: A new class of magnetorheological elastomers. *J Intell Mater Syst Struct*. 2017:1045389X1772103. doi:10.1177/1045389X17721037.

144. Evans E, Ritchie K. Dynamic strength of molecular adhesion bonds. *Biophys J*. 1997;72(4):1541-1555. doi:10.1016/S0006-3495(97)78802-7.

145. Raney JR, Nadkarni N, Daraio C, Kochmann DM, Lewis JA, Bertoldi K. Stable propagation of mechanical signals in soft media using stored elastic energy. *Proc Natl Acad Sci*. 2016;113(35):201604838. doi:10.1073/pnas.1604838113.

146. Martinez R V., Fish CR, Chen X, Whitesides GM. Elastomeric origami: Programmable paper-elastomer composites as pneumatic actuators. *Adv Funct Mater*. 2012;22(7):1376-1384. doi:10.1002/adfm.201102978.

147. Chen T, Shea K. An autonomous programmable actuator and shape reconfigurable structures using bistability and shape memory polymers. 2017:1-8. http://arxiv.org/abs/1711.00452.

148. Filipov ET, Tachi T, Paulino GH. Origami tubes assembled into stiff, yet reconfigurable structures and metamaterials. *Proc Natl Acad Sci*. 2015;112(40):12321-12326. doi:10.1073/pnas.1509465112.

149. Kamrava S, Mousanezhad D, Ebrahimi H, Ghosh R, Vaziri A. Origami-based cellular metamaterial with auxetic, bistable, and self-locking properties. *Sci Rep*. 2017;7:46046. doi:10.1038/srep46046.

150. Li S, Wang KW. Plant-inspired adaptive structures and materials for morphing and actuation: A review. *Bioinspiration and Biomimetics*. 2017;12(1). doi:10.1088/1748-3190/12/1/011001.

151. Cai J, Deng X, Zhou Y, Feng J, Tu Y. Bistable behavior of the cylindrical origami structure with Kresling pattern. *J Mech Des*. 2015;137(6):61406. doi:10.1115/1.4030158.

152. Timoshenko SP, Gere JM. *Theory of Elastic Stability*. Vol Second. New York, USA: McGraw-Hill; 1963.

153. Chen J-S, Lin Y-Z. Snapping of a planar elastica with fixed end slopes. *J Appl Mech*. 2008;75(4):410241-410246. doi:10.1115/1.2871207.

154. Byrd PF, Friedman MD. *Handbook of Elliptic Integrals for Engineers and Scientists*. Vol 2nd ed. Berlin: Springer-Verlag; 1971.

155. Kidambi N, Harne RL, Wang KW. Modular architected material systems inspired by skeletal muscle. *(submitted)*. 2018.

156. Kidambi N, Harne RL, Wang KW. Asymmetric influences on the energy dissipation performance of a metastable module excited near resonance. In: *Proceedings of the 25th Canadian Congress of Applied Mechanics*. Vol London, ON, Canada; 2015.

157. Kidambi N, Harne RL, Wang KW. Multistability inspired by the oblique, pennate architectures of skeletal muscle. In: *Active and Passive Smart Structures and Integrated Systems XI*. Vol 10164. Portland, OR, USA; 2017:1016415. doi:10.1117/12.2259990.

158. Kidambi N, Zheng Y, Harne RL, Wang KW. Energy release for the actuation and deployment of muscle-inspired asymmetrically multistable chains. In: *Active and Passive Smart Structures and Integrated Systems XII*. Vol 1059510. Denver, CO, USA; 2018:35. doi:10.1117/12.2296583.